TECHNISCHE UNIVERSITÄT MÜNCHEN

Interface Optimization of Tungsten Fiber-Reinforced Copper for Heat Sink Application

Aurelia Herrmann

Pour ma famille

Kurzfassung

Für zukünftige Fusionsreaktoren wie beispielsweise DEMO werden im Bereich des Divertors Wärmeflüsse bis zu 20 MW/m² erwartet. Dadurch können an der Grenzfläche zwischen plasmabeslasteten Material, Wolfram, und der Wärmesenke, Cu oder CuCr1Zr, je nach Divertordesign, Temperaturen bis zu 550°C auftreten. Um diesen hochbelasteten Bereich zu verstärken, wurde ein neuartiger W_f/Cu Metall-Matrix Verbundwerkstoff entwickelt und bewertet.

Das Ziel dieser Arbeit ist die Optimierung der Grenzflächenadhäsion zwischen Wolframfasern und der Kupfermatrix, um gute mechanische Eigenschaften des Verbundwerkstoffs zu erreichen. Der Optimierungsprozess beinhaltet zunächst eine Anpassung der Faseroberfläche mittels Beschichtungen mit unterschiedlichen Zwischenschichten, um sowohl einen Formschluß von Faser und Matrix zu erhalten als auch eine verbesserte Faser/Matrix Adhäsion zu erzeugen. Um die mechanische Verzahnung von Faser und Matrix zusätzlich zu verbessern, wird die Faseroberfläche durch unterschiedliche Methoden im Mikro- und Nanobereich modifiziert. Die optimierten Grenzflächeneigenschaften werden anschließend, durch Pull-out Versuche von Einzelfasern, charakterisiert und bewertet.

Die dünnen Zwischenschichten werden durch das Magnetron-Zerstäubungsverfahren auf die Wolframfasern abgeschieden und anschließend durch Wärmebehandlungen, die einerseits dem Herstellungsprozess und andererseits der geplanten Einsatztemperatur angepasst sind, unterzogen. Die Oberflächenstruktur der Fasern, die Zusammensetzung, der Spannungszustand sowie die Textur der Zwischenschichten werden durch Rutherford-Rückstreu-spektroskopie (RBS), Röntgenbeugung (XRD) und unterschiedliche mikroskopische Verfahren untersucht. Durch die Abscheidung einer 500 nm dünnen stufenweise als auch kontinuierlich gradierten W/Cu-Schicht und einer Wärmebehandlung bei 800°C kann die Adhäsion zwischen Faser und Matrix gegenüber einer unbehandelten Grenzfläche um das sechsfache verbessert werden. Zusätzlich zeigen Neutronenbeugungsuntersuchungen sowie thermisch zyklierte Verbundproben, dass diese gradierte Übergangsschicht eine schrittweise Anpassung der unterschiedlichen Wärmeaus-

dehnungskoeffizienten darstellt und die Spannungen an der W/Cu Grenzfläche signifikant reduziert.

Zur Strukturierung der Faseroberfläche auf Mikro- und Nanoskala werden unterschiedliche Verfahren wie Ionenätzen, chemisches Ätzen oder Verdrillung der Wolframfasern angewendet. Das Ziel dabei ist, eine verbesserte Verzahnung der Faser in der Kupfermatrix zu erreichen. Die daraus resultierenden Änderungen der Fasereigenschaften wie Zugfestigkeit, Morphologie oder Rauhigkeit werden auf mehreren Längenskalen untersucht. Die verschiedenen Mikrostrukturierungskonzepte haben einen unterschiedlichen Einfluss auf die Faseroberfläche, der von Glättung der Oberfläche durch das Ionenätzen bis hin zu einer rissigen Oberflächenstruktur durch das Verdrillen reicht. Einzelfaserzugversuche zeigen eine Abnahme der Zugfestigkeit durch die Mikrostrukturierung der Faseroberfläche auf der anderen Seite zeigen Pull-out Versuche eine deutliche Zunahme der Grenzflächenscherfestigkeit. Der beste Kompromiss zwischen Adhäsion und Oberflächenstruktur besteht dabei in einer kontinuierlich gradierten Übergangsschicht mit 800°C Wärmebehandlung, die auf einer chemisch geätzten Wolframfaser abgeschieden wird. Um das Potenzial eines derartigen Verbundwerkstoffes aufzuzeigen werden zwei Monoblock-Prototypen mit dieser optimierten W/Cu-Grenzfläche unter verschiedenen Wärmeflusskonfigurationen getestet. Dabei zeigt sich, dass die Fasern auch bei einem Wärmefluss von 10.5 MW/m^2 stabil in der Kupfermatrix eingebettet bleiben und dadurch ein sehr gutes thermomechanisches Verhalten des Bauteils garantieren. Diese abschließenden Wärmeflusstests demonstrieren, dass der neuartige W$_f$/Cu-Verbundwerkstoff geeignet ist, den hochbelasteten Grenzflächenbereich zwischen dem plasmabelasteten Material und der Wärmesenke zu verstärken.

Abstract

In future fusion reactors like DEMO, heat fluxes up to 20 MW/m^2 are expected in the divertor region. Depending on the divertor design, this results in high temperatures up to 550°C at the interface between plasma-facing material (W) and the water-cooled heat sink material (Cu, CuCr1Zr). A novel W_f/Cu metal matrix composite (MMC) was developed and validated to strengthen this zone by improving the mechanical performance at high temperatures.

The aim of this work is the interface optimization between the W fibers and the Cu matrix of the MMC for enhanced adhesion, resulting in good mechanical properties of the compound. The optimization consists of, first, tailoring the nanoscopic interface by depositing different interlayers to achieve a form closure plus adhesive bond, and second, by nano- and microstructuring of the fiber to improve the mechanical interlocking. The optimized interface properties are investigated through pull-out measurements of single matrix-coated fibers.

The thin interlayers are deposited by magnetron sputtering and subsequently heat treated according to the synthesis and operation temperatures of the MMC in the divertor. The nanostructure, composition, stress state and texture of the interface layers were investigated with sophisticated characterization techniques including Rutherford backscattering spectroscopy, X-ray diffractometry and different microscopy methods. By applying thin 500 nm graded W/Cu coatings, stepwise and continuously, with subsequent heat treatment at 800°C, the interfacial adhesion between W and Cu could be improved by at least a factor of 6. In addition, neutron diffraction investigations and thermal cycling on multi-fibers MMCs indicate that the graded transition between W fiber and Cu matrix acts as a stepwise adaptation of coefficients of thermal expansion (CTE) mismatch leading to stress reduction at the fiber/matrix interface.

Different microstructuring concepts like ion sputtering, chemical etching, and fiber twisting are performed to modify the tungsten fiber surface to achieve enhanced interfacial adhesion between the W fiber and the Cu matrix. The morphology, roughness, and

strength of the microstructured fibers are characterized on several length scales. The different microstructuring concepts have varying impacts on the fiber surface, ranging from smoothing effects due to ion sputtering, increased roughness due to chemical etching, or surface cracking due to fiber twisting. Tensile tests demonstrate that the surface modifications weaken the ultimate tensile strength of the fibers. However, the single fiber pull-out tests show that an increase in interfacial shear strength is achieved by the microstructuring concepts with the exception of ion sputtering. The optimal interface and microstructuring concept was determined to be a continuously graded W/Cu_{PVD} interlayer plus 800°C heat treatment with chemical etching of the fiber. Two monoblock mock-ups consisting of the optimized interface MMC were tested under high heat fluxes. The fibers remain stably embedded in the matrix under high heat fluxes of up to 10.5 MW/m^2 guaranteeing good thermo-mechanical performance of the whole component. High heat flux test results demonstrate the successful application of the implementation of this novel W_f/Cu MMC.

Contents

Chapter 1

Introduction

1.1 Motivation

The first realistic attempt to solve the world's energy problems by means of fusion power date back to the 1950s. Although the current scientific understanding and technological capabilities still need further improvement, the research activities carried out world wide are making steady progress. Several fusion experiments have been built with the main aims to understand the underlying physical principles and, more importantly, to address the material issues which are experienced when dealing with the unique and extreme loading scenarios. In this context the next challenge, addressed in the fusion experiment *ITER* in Cadarache (southern France), is to exceed the break even point, meaning the generation of more output power than input power is consumed [1]. The start up of this machine is scheduled for the end of 2018. Already, the research and development phase for *DEMO*, the successor of ITER ($\approx$ 2040) aimed at demonstrating the feasibility of fusion as a commercial power source, has started.

The most attractive fusion reaction for energy generation is the fusion of the hydrogen isotopes, deuterium (D) and tritium (T), due to their large cross-section at relatively low temperatures of about 100 Mio. K [2]. The reaction products are helium and an high-energy neutron.

$$\mathrm{D} + \mathrm{T} \longrightarrow {}^{4}\mathrm{He}\,(3.5\,\mathrm{MeV}) + n\,(14.1\,\mathrm{MeV}) \tag{1.1}$$
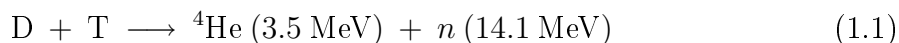
The hot plasma is thermally insulated from the material surroundings by magnetic confinement [2]. Heat is generated by neutrons and high-energetic particles impacting the wall materials (blanket and divertor). The heat is then removed by flowing coolant fluids which in turn produce conventional electrical energy via steam generators.

The highest heat load inside a fusion reactor is found in the *divertor* located at the bottom of the reactor. The divertor system (consisting of the baffle, dome, inner and outer wing and vertical target) is responsible for heat removal, as well as for exhausting the He-ash, unburned D and T and other impurities [3]. The choice of materials is limited to those that meet certain requirements including mechanical and thermo-physical properties, radiation effects, chemical compatibility and corrosion issues, material availability, cost and joining technology, as well as safety and waste disposal aspects [4,5].

For DEMO heat fluxes between 15 and 20 MW/m² in the divertor region are expected [6]. According to the European Power Plant Conceptual Study (PPCS) (Model A) [7,8], the heat has to be removed efficiently from the tungsten (W) plasma-facing material (PFM) to the joint water-cooled heat sink material, the copper alloy (CuCr1Zr) tubes. Due to the mismatch in the coefficients of thermal expansion (CTE) between the W ($4.2 \times 10^{-6} K^{-1}$) and CuCr1Zr ($17.6 \times 10^{-6} K^{-1}$) heat sink, a soft intermediate Oxygen Free High Conductivity (OFHC) Cu layer is included [9]. From ITER research and development (heat flux tests and neutron irradiation campaign) [10], the monoblock design concept was shown to have higher thermal resistance, defect tolerances and better thermal fatigue behavior than other concepts like the flat tile concept [11]. This "low temperature divertor" concept (monoblock design) tolerates heat flux of 15 MW/m² with a coolant temperature of 150°C. For efficient energy production, increase of the cooling water temperature to at least 300°C is desired. This would lead to temperatures of up to 550°C at the interface between the PFM (W) and heat sink material (CuCr1Zr) [12]. However, the mechanical properties of the current Cu-based material at this high temperature are insufficient [13]. Due to the temperature gradient and different CTE between W and Cu-based materials, high stresses occur at the interface of PFM and the heat sink material. Furthermore, Cu-based materials like CuCr1Zr or OFHC Cu are prone to embrittlement under neutron irradiation below 200°C and to irradiation induced creep above 350°C [9].

One solution proposed is a novel optimized water-cooled monoblock divertor consisting of W as PFM, brazing foil as bonding material, W_f/Cu metal matrix composites (MMC) as reinforcement of the critical zone between PFM and the CuCr1Zr cooling tube (Figure 1.1). A W fiber-reinforced Cu MMC has the potential to strengthen the interface of PFM and the heat sink material and may provide a highly creep resistant alternative to conventional Cu-based materials for operation at high temperatures [14,15]. MMCs also offer a wide range of material properties for tailoring the interface. The attraction of W_f/Cu MMC for its use as heat sink material in fusion application is twofold: (1) The W fibers provide the necessary strength of the compos-

ite at high temperatures, while (2) the Cu matrix provides the required high thermal conductivity for efficient heat removal in the cooling system. Further details on the potential and current status of W_f/Cu MMC are summarized in chapter 3.3, while Table 1.1 summarizes the requirements and goals of novel divertor components.

Table 1.1: *Operating conditions and requirements of novel divertor components (revised from [7, 8])*

Structural material	CuCr1Zr
Armour material	W
Intermediate layer	Novel composite material (W_f/Cu MMC)
Temperature at intermediate layer	500-550°C
Cooling Temperature	Water 300°C
Divertor Peak load	15 MW/m^2
Average neutron wall load	2.2 MW/m^2
Continuous operation time	5 years
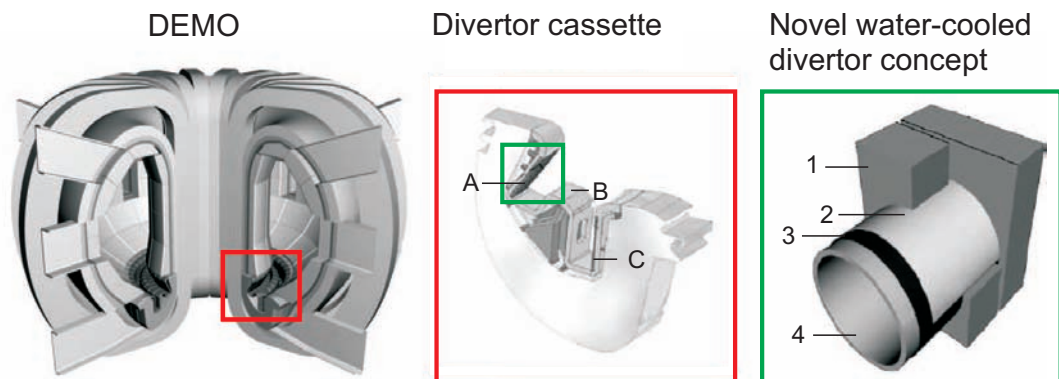
Figure 1.1: *Cut-away view of the fusion power core of future fusion reactors with the divertor cassette comprising of A) outer vertical target, B) dome and C) inner vertical target. In the second blow-up the novel optimized water-cooled monoblock divertor concept is presented including 1) W plasma-facing material, 2) brazing foil 3) W_f/Cu MMC and 4) CuCr1Zr cooling tube (revised from [8])*

1.2 Purpose

The goal of this thesis is the development, optimization and validation of an advanced W_f/Cu MMC as an efficient high temperature heat sink material in water-cooled monoblock divertors for future fusion reactors like DEMO. A stable interface between the W fiber and the Cu matrix is a basic requirement for achieving good mechanical

properties of the MMC. Therefore, the main focus of the work is the optimization of the interface between W fiber and Cu matrix to produce better adhesion.

In the absence of chemical bonding (see chapter 3.2) of W and Cu, the interfacial adhesion can be adjusted by controlling the degree of interfacial roughness, the thermal mismatch between the Cu matrix and the W fiber-reinforcement and the temperature gradient.

In this work two main objectives are pursued to improve the interface between W fiber and Cu matrix:

1. Tailoring the nanoscopic interface by depositing different interlayers to achieve a form closure plus adhesive bond.

2. Nano- and microstructuring of the fiber to improve the mechanical interlocking.

Therefore, different interface and microstructuring concepts were developed, realized, characterized on several length scales and mechanically validated. The best concepts were unified in MMCs, processed in two monoblock mock-ups and tested under high heat fluxes. The concepts are presented in detail in chapter 2.

1.3   Strategy of the work

The basis of the work is the interface optimization comprising the fiber microstructuring and the fiber coating. Each concept is well characterized and mechanically investigated (see Fig. 1.2). The best concepts were unified and applied in the MMC and then implemented into the synthesis of the monoblock mock-up.

Therefore, the following emphases were thoroughly investigated and characterized by sophisticated methods:

- Deposition of different fiber coatings for optimal interfacial adhesion

- Fiber surface microstructuring for optimal mechanical interlocking between W and Cu

- Combination of best microstructuring and interface concepts within a MMC

- Implementation of results in the development of monoblock testing devices for heat flux experiments at GLADIS

Background information on thin films, W/Cu interface and current status of W_f/Cu MMCs is summarized in chapter 3. A review of the main applied characterization techniques is given in chapter 4. The experimental details, as well as the results and discussion, can be found in chapter 5 and 6.
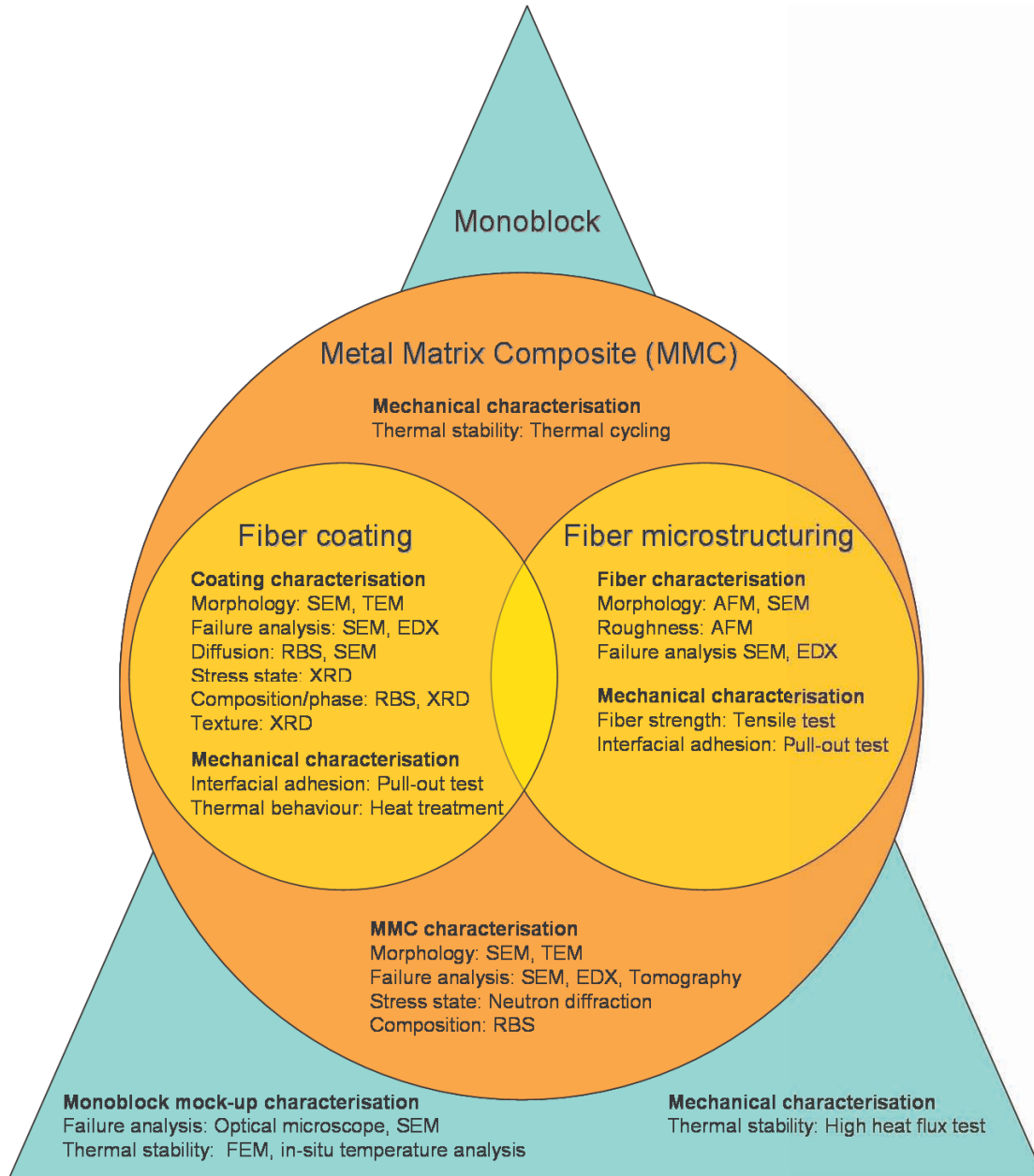
Figure 1.2: *The basis of the work is the interface optimization comprising the fiber microstructuring and the fiber coating. Each concept is well characterized and mechanically investigated. The best concepts were unified and applied in the MMC and then implemented into the synthesis of the monoblock mock-up.*

Chapter 2

Interface optimization concepts

This chapter presents and summarizes all investigated interface and microstructuring concepts used to improve the interface between W fiber and Cu matrix. A nomenclature for each concept was introduced for clarity and can be found in Table 2.1.

2.1 Interface concepts

The interlayer coatings have to fulfill two essential requirements:

- Thermal stability during operation (long duration) of the monoblock at temperatures between 300°C - 550°C

- Thermal stability at temperatures occurring at the material component syntheses like outgassing at 550°C and consolidation process at 650°C (chapter 5)

Five different interface concepts were chosen to improve the interface between fiber and matrix, which was applied by an electroplating process:

A) Direct interface between W fiber and the Cu matrix without deposited interlayer;

B) W fibers coated with a thin Cu interlayer by magnetron sputter deposition and then encased with the Cu matrix;

C) W fiber coated with a stepwise graded transition to the Cu matrix by magnetron sputter deposition;

D) W fiber coated with a stepwise graded transition to the Cu matrix by magnetron sputter deposition plus subsequent heat treatment at 800°C;

E) W fiber coated with a continuously graded transition to the Cu matrix by magnetron sputter deposition plus subsequent heat treatment at 800°C.

The ideas behind the choice of interlayers are explained as follows:

- Interface concept A serves as the reference interface. The W fibers are directly electroplated with the matrix material, Cu. The thickness of the electroplated Cu layer defines the fiber volume content when the fibers are processed to composites.

- Concept B is expected to achieve a stronger mechanical interlocking due to the fine nanostructure of the thin PVD Cu layer filling the coarse grooves of the W fiber.

- It is hypothesized that concept C, the stepwise graded transition from W fiber to Cu matrix, will achieve a macroscopic interlocking within the interlayer, in addition to the nanoscopic interlocking between the Cu and W. Furthermore, the transition should act as a stepwise adaptation of the coefficient of thermal expansion (CTE) of W and Cu during thermal cyclic loading. To reduce thermally induced stresses of W and Cu, numerous successful investigations were performed on W/Cu functionally graded layers used in fusion application produced by different techniques like powder metallurgy, electrochemical processing, infiltration and plasma spraying on mm-scale [16–22]. In this work, the investigated interlayers are in the nanometer scale and are produced by magnetron sputtering.

- Interface concept D was chosen to combine mechanical interlocking, between fiber and matrix and within the interlayer, with adhesive bonding at the W fiber/interlayer interface. Thermal treatment was applied to achieve W/W bonding. At 800°C, higher W diffusion processes were expected, resulting in a good bonding between the initially coated W layer and the W fiber.

- Concept E mimics the ideas of concept D but is realized with a continuously graded interlayer for a smoother transition between W and Cu resulting in a better adaptation of CTE.

2.2   Microstructuring concepts

In order to optimize the mechanical interlocking, six different microstructuring concepts were chosen to modify the tungsten fiber surface on nanometer and micrometer scale:

Ion sputtering I), chemical etching II), fiber twisting to III) 20° and to IV) 30°, and combinations of fiber twisting and subsequent chemical etching V) and VI) were performed.

Table 2.1: *Overview and nomenclature of the a) interface and b) microstructuring concepts*

a)	Nomenclature	Interface concept
	A	No interlayer
	B	Cu_{PVD} interlayer
	C	Stepwise graded W/Cu_{PVD} interlayer
	D	Stepwise graded W/Cu_{PVD} interlayer + 800°C heat treatment
	E	Continuously graded W/Cu_{PVD} interlayer + 800°C heat treatment
b)	Nomenclature	Microstructuring concept
	0	Initial
	I	Ion sputtering
	II	Chemical etching
	III	Twisting 20° ± 4°
	IV	Twisting 30° ± 4°
	V	Twisting 20° ± 4° + chemical etching
	VI	Twisting 30° ± 4° + chemical etching

All six concepts aim to increase the surface roughness, thus achieving a surface enlargement, which results in an optimized form closure.

It was assumed that the tensile strength of the fibers decreases through twisting, i.e., plastic deformation of the fiber, while on the other hand the interfacial adhesion increases. To find a balance between interfacial adhesion and fiber strength, the twisting angles were chosen to be 20° and 30°.

Chapter 3

Background knowledge

This work deals with multiple problems and requires understanding of various research fields. This chapter focuses on summarizing the relevant basics in thin film technology including the deposition process, growth mechanism and the related stress state of the films. The interface between W and Cu is described and adhesion test are introduced. Furthermore, the potential and current status of W_f/Cu metal matrix composites (MMC) development are reviewed.

3.1 Thin films

As different interlayers are investigated to optimize the adhesion at the W/Cu interface, thin film technology plays a key role in this work. Various factors control the adhesive property of thin films (thin $\hat{=}$ thickness $\leq$ 1μm), such as deposition process, surface state of the substrate, growth and the intrinsic stress in thin films [23]. In the following, the relevant knowledge concerning the production, growth mechanism and stress state of thin films is briefly presented.

3.1.1 Magnetron sputtering

Atomistic deposition processes such as physical vapor deposition (PVD) and chemical vapor deposition, provide a spectrum of possibilities in tailoring thin films. The most established methods to produce thin films are PVD processes. PVD is a vacuum-based coating technology used to deposit thin films of various materials onto various surfaces. Variants of PVD include evaporative deposition, sputtering, as well as reactive types of these processes [24]. As the sputtering deposition process is relevant for this work it is briefly introduced. More details can be found in Ohring [25].

During sputtering, the target material is transformed into vapor, transported to the substrate and then deposited on the substrate surface forming the thin film. For the sputtering process, ions are supplied by an inert gas ionized through glow discharge (plasma) between the target as cathode and the substrate holder as anode. The generated ions are accelerated toward the cathode (the target) and sputter atoms out of the target material, which is transformed into vapor. The vapor mainly consists of neutral target atoms and reflected gas ions. The energy of the sputtered atoms is in the range of a few eV, while the reflected gas ions can be in a range of hundreds of eV depending on the shield potential. Details of the underlying ion-surface interaction processes leading to a sputtered surface atom can be found in [25–27].

The deposition on the substrate depends on two factors: gas pressure and bias, a negative voltage between substrate and ground. The gas pressure determines the mean free path of the target particle. The higher the gas pressure, the smaller the mean free path and the smaller the kinetic energy of the impinging particles. The bias accelerates the gas ions onto the substrate leading to rearrangement and sputtering during the film growth. The higher the bias, the higher the kinetic energy of the impinging ions.

The magnetron configuration is used to catch free electrons in front of the target surface due to the additional magnetic field [28]. The higher electron density leads to collision ionization and to higher Ar ion density. These effects result in a higher sputtering yield.

3.1.2   Micro- and nanostructure of thin films

The growth, hence, the characteristics and functionality of the films depend strongly on the physical, mechanical and chemical properties of the substrate surface. Surface roughness leads to less dense film growth due to geometrical effects [29, 30].

For polycrystalline films a profound understanding of the growth mechanism has been collected for several years. There is a strong relation between the microstructure of thin films on atomistic scale and the intrinsic stress. The possible range of microstructures of evaporated coatings influenced by the deposition temperature were firstly shown in the structure zone model by Movchan and Demchishin and has been reviewed in many publications [31–33]. This model was later extended by Thorton in 1989 [34] for sputtered coatings and by Messier 1984 [35] regarding the influence of bias-controlled ion energy. Another established growth model of sputtered films with related stress mechanisms is proposed by Windischmann in 1991/1992 [36, 37].

The nucleation stage and the thermodynamics at the beginning of the film deposition influence the film growth mechanism, i.e., the morphology of the film. Three

different film growth modes can be distinguished for epitaxial growth. The *Volmer-Weber mode* describes the growing of three-dimensional (3D) islands on the substrate. The film growth proceeds to columnar grain growth due to self-diffusion of the film material or to lateral grain growth due to recrystallization processes. In the *Frank-Van der Merwe mode*, the films wet the substrate and two-dimensional (2D) islands are formed layer by layer. The third growth mode is the *Stranski-Kastanov mode* describing 3D islands which nucleate on top of one or a few monolayers.

The continuous growth process is controlled by kinematic processes. Therefore, different defects lead to stress evolution in the films (see chapter 3.1.3).

Polycrystalline thin films grow by *Volmer-Weber mode* without a preferential direction. The initial islands and later the grains have a random orientation within the plane and are highly influenced by the mobility of the atoms. Two distinguishable modes are possible: *Low-mobility* Volmer-Weber growth of high melting point film materials is characterized by columnar grain growth and shadowing effects in the microstructure [38]. On the other hand, *high-mobility* Volmer-Weber growth of low melting point film materials is characterized by surface and self-diffusion of the film atoms resulting in proceeding lateral grain growth and dense microstructure.

Due to the dependence of the mobility of the film atoms, polycrystalline films are highly influenced by substrate temperature (activating the mobility), O_2 partial pressure (reducing the mobility), ion bombardment and impurity content. Zhang investigated (2003) [39] the effect of sputtering conditions, in particular the impact of substrate temperature on the microstructure and tribological properties of W coatings. At a temperature of 1100°C, the microstructure was densely packed leading to strong and wear resistant coatings compared to the one with a high density of voids deposited at 400°C. In turn, low adatom mobility combined with oblique angle of vapor incidence conditions and atomic self-shadowing control can create sculptured columnar thin films in various shapes like helices and zigzags [40–42].

3.1.3 Residual stress in thin films

The residual stress at the interface is the key element of the adhesion of W and Cu. The large amount of papers concerning stresses in thin films and coating demonstrates the high interest in this field. The pioneer work was performed by Stoney in 1909 [43]. Since this time many methods of measurements and theories have been developed to explain the mechanism and the evolution of residual stress in thin films. This was reviewed by Hoffman in 1976 [44], Bravman, Nix, Barnett and Smith in 1989 [45], Koch in 1994 [46], Spaepen in 2000 [47] and Janssen in 2007 [48]. They present a

thorough discussion of today's understanding of the growth of thin films and review the related atomistic mechanisms responsible for intrinsic stress.

Depending on the scale at which the matter is analyzed, three kinds of residual stresses are distinguished [49]: Residual stresses of the *1st kind*, macro stresses, are position-dependent and averaged over all crystallites and phases within the considered volume; the *2nd kind* are homogeneous micro stresses within a crystal; and the *3rd kind* are inhomogeneous micro stresses within a grain.

In thin films residual stresses of the *1st kind* are composed of thermal and intrinsic stress.

$$\sigma_{residual} = \sigma_{th} + \sigma_{intrinsic} \tag{3.1}$$

Thermal stresses (σ_{th}) result in a difference in the thermal expansion coefficient of the substrate (α_s) and the film (α_f) and can be determined by elastic mechanical properties (E_f, ν_f) of the film. Murakami [50] presented the calculation of the thermal stress by the following equation:

$$\sigma_{th} = \frac{E_f}{1 - \nu_f} \int_{T_0}^{T} (\alpha_f - \alpha_s)\, dT \tag{3.2}$$

The intrinsic stress originates from strained regions

- within the films like grain boundaries, dislocations, voids and impurities

- at the film/substrate interface due to lattice mismatch

- at the film/vacuum interface due to surface stress, adsorption, etc.

- due to dynamic processes like recrystallization and interdiffusion of film material during the deposition.

Whereas low-mobility Volmer-Weber growth leads to tensile stress at the small-angle boundaries separating the randomly oriented grains, high-mobility Volmer-Weber growth leads to a compressive stress due to a sum of grain boundaries, recrystallization and capillary stress [46]. To summarize, tensile stresses as well as compressive stress may lead to cracking and buckling of the films. Thus, tailoring of the stress state improves the conditions of film preparation to guarantee the functionality of the film or even of the whole component.

Measurement of residual stresses

The measurement of residual stresses can be divided in two types: destructive and non-destructive techniques.

The *destructive* methods are based on destruction of the state of equilibrium of the residual stress, e.g., layer removal during scratch test [25] or hole-drilling method. These techniques are only sensitive to the 1st kind of residual stress.

Non-destructive techniques are based on the relation between the physical and crystallographic parameters and the residual stress. Stress in thin films can be determined in two ways: (1) by measuring the elastic deformation of the substrate and (2) by directly measuring the crystal lattice strain in the film using X-ray or neutron diffraction.

From the elastic bending of the substrate due to the intrinsic stress, the curvature of the wafer can be determined. Since the elastic properties of the wafer are known, the stress in the film can be calculated. In the bi-axial rotationally symmetric case and under the assumption that the thickness of the film is much smaller than that of the substrate, the stress state can be calculated by the well known Stoney equation [43,51]. The bending of the substrate can also be measured in-situ via laser as reported by Pletea [52] and Fitz [53] or by use of a commercial strain gauge reported by Cremona 2000 [54]. In-situ stress measurement, in combination with microstructure investigation, can lead to a better understanding of the stress generating mechanisms in thin films.

The most efficient representative of the *non-destructive* techniques is the X-ray diffraction method using the lattice spacing as a strain gauge. It makes studying and separating the three kinds of residual stress possible. Residual stresses of the 1st kind cause a change in the lattice spacing leading to peak shift of the diffraction peak. Residual stresses of the 2nd kind are not expected in thin films [55] and residual stresses of the 3rd kind lead to a peak width increase. An excellent review has been published by Welzel in 2005 [56].

In this work, X-ray diffraction were used to analyze the stress state of the deposited interlayers. More experimental details about the XRD set-up and constitutive equations can be found in chapter 4.3 and chapter 5.3.3.

3.2 Interface of W/Cu

A detailed interface specification of W and Cu is relevant for the production or synthesis of W_f/Cu MMC. In general, interfaces (including abrupt interface, chemical bonding, diffusive mixing and mechanical interlocking) must withstand the shear forces caused by thermal and intrinsic stress.

Due to the insolubility of W in liquid Cu [57, 58] the "Cu-W alloys" reported in the literature [59] are prepared by liquid-phase sintering of mixed W and Cu powders at temperatures higher than the melting point of Cu ($T_{melt} \approx 1085°C$). Phase equilibria studies of the ternary systems W-Cu-Al [60] and W-WSi$_2$-Cu [61] showed negligible mutual solubilities of Cu and W at $\approx 600°C$ and $800°C$, respectively. The mutual solubility of W and Cu at higher temperature is negligible. Co-evaporation of W/Cu amorphous thin film (28 - 55 at % W) reported by Nastasi [62] showed that the as-deposited, the heat treated and the ion treated specimens form intermediate metastable structures.

It is well known that Cu wets W well so that a good adhesion at the interface is predicted. The degree of wetting is the result of the formation of chemical equilibrium bonds achieved by the mutual saturation of the free valences of the contacting surfaces (van der Waals forces). The non-existence of chemical reactions defines the wetting as non-reactive. A contact angle measurement, performed at IPP, determined an angle of 65° between the W substrate surface and the surface of the Cu liquid molt on the surface. As the wetting angle is < 90°, good wetting of Cu on W can be confirmed.

The chemical potential between W and Cu can be regarded as in a thermodynamic equilibrium. Therefore there will be no driving force for a chemical reaction (see [57]). Potential diffusion reactions at elevated temperatures were investigated within this work and can be found in chapter 6.1.1.

As W and Cu seem to be a non-reactive component with purely a mechanical bond at the interface, Kerans and Parthasarathy [63] estimate the radial stress σ_r at the fiber/matrix interface due to roughness induced gripping:

$$\sigma_r = \frac{-E_m E_f}{E_f \cdot (1 + \nu_m) + E_m \cdot (1 - \nu_f)} \cdot \left[\frac{A}{r}\right] \tag{3.3}$$

where E is the Young's modulus, ν is the Poisson's ratio, A is the roughness amplitude, r is the fiber radius and the subscripts m and f indicate the matrix and the fiber, respectively.

These equation can be adjusted by the contribution due to thermal mismatch between the reinforcement and the matrix [63]. The compressive radial stress increases with roughness amplitude and decreases with fiber radius. Thus, the degree of interfacial bonding can be controlled in the absence of chemical bonding by controlling the degree of interfacial roughness, the thermal mismatch between matrix and fiber and the amplitude of temperature change.

Interface adhesion

Besides the qualitative methods (e.g. tape test and thermal shock test [64]) and the semi-quantitative methods (e.g. acoustic methods, scratch test [65]), there are also methods to investigate the adhesion of thin films quantitatively. This includes e.g. indentation test [66–68] or resistance measurements [69]. Different adhesion test methods for thin hard coatings on planar substrates was critical reviewed by Valli in 1986 [70].

To determine the interface adhesion for more complex geometries like fiber/matrix interface, different techniques are proposed. The most common techniques to obtain quantitative information about the interface strength of fiber-reinforced materials are pull/push-out tests [71, 72]. Details about the underlying mechanisms can be found in Kim [73] reviewing the existing theories of fracture toughness of fiber composites and the various methods for improving the fracture toughness by means of interface control.

As the W fibers exhibit a brittle behavior at room temperature leading to splitting of the fiber, experimental pull-out test were performed in this work to determine the interfacial shear strength and interfacial friction stress by pulling single fibers out of the matrix. Experimental details are presented in chapter 5.4.2.

3.3 Potential and current status of W_f/Cu MMC

Besides its application in fusion reactors, MMC with superior thermal properties designed for heat sinks under extreme conditions successfully find use in microelectronics and aerospace. The properties including Young's modulus, strength, toughness and thermal characteristics of composite materials can be tailored in a wide range [74]. Reinforcements comprising particles, whiskers, as well as short, long or continuous fibers can be embedded into the high thermal conductive Cu matrix.

Although known for decades as an ideal model system to analyze the properties of metal matrix composites [75, 76], W_f/Cu MMC has never been industrially employed [77] and the most effective production route must still be found [78]. This chapter concentrates on a brief description of long W fiber-reinforced Cu composite material and its synthesis process. Table 3.1 shows a comparison of the mechanical and physical properties of W fiber, CuCr1Zr alloy, Cu and the alternative reinforcement SiC-fiber. Due to the higher thermal conductivity of W compared to SiC and its formability, W was selected as a more promising reinforcement in MMC for fusion application.

Nevertheless, the material compound W_f/Cu can benefit from generated basic knowledge of the SiC_f/Cu and $SiC_f/Eurofer$ systems regarding the synthesis process.

Table 3.1: *Mechanical and physical properties of the components of the W_f/Cu-MMC and of CuCr1Zr and SiC fiber*

Material	Young's modulus [GPa]	Ultimate tensile strength [GPa]	Density at 20°C [g/cm3]	Linear CTE at 20°C [ppm/°C]	Thermal conductivity at 20°C [W/mK]
W fiber [79]	410	4.1	19.3	4.5	164
SiC fiber [80]	380	3.9	3.0	4.1	16 [81]
Cu [82]	110	0.2	8.96	16.4	385
CuCr1Zr, precipitation hardened [83]	110 - 130	4.8 - 5.1	8.91	17.6	310 - 330

SiC-reinforced copper composites have been investigated at IPP for several years. The research program has been focused on the development and characterization of SiC_f/Cu MMC [84–87], as well as on the interface optimization of $SiC_f/Eurofer$ MMC [88,89] and SiC_f/Cu MMC [90,91].

In the frame of the European Integrated Project ExtreMat [92], parallel development of W_f-reinforced Cu heat sink materials incorporated in W monoblock has been performed by Max-Planck-Institute for Plasma Physics, Institute for Material Research of DLR in Cologne [81], and Institute for Material and Machine Mechanics of Slovak Academy of Science (IMSAS) in Bratislava [93]. The different developed monoblock mock-ups by the three groups will be investigated in respect of heat resistance in the high heat flux testing device JUDITH [94]. The testing campaign will be finished at the end of the year 2008.

3.3.1   W fiber

W has an abnormal lattice strength (tensile strength of W single crystal is $\approx$1.1 GPa) [95] at temperatures of up to 800°C. The internal crystalline strength is much higher than the cohesion between the single crystals (grain boundary strength). This explains its extraordinary properties like high tensile strength compared to other metals which otherwise leads to special treatments in its application and machining. Transverse to the fiber, the bonding is weaker and deformations in this direction lead to splitting of the fiber in single phase.

To reduce the high brittle-ductile transition temperature, rhenium (Re$\leq$3%) can be doped to W fibers without significant reduction of mechanical properties. Regarding the mechanical properties at high temperatures, thoriated or potassium-doped W

fibers can be taken into consideration to increase the high temperature strength and recrystallization temperature [79].

Due to its high recrystallization temperature ($\approx$1350°C), high tensile strength, fracture toughness, fatigue resistance at high temperatures, non-hydrid-builder properties and neutron irradiation resistance combined with its availability in a wide range of diameters, W fibers were selected as Cu reinforcement in this work.

3.3.2 Cu and CuCr1Zr

Cu alloys, in particular precipitation hardened CuCr1Zr (Cr 0.5 - 1.2%, Zr 0.03 - 0.3%, rest Cu [83]), was selected for heat sink materials in ITER due to its good weldability and its high fracture toughness at high temperatures [10]. CuCr1Zr exhibits a homogeneous α-structure in the solution-annealed state and crystallizes in a face-centered cubic (fcc) body. Through aging under the solubility temperature, Cr and Cr_2Zr phases precipitate out of the oversaturated matrix. The precipitates are homogeneously dispersed. CuCr1Zr can be used in temperature ranges of up to $\approx$450°C before dissolving its precipitation, which can be restored by thermal treatment [96, 97].

In this work CuCr1Zr was selected as cooling tube for the monoblock mock-up. Pure Cu was chosen as matrix material for the synthesis of MMC based on the difficulties to produce electroplated CuCr1Zr coatings.

3.3.3 Interface

Interface optimization between W fiber and Cu matrix via Cu deposition , graded W/Cu coatings or via microstructuring (presented in chapter 2) has never been reported in the literature. An alternative option to enhanced adhesion of Cu-W thin films on tungsten substrate was proposed by Zhou [98]. The technique of "ion beam assisting bombardment implanting of W particles" can improve the adhesive property of Cu-W thin films on steel substrate. A further possibility is tailoring the interface with different alloying element interlayers forming chemical bonds between the fiber and the matrix [76]. Deterioration of the thermal conductivity of the Cu matrix must be assumed even through small amounts of impurities [99, 100]. Additionally, different elements can lead to a decrease of the fiber strength due to destructive diffusion processes as observed in the SiC_f/Cu system described in Köck's work [90].

3.3.4   Production techniques

Numerous production or synthesis techniques of W_f/Cu MMC are reported in the literature [74]. The MMC can be synthesized out of liquid phase like gas pressure infiltration [78], metal injection molding [101] and spray deposition, or out of the solid state like vacuum diffusion bonding technologies including powder metallurgy and matrix-coated fiber technology [102, 103]. The favored route for W_f/Cu MMC, briefly presented, are gas pressure infiltration, vacuum diffusion bonding technology by foil-fiber-foil arrangements and matrix-coated fiber technology.

Gas pressure infiltration procedure uses molten Cu in combination with gas pressure applied on the melt surface to penetrate aligned W fibers. Due to the good wettability from W and Cu this simple method can be used to produce unidirectionally aligned reinforcements with possible high fiber volume fraction. However, the high infiltration temperature of 1200°C leads to degradation of the W fiber resulting in a decrease of mechanical properties of the reinforcement [79, 95, 104].

For the *vacuum diffusion bonding* process W fibers are aligned between Cu foil and subsequently consolidated at temperatures of up to 900°C at a pressure of 100 MPa [74]. These monolayers are stacked for the production of components. A homogeneous fiber distribution in the final component with high volume fraction is challenging due to the unstable alignment of the fibers leading to an undesirable fiber-fiber contact with high failure rate. Additionally, contamination through impurities such as oxides and carbides can occur.

The patented *matrix-coated fiber* technology developed by DLR [102, 103] shows promising advantages. The process includes a sputtering process of the reinforcement with the desired interlayer, bundles encapsulated under vacuum and finally hot isostatic pressing at 650°C and 1000 MPa leading to consolidation. This clean technique guarantees a homogeneous fiber distribution. The thickness of the fiber coating defines the fiber volume content in the composite. In this work the matrix-coated fiber technology was chosen to synthesis the optimized MMC.

3.3.5   Mechanical properties

A stable interface between the W fiber and the Cu matrix is a basic requirement for achieving good mechanical properties of the MMC. In this work the macromechanical properties of the MMC, like tensile strength and Young's modulus, were not investigated. The main focus of the MMC investigation was the micromechanical properties like stress state of fiber and matrix and the fatigue behavior during thermal cycling.

However, theoretically, the rule of mixtures predicts the behavior of composites

under stress assuming that the fiber and matrix have equal strain. MMC with brittle, small diameter fibers have indicated that failure can take place at lower tensile and cyclic stresses than at those predicted by theory [105]. Incorporation of damaged fibers and poor fiber-matrix bonding during fabrication weakens the composite as well as possible interfiber contact and inhomogeneous plating. A detailed model for fatigue fracture behavior of brittle W monofilament-reinforced multicrystalline ductile Cu composites was proposed by Zhang in 2001 [106]. At low applied plastic strain amplitude (1×10^{-4}) multiple matrix cracks are involved in the fatigue process propagating to the fiber and finally leading to fiber break. Whereas at intermediate plastic strain amplitude (5×10^{-4}) one fatal single matrix crack, occurring preferably at the Cu grain boundaries, dominates the process. At high plastic strain amplitude (1×10^{-3}) a single fiber can break resulting in a quick failure of the composite. Fatigue mechanisms of W_f/Cu composite have been investigated in the past 20 years [107, 108]. These works mainly focused on crack propagation whereas fundamental micromechanisms of fatigue behavior, such as, strain localization, crack initiation and their related microstructure evolution in the Cu matrix is still challenging.

Chapter 4

Characterization techniques

Characterization is one focus of this work and serves as basis for the validation process of the different concepts. All relevant characterization techniques applied in this work are briefly itemized.

4.1 Electron microscopy - SEM, FIB and TEM

An optical microscope is used for surface analysis with resolutions of up to 300 nm. For higher magnification Scanning Electron Microscopy (SEM), detecting Secondary Electrons (SE) and Backscatterd Electrons (BSE), serves as a high resolution technique for studying the morphology and grain topography. With the additional feature of Energy Dispersive X-ray Spectroscopy (EDXS), the composition of the surface structure can be determined. SEM images rely on imaging surfaces and 3D structure of the sample due to the high depth of field and the brightness of tilted surfaces.

Generally, a focused electron beam (beam size 1 - 10 nm), accelerated by a cathode voltage between 1 - 30 kV [109], is scanned over the sample surface under vacuum. The current of the SE (collision ionization generated electrons) or BSE (quasi elastically scattered primary electrons) are detected and define the intensity of the corresponding pixel displayed in the image. Besides SE and BSE, X-rays are also generated due to the bombardment with the electron beam. Detailed descriptions of the functional principle of the SEM can be found in [110].

The Focused Ion Beam (FIB) uses a focused beam (beam size 4 - 6 nm) of gallium ions, accelerated to an energy of 1 - 30 keV, to sputter atoms from the surface. Thereby, the implantation of Gallium atoms into the top few nanometers of the surface cannot be avoided, which may lead to modifications of the crystal structure. The FIB is used for cross-section polishing prior to SEM analysis of materials and as an ion beam milling

tool to thin samples until they are transparent to electrons for Transition Electron Microscopy (TEM) analysis.

Generally, for TEM a time consuming preparation process of polishing, thinning and perforation must be performed to produce areas of uniformly electron transparent materials (thickness < 0.5 µm). The TEM resolution (> 0.1 nm [109]) can be about an order of magnitude greater than the SEM resolution (> 1 nm). For TEM analysis an electron beam accelerated with cathode voltage between 80 - 400 kV, is transmitted through the thin transparent sample. An image is formed from the electrons transmitted through the specimen, magnified and focused by an objective lens and can be detected by a CCD camera.

In this work the SEM was used for fiber and coating characterization and fracture analysis. Post experiment investigations of the MMC and monoblock mock-up were performed by optical microscope and SEM. TEM was applied for coating characterization. FIB was used as an effective tool for sample preparation.

4.2   Atomic Force Microscope (AFM)

The Atomic Force Microscope developed by Binnig et al. in 1986 [111] is a combination of the principles of scanning tunneling microscope and the stylus profilometer. It relies on the scanning technique to generate high resolution 3D images of a surface in the nanoscale [112]. A small thin tip with a nanometer radius of curvature is mounted at the end of a flexible cantilever and is brought into proximity with the sample surface. Forces (like Van der Waals forces, capillary forces, chemical bonding, electrostatic forces, magnetic forces) between the tip and the sample lead to a deflection of the cantilever. The motion of the cantilever beam is measured by using a laser deflection technique, i.e., the deflection is measured using a laser spot reflected from the top of the cantilever into an array of photo diodes.

Depending on the application, the AFM can be operated in various modes [113]. In the so-called contact mode the samples are scanned against the tip with a constant force. A feedback mechanism is used to adjust the distance between tip and sample to maintain a constant force. The sample is mounted on a piezoelectric tube, for scanning in the x, y and z directions. The resulting map of the area s = f (x, y) represents the topography of the sample.

In this work the AFM data provides information about surface structure features of W fibers on a nanometer scale.

4.3   X-ray Diffraction (XRD)

Non-destructive X-ray diffraction analysis gives information of the crystallographic phase, texture and stress state of materials in depth of up to a few micrometers.

In the crystal lattice atoms are arranged in space such that a series of parallel planes (h, k, l) are separated from one another by a distance d_{hkl}, which varies according to the nature of the material.

When a monochromatic X-ray beam with wavelength λ is projected onto a crystalline material at an angle θ, diffraction occurs only when the distance traveled by the rays reflected from successive planes differs by an integer multible of λ. By varying θ, the Bragg's Law (see 4.1) is fulfilled by different d_{hkl}-spacings in polycrystalline materials. The angular positions and intensities of the resulting diffracted peaks are plotted (diffraction pattern) which is characteristic of the sample allowing the determination of the *crystallographic phase* of a substance by comparing the diffraction pattern with known crystal structures. In the case of different phases, the resulting diffractogram is formed by addition of the individual patterns.

$$2d_{hkl} \cdot sin\theta = n\lambda \tag{4.1}$$

In this work $\theta/2\theta$ scans are performed. The diffraction pattern is formed by changing the X-ray incidence angle by θ and the scattering angle by 2θ. Therefore, the scattered intensity is plotted as function of 2θ.

Texture is the orientation distribution of crystallites of polycrystalline materials and influences its properties. A material in which these orientations are fully random is said to have no texture. In contrast, single crystals with one preferred crystallographic orientation, have a strong texture. For the determination of the orientation of lattice planes via X-ray, the following steps are performed:

- Diffraction angle remains constant so that one specific lattice spacing is chosen

- Sample is tilted and rotated to detect the planes which are not parallel to the surface and which diffract after Bragg's law

- The result, the orientation of grains based on the analyzed plane, is represented using a pole figure where the measured intensity is presented depending on the tilt and rotation angle.

X-ray and neutron diffraction are well established to measure residual *stresses*. Both techniques show strain resolution of ± 10 µstrain but differ in the depth penetration of µm scale and mm, respectively [114].

The methods are based on the use of the lattice spacing as a strain gauge. The residual stresses in this work were analyzed by XRD using the $sin^2\psi$ method/Ω mode. For each inclination of the sample, defined by two angles ϕ and ψ, the strain $\varepsilon_{\phi\psi}$ in the direction normal to the diffracting planes is related to the corresponding lattice spacing d. A relation between the strain and the stress tensor components is then derived through a micro mechanical approach (elasticity theory) of the material.

The complexity of the X-ray analysis strongly depends on the assumptions which have to be made. When the occurrence of texture, anisotropy, stress gradients, etc. has to be considered the complexity of the calculation increases.

Considering the case of a thin and homogeneous film on a substrate, a biaxial residual stress state of rotational symmetry ($\sigma_{13} = \sigma_{23} = \sigma_{33} = 0$ and $\sigma_{11} = \sigma_{22}$) independent of the thickness can be assumed for simplification [115] and is described by the following equation:

$$\varepsilon_{\theta\psi} = \frac{1}{2}S_2^{\{hkl\}}\sigma_\phi sin^2\psi + S_1^{\{hkl\}}(\sigma_{11} + \sigma_{22}) \tag{4.2}$$

with

$$\sigma_\phi = \sigma_1 cos^2\phi + \sigma_2 sin^2\phi \tag{4.3}$$

with

$$\frac{1}{2}S_2^{\{hkl\}} = \frac{\nu^{\{hkl\}} + 1}{E^{\{hkl\}}} \tag{4.4}$$

and

$$S_1^{\{hkl\}} = \frac{-\nu^{\{hkl\}}}{E^{\{hkl\}}} \tag{4.5}$$

The plot of $\varepsilon_{\phi\psi}$ vs. $sin^2\psi$ gives a linear distribution, whose slope allows the stress component σ_ϕ in the ϕ direction of the surface to be calculated [116]. The elastic constants have to be calculated or determined experimentally. One must keep in mind that the use of macroscopic elastic constants is an assumption for thin films due to their microscopic inhomogeneity [115].

4.4   Ion beam analysis

Nuclear reaction analysis (NRA) and Rutherford Backscattering Spectrometry (RBS) are well established ion beam analysis methods for supplying depth resolved composition information in the near surface region [113]. RBS is usually used to measure the distribution of heavy elements in a light matrix. In general, the depth resolved composition of specimen is analyzed with a high sensitivity of up to $\sim 10^{12}$ cm^{-2}and an information depth of up to several µm. Both the sensitivity and the information depth depend on the element and matrix. This makes RBS an attractive candidate for examining thin films and surface modified materials [117].

The specimen is bombarded with light ions (usually H or He) in the MeV range for RBS and NRA measurements. The particles are backscattered and are measured in an energy dispersive spectrometer. The accumulated charge Q on the specimen is also recorded. From the energy of the detected backscattered ions the distribution and the concentration of the elements in the sample can be extracted. Typical RBS spectra exhibit broad signals at different backscattering energies. Signals from the surface and heavier atoms appear at higher energies. To measure light elements in a heavy matrix with RBS causes problems because the spectrum of the ions backscattered from the heavy elements overshadow the ones from the light elements (detailed problem description can be found in [118]). For this case alternative methods like NRA can be used.

The NRA technique detects the reaction product (mainly protons) of the nuclear reaction occurring between the incoming ions and the substrate elements. The proton detector is equipped with a thick stopper foil for filtering the backscattered ^{3}He, so that only high-energetic protons from nuclear reactions are detected. It has a large solid angle for maximum sensitivity. As the cross section of nuclear reaction is larger than the RBS cross section the sensitivity is higher compared to RBS.

RBS is applied for composition analysis of continuously graded W/Cu coatings as well as for stepwise graded coatings after dedicated thermal treatments, and for diffusion analysis of W/Cu diffusion couples. To determine O content in W$_f$/Cu MMC, NRA was performed with ^{3}He$^+$ ions. The tandem accelerator in IPP Garching provides the high energetic ion beams which were used for RBS and NRA measurements in the RKS (Rückstreutopf) endstation.

4.5 High heat flux (HHF) test by neutral beam

The neutral beam facility GLADIS at IPP Garching was constructed for the testing of PFCs under high heat fluxes similar to the expected loads in fusion devices and offers an additional European HHF test facility for the tests of divertor components [119,120]. GLADIS provides thermo-mechanical testing capabilities for high heat loaded water-cooled divertor components with dimensions of up to 2 m length in a water-cooled test vacuum chamber. Two ion sources with max 1.1 MW beam power can be used for heat loading tests in an operating range: 0.2 to 45 MW/m^2 at target position. GLADIS uses a hydrogen beam generated in a RF driven ion source. The technical characteristics and the systems for vacuum generation, cooling, power supply, control, target diagnostics and data acquisition are described in detail by Greuner [119].

HHF test were performed for the evolution of the implemented W$_f$/Cu MMC in the monoblock mock-up.

Chapter 5

Experimental details

Chapter 5 presents the experimental details of the interface optimization between W fiber and Cu matrix including the realization of different interface and microstructuring concepts with the parallel performed characterization. The sample preparation from matrix-coated single fibers to the optimized monoblock mock-up is described in detail.

5.1 Sample preparation and treatment

The sample preparation and treatment, comprised of the deposition process, the realization of the microstructuring as well as the synthesis of the MMC and the monoblock mock-up development, are thoroughly explained.

5.1.1 Deposition process

The six different interlayer concepts, each with a thickness of $\approx$500 nm, were deposited by magnetron sputter deposition (Discovery 18DC/RF, Denton Vacuum Company). The deposition chamber was evacuated by a turbo molecular pump using a liquid nitrogen trap to a base pressure of $\approx$2.7$\cdot$10^{-7} Pa. Argon with a gas flow of 25 sccm was used for sputtering resulting in a chamber pressure of $\approx$3 - 4$\cdot$10^{-3} Pa during the sputter deposition. The Cu sputter target (purity of 99.99%) operated in radio frequency (RF) mode was attached to cathode 1 while the W sputter target (purity of 99.95%) operated in direct current (DC) mode was connected to cathode 2. The distance between target and sample was fixed to $\approx$9 cm.

The planar samples were circularly positioned on the sample holder. For fiber coating, W fibers were fixed on a Cu frame and positioned perpendicular to the sample holder plate in the magnetron sputter deposition machine. Thereby, the distance of

the fibers of the upper part to the target is smaller then of the fibers of the lower part. This leads to an inhomogeneous longitudinal coating in the fiber direction during the deposition. The coating thickness varies up to 20 % of the thickness. For this work, the coating thickness gradient was neglected.

Before deposition, the planar samples and the fibers were etched by the argon plasma for 2 minutes (100 W, 570 V bias) to remove oxide layers and adsorbed impurities. Also, the sputter targets were pre-cleaned for 2 minutes (Cu at 250 W, $\approx$350 V and W at 150 W, $\approx$508 V).

Depending on the interface concept the power of the charged cathodes was controlled. Table 5.1 gives an overview of the applied deposition parameters for the respective interface concepts (see Table 2.1). Regarding the concept C and D, the Cu concentration is thereby increased in $\approx$25% steps from W to Cu by varying the power to the Cu and W electrodes every 9 minutes. For concept E the power of the Cu and W electrodes were increased and decreased, respectively, every minute resulting in a concentration change in $\approx$2% steps. Thus, the continuously graded interlayer consists of 50 layers with thicknesses of $\approx$10 nm each.

All depositions were performed without external heating and bias voltage. The substrate holder was rotating at 10 rpm to allow homogeneous deposition and etching. The sample temperature was measured during film deposition by thermocouples close to the substrate holder.

The film thickness was measured by a profilometer (alpha-step 200, Tencor) on references samples.

Table 5.1: *Deposition parameter of the different interface concepts. The thickness of all PVD films is $\approx$500 nm. A chamber pressure of $\approx$3 - $4 \cdot 10^{-3}$ Pa was measured during the sputter deposition. The nomenclature of interface concepts can be found in Table2.1.*

interface concepts	Deposition power on Cu target [W]	Voltage of Cu target [V]	Deposition power on W target [W]	Voltage of W target [V]	Deposition temperature	Total deposition time
B	100	380	-	-	$\approx$27°C	23 min
C and D	0	$\approx$0	155	$\approx$390	$\approx$56°C	45 min
	40	$\approx$140	200	$\approx$380		
	168	$\approx$300	268	$\approx$400		
	107	$\approx$230	47	$\approx$310		
	95	$\approx$205	0	$\approx$0		
E	0 - 88	0 - 190	137 - 0	340 - 0	$\approx$36°C	50 min

5.1.2 Microstructuring

The six different microstructuring concepts, presented in Table 2.1, were applied on the tungsten fibers. The realization of the different types of microstructuring is described below:

- Chemical etching was performed for 10 minutes in a Murakami solution consisting of 100 ml H_2O with 15 g NaOH mixed in 1:1 ratio to 100 ml H_2O with 15 g Kaliumferricyanid $K_3[Fe(CN)_6]$.

- Ion sputtering was performed by the magnetron sputter deposition device. Fibers fixed on a Cu frame were inserted into the deposition chamber which was pumped down to a base pressure of $\approx 5 \cdot 10^{-6}$ mbar. Argon plasma with a gas flow of 25 sccm was generated and a RF power of 50 W, with the resulting bias voltage of 294 V, was applied to accelerate the ions to the surface of the tungsten fibers. At a pressure of $\approx 1 \cdot 10^{-3}$ mbar, ion sputtering was performed for 1 h resulting in a mass loss of $1.77 \cdot 10^{-6}$ g/mm^2. The mass loss was evaluated by weighing a reference W substrate before and after the ion sputtering using a micro balance (MC21S from Sartorius).

- For the fiber twisting process, a novel method was developed. Tungsten is brittle at room temperature, but at temperatures between 200°C and 500°C, tungsten reaches the transition from brittle to ductile and is processable [79]. The principle of the twisting process is based on heating the fiber via resistive heating and simultaneously twisting the fibers clamped in a turning lathe. Similar fiber heating arrangements was performed in [121]. An external current source is used to drive the resistive heating current through the spindle at the tail stock and the turning lathe. The specific resistance $\rho(T)$ of the fiber increases with the temperature [122–124] and can be approximated by

$$\rho(T) = 5.65 \cdot 10^{-8}\Omega/m + \alpha \cdot \frac{T}{300\text{K}} \tag{5.1}$$

where α is the temperature coefficient and T is the temperature. The temperature of the electrical resistance $\tilde{R}$ and the resulting current I can be calculated with

$$\tilde{R}(T) = \frac{\rho}{A} \cdot l \tag{5.2}$$

and

$$I = \frac{U}{\tilde{R}} \tag{5.3}$$

where A is the cross section of the tungsten fiber, l is the fiber length and U is the voltage. In order to avoid surface oxidation of the fiber, the twisting process was performed in an inert gas chamber. Argon prevents the chemical reaction between the heated fiber and oxygen which begins at 400°C [79]. The inert gas flow rate was set to $1\,\mathrm{m^3/h}$ and was controlled by a gas flow controller (Flow meter PT 2700). The temperature is sensitive to differences in the environment such as gas circulation of argon and electrical losses at contacts. Therefore, a two-color pyrometer was used to obtain the temperature of the heated fiber experimentally. The deviation of the calculated temperature from the pyrometer measurements was approximately ±50°C. The estimated temperature variation along the wire in the longitudinal direction was 40°C - 80°C. A temperature of ≈470°C (1.3 A) was determined to be the optimal temperature for the twisting process of the $100\,\mathrm{\mu m}$ thin tungsten fiber.

The twisting angle α (presented in Figure 5.1) was controlled by the turning lathe and can be approximated by the following equations:

$$\alpha = arctan\frac{a}{l} \tag{5.4}$$

with

$$a = r \cdot \omega \tag{5.5}$$

and

$$\omega = 2\pi \cdot U_{rot} \cdot t \tag{5.6}$$

where a is the arc length, r the fiber radius, ω the total rotation angle, U_{rot} the number of rotation per minute, and t the twisting time, and l the fiber length. The maximum twisting angle was fixed to 30° since larger angles resulted in surface damage and a large reduction in tensile strength. The number of rotation per minute were fixed to $80\,\mathrm{r/min}$ for twisting to 20°±4° and $115\,\mathrm{r/min}$ for twisting to 30°±4°.

5.1.3   Sample geometries

5.1.3.1   Planar samples

Planar samples were mainly used to investigate the various interface concepts. Thereby, different planar substrate materials were deposited with the stepwise and the continuously graded transition (interface concepts C, D and E): quadratic Si wafer (polished,
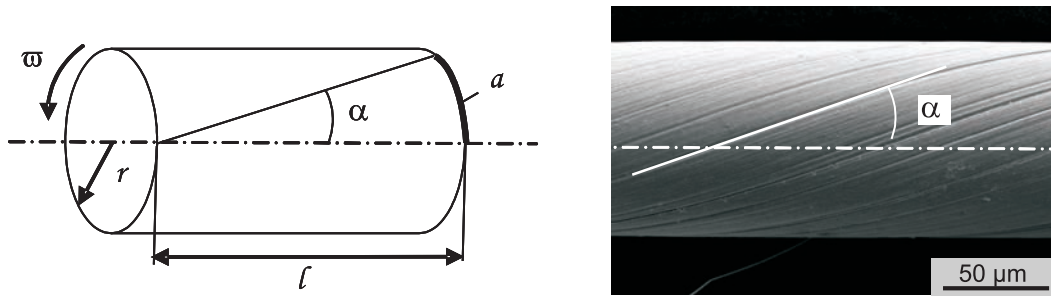
Figure 5.1: *Defined twisting angle on the W fiber, adjusted by the number of rotations of the turning lathe*

(100) orientation, a = 1 cm, ≈0.5 mm thickness, from CrysTec), quadratic pyrolytic graphite (polished, a = 1 cm, ≈1 mm thickness, from Union Carbide), circular W sheet (rolled, r = 0.5 cm, ≈0.3 mm thickness, from Plansee) and circular SiO_2 substrates (polished, r = 1 cm, ≈1 mm thickness, from GVB). All substrates were cleaned with isopropanol.

Planar samples for interdiffusion and segregation experiments

The W/Cu diffusion couples were made from high-purity Cu substrates (Goodfellow) deposited with 500 nm W layer by magnetron sputter deposition. For the segregation experiment interface concept C was deposited on a graphite substrate. This sample was tempered at 650°C for 60 minutes.

Planar samples for thermal stability tests

For thermal stability of graded interlayers, planar samples were coated with interface concept C and were transferred to a vacuum furnace (oven MOMO, base pressure ≈5·10^{-4} Pa, during heating ≈1·10^{-3} Pa) and annealed at 550°C, 650°C and 800°C for 60 minutes. The temperature were chosen according to the requirements which have to be fulfilled by the interface coatings (see chapter 2.1). The temperature was controlled by thermocouples installed near the sample.

5.1.3.2 Fibers

W fibers (drawn, OSRAM) with a diameter of 100 µm were used to produce single matrix-coated fibers, for microstructuring and for long-fiber reinforcement of the Cu matrix. All initial fibers were cleaned ultrasonically in aceton and isopropanol to remove possible fabrication residues.

Matrix-coated single fibers for pull-out measurements

For the mechanical characterization of the interface between fiber and matrix, pull-out tests (see chapter 5.4.2) on matrix-coated single tungsten fibers were performed. Initial or pre-treated fibers (comprising unstructured fibers with the interface coating concepts B, C, E and microstructured fiber plus interface concept B) were electroplated for 22 h at room temperature in a $CuSO_4$ bath to obtain an adequate matrix thickness (≈ 1 mm) to pull against. Here, 1/3 of the fiber length was inserted into the bath.

Wang et al. [125] demonstrate that adherent Cu films with apparent dendritic growth can be directly electroplated on a W surface from Cu^{2+} in sulfuric baths. They showed that the pH-value of the bath effects the adhesion of the film: PH values > 1 results in poorer adhesion of Cu films. Additionally, it was shown that the average Cu nucleation size is controlled by deposition potential. In this work a $CuSO_4$ bath with constant pH-value of 1.2 was used. For a homogeneous coating, 0.8 V (1.89 A) was applied.

After deposition, the fibers were heat-treated at 550°C for 1 h with a slow heating rate of 20°C/h to avoid the formation of pores by outgassing of hydrogen and oxygen present in the electroplated layer [84,85]. The length of the electroplated copper matrix was varied by cutting to obtain embedded fibers with different lengths between 0.5 mm and 3 mm.

5.1.3.3   MMC

The synthesis of the multi-fiber MMCs was performed similar to the matrix-coated single fiber. The thickness of the electroplated Cu layer of the coated fibers defines the fiber volume content in the composite: to obtain a fiber volume fraction of ≈ 20 %, the pre-coated fibers were electroplated with a ≈ 60 µm thick Cu layer within 73 min instead of 22 h as for the single coated fiber synthesis. After the deposition, the fibers were slowly outgassed as with the single fibers (500°C; 20°C/h; 1h). In the last step, the coated and heat-treated single fibers (≈ 100) were packed in a Cu capsule (inner diameter = 3.5 mm), sealed by vacuum welding and consolidated by hot-isostatic pressing at 650°C with a pressure of 100 MPa for 30 min. The HIP process was kindly performed by EADS, Corporate Research Center Germany SC/IRT/LG-MT, Munich in Germany. The resulting MMC shows a homogeneous fiber distribution.

Thermal cycling experiments

For thermal cycling experiments, thin discs of 1 mm were cut from the MMC, polished on both sides and characterized by SEM before and after thermal cycling.

Oxygen content measurement

The discs, as prepared for the thermal cycling test, were used for oxygen (O) content measurements within the MMC by NRA.

Residual stresses during thermal cycling

Different MMCs (see chapter 5.4.4) were machined to a diameter of 3.5 mm and MMC length of 16 mm for adequate residual stress measurements.

5.1.4 Monoblock mock-up

The final experiment of this thesis is the testing of two optimized water-cooled monoblock mock-ups under high heat flux. All achieved results (see chapter 6) are unified in the synthesis of these compounds which were constructed the same way. Interface concept E and microstructuring concept II were chosen to be applied on the fibers used for the MMC reinforcement of the interface between the PFM and the cooling channel in the monoblock mock-ups.

The geometry of the monoblock mock-ups was chosen in a way such that the results of the high heat flux tests can be compared to those of the ITER divertor mock-ups and to the investigated mock-ups within the Extremat project. The novel W monoblock mock-up geometry can be seen in Figure 5.3. The standard design was slightly modified such that the W_f/Cu MMC reinforces the cooling tube. Based on the simulation results of You [126], the orientation of the W fiber reinforcement is chosen to achieve an axial and tangential reinforcement.

The W tiles were obtained from bulk rolled material from Plansee. The tiles were machined in order to orient the rolling directions, which is the grain orientation, along the high heat flux direction which is perpendicular to the heated surface. The internal diameter of the W tiles were machined by wire-electro discharge and subsequently polished resulting in a low roughness of $R_a \approx 0.2$ nm. Holes (d = 0.1 mm) were drilled 2.5 mm under the loaded surface of each W tile to install thermocouples for temperature measurements.

The following steps were performed to synthesize the monoblock mock-up:

- The first steps were the fiber microstructuring by concept II and coating by interface concept E (see chapter 5.1.1 and 5.1.2).

- The PVD coated fibers were deposited with a $\approx$60 µm thick Cu electroplated layer plus heat treated (see also chapter 5.1.3.3).

- Subsequently, the $\approx$100 fibers were 45° aligned on a 0.02 mm thick Cu foil (99.9%) cut in trapezium shape (see Figure 5.2). In total four layers were implemented in such a way that two layers were orientated to 45° and two layers to -45° to achieve a homogeneous 45°/-45°/45°/-45°/ reinforcement.

- The foils were wrapped around a 17 mm thick CuCr1Zr (0.5-1.2 Cr, 0.03-0.3 Zr, rest Cu [83]) rod resulting in a gap-free ±45° orientated wrapped fiber reinforcement.
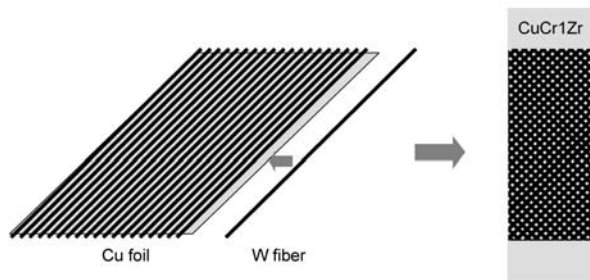
Figure 5.2: *±45° fiber alignment around the CuCr1Zr cooling tube*

- The wrapped CuCr1Zr rod was encased by a Cu capsule, sealed by vacuum welding and consolidated by hot-isostatic pressing as performed in the MMC synthesis (see chapter 5.1.3.3).

- The consolidated fiber-reinforced compound was post machined to obtain a cylindrical clearance fit between the MMC reinforced CuCr1Zr rod and the W tiles.

- The 12 mm thick hole was bored centrally through the CuCr1Zr rod to functionalize it as a cooling tube.

- Among the available brazing alloy, GEMCO alloy (Cu12Ge0.25Ni alloy from Wesgometals) has been selected as the most suitable brazing material for the

joining of the cooling tube into W. Three thin foils of GEMCO alloy were wrapped around the reinforced cooling tube.

- The four W tiles were beaded over the reinforced cooling tube plus brazing foil with a distance of 0.5 mm in between and heated at ≈970°C in a vacuum furnace. The properties of CuCr1Zr were recovered by suitable brazing thermal cycle (solubilization, fast cooling, aging: 480 - 550°C for 2-4 hours [9]). The brazing process was performed by ANSALDO, Materials and Technological Processes Laboratory, Genova in Italy [127].

- To finalize the monoblock mock-up as a high heat flux testing device, the CuCr1Zr tube were clamped to the water cooling supply using Swagelok plugs. Thermocouples with a diameter of 0.1 mm were glued 2.5 mm into the bore holes of each W tile for temperature measurements.
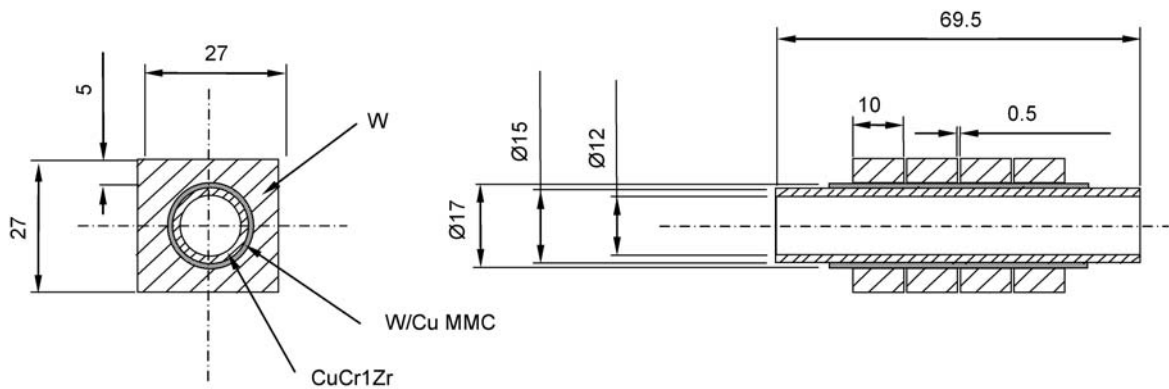
Figure 5.3: *Geometry of novel W monoblock mock-up based on the ITER reference geometry for standard W monoblock compounds*

5.2 Fiber characterization

The initial fiber and the nano- and microstructured fibers were characterized in detail.

5.2.1 Fiber surface morphology characterization (SEM, AFM)

Surface morphology characterization of the tungsten fibers was performed at the nanometer scale using atomic force microscopy (AFM) (chapter 4.2) under ambient conditions using Rasterscope 400 by DME. For the initial fiber and for each microstructuring

concepts, scans were made of 2 µm x 2 µm and 4 µm x 4 µm areas with 512 x 512 data points, with a scanning speed of 2 µm/s and 4 µm/s, respectively. All images were obtained in the contact mode using silicon tips by Nanoworld Pointprobe CONTR with approximate tip radius smaller than 10 nm. A constant force of 1 nN was chosen. Each fiber was measured three times at different locations on the surface. The raw data was processed with the open-source software Gwyddion [128].

The microstructure of the initial and modified tungsten fibers was examined on micrometer scale with XL 30 ESEM Scanning Electron Microscope (SEM) by FEI.

After the pull-out measurements (see chapter 5.4.2), SEM images were acquired to locate the point of failure.

5.2.2   Fiber roughness analysis (AFM)

The roughness analysis is based on the AFM data. The AFM data is collected as line scans along the x axis that are connected together to form the two-dimensional image. The scanning speed in the x direction is considerably higher than the scanning speed in the y direction. Therefore, the statistical properties like roughness values of AFM data are collected along the x profiles as these are less affected by low frequency noise and thermal drift of the cantilever [128]. The following standardized one-dimensional roughness parameters were determined for the 4 µm x 4 µm scanned area: the root-mean-square roughness (RMS), the skewness and the kurtosis parameters.

The RMS parameter describes the roughness statistically by the standard deviation of the distribution of surface heights measured within the evaluation length and from the mean line:

$$RMS = \sqrt{\frac{1}{N}\sum_{i=1}^{N}r_i^2} \tag{5.7}$$

where $r_i = z_i - \bar{z}$. The mean line was so defined that the sum of the square of the deviations of the profile height from it was zero [129].

The skewness parameter is used to distinguish between two profiles having the same RMS values but different symmetries about the RMS mean line. It describes the shape of the height distribution function and is defined as follows

$$R_{sk} = \frac{1}{N \cdot RMS^3}\left(\sum_{i=1}^{N}r_i^3\right) \tag{5.8}$$

Positive skewness indicates valleys filled in or high peaks so that the bulk of the sample

is below the mean line, while negative skewness indicates reduced peaks and/or deep scratches so that the bulk of the sample is above the mean line [129, 130].

The kurtosis of a profile is used to distinguish between two profiles having the same RMS values but different periodicity. The shape of the distribution density of the profile can be platykurtic ($R_{ku} \prec 0$) which is equivalent to few high peaks and low valleys, or leptokurtic, ($R_{ku} \succ 0$) which is equivalent to many high peaks and low valleys. The kurtosis is defined as

$$R_{ku} = \frac{1}{N \cdot RMS^4} \left(\sum_{i=1}^{N} r_i^4 \right) - 3 \tag{5.9}$$

For each fiber type the RMS, skewness and kurtosis values of three different spots were determined. The average values and their standard errors were calculated, respectively, and compared in chapter 6.2.2.

5.2.3 Fiber surface area

The mechanical interlocking depends on the surface size of the contact areas. For the six different microstructuring concepts the surface area was analyzed based on AFM data. The surface area is estimated by the triangulation method proposed in Gwyddion [128] and based on Douketis [131].

The values were determined from three different spots on each modified fiber for the 2 µm x 2 µm and 4 µm x 4 µm scanned area. The ratios value of the real surface area to the projected surface area of the 2 µm x 2 µm and 4 µm x 4 µm scanned area were used to obtain an average value and its standard error (chapter 6.2.2).

5.3 Coating characterization

The five different interlayers between W and Cu are based on three different interface coatings. The morphology of the coatings were characterized. The stepwise and continuously graded W/Cu coating were characterized in detail. Due to the clear layer structure of the stepwise graded coating, it was used for segregation experiments, thermal stability investigations and thereby resulting characterization.

5.3.1 Coating morphology (SEM, TEM, AFM)

Two scanning electron microscopes (XL 30 ESEM from FEI operated at 20 kV and Helios Nanolab 600 from FEI operated at 10 kV, both equipped with EDX) were used

to analyze the surface morphology and the cross-sections of the coated planar samples and fibers.

Preparation of cross-sections of the interface concept coated W substrate and fiber was performed by FIB (chapter 4.1). Subsequently, some samples were analyzed by TEM done by M. Rasinski at IPP and at the Technical University of Warsaw. Two transmission electron microscopes (TEM 1200 from JEOL operated at 120 kV and Philips EM 430 operated at 300 kV) were applied for the microstructural characterization of the samples.

5.3.2   Coating composition (RBS)

To understand the reactions between W and Cu at elevated temperatures, the type of interface between the W fiber and the Cu matrix must be identified. The binary phase diagram states that no chemical alloying of Cu and W occurs independent of temperature. This was revised in interdiffusion experiments (chapter 6.1.1) where W/Cu diffusion couples were tempered at 500°C, 650°C, 800°C and 900°C. The diffusion couples were made as described in chapter 5.1. After tempering, the resulting Cu and W depth profiles were measured using Rutherford Backscattering Spectrometry (RBS) (see also chapter 4.4).

Due to the insolubility of Cu and W, segregation experiments (chapter 6.1.1) are performed to investigate the stability of the graded transition layers, interface concept C, D and E, at elevated temperatures. For the segregation experiment interface concept C was deposited on a W substrate. This sample was tempered at 650°C for 60 minutes and the resulting Cu and W depth profiles were measured using RBS.

For both experiments the RBS measurements were performed using a 6 MeV ^{4}He^{2+} ion beam and a scattering angle of 165°. The spot size was about 1x1 mm^2 and a charge of 20-30 µC was accumulated for a spectrum. The Cu and W depth profiles were extracted from the measured spectra using the SIMNRA program [132]. The film composition was determined in at - %.

5.3.3   Coating phase, texture and stress analysis (XRD)

The crystallographic phase analysis, stress state and texture of interface concept C were determined on planar SiO$_2$ samples by XRD (XRD 3003 PTS diffractometer, Seifert). The diffractometer was operated with Cu K$_\alpha$ radiation (0.154 nm). A parabolic multilayer mirror was used on the primary side to achieve a parallel beam and K$_\beta$ suppression. On the secondary side, parallel metal plates, perpendicular to the scattering

plane, were installed to restrict the divergences to 0.4°.

The phase analysis, stress and texture analysis by XRD were performed at RT and were measured after annealing to 550°C, 650° and 800°C.

The phase spectra were acquired in a $\theta/2\theta$-scan.

For texture analysis the diffraction angles were fixed so that the specific lattice spacing of the Cu {111} and W {110} planes were chosen. The pole figures after heating at different temperatures were compared and can be found in chapter 6.1.4.3.

The intrinsic stresses were analyzed by XRD using the $\sin^2\psi$ method (chapter 4.3). Polycrystalline films deposited on amorphous substrates exhibit isotropic biaxial stress within the film plane [46]. For the stepwise graded coating a biaxial residual stress state of rotational symmetry ($\sigma_{13} = \sigma_{23} = \sigma_{33} = 0$ and $\sigma_{11} = \sigma_{22}$) independent of the thickness was assumed for simplification of the complex stress state of the inhomogeneous and textured coating. The stress was measured for $\phi= 0°$ - 90° and $\psi= -70°$ - 70°. The average stress values with the standard error were determined and compared (see chapter 6.1.4.4). Additionally, a biaxial residual stress state ($\sigma_{13} = \sigma_{23} = \sigma_{33} = 0$) independent of the thickness was assumed for comparison. The thermal stress introduced during the deposition process was calculated using the thermal stress equation (see chapter 3.1.3) and was subtracted from all XRD measured stress values to obtain the intrinsic stresses. The elastic mechanical properties (E_f, ν_f) of the stepwise graded coating were determined by using the rule of mixture and assuming bulk material properties of Cu and W.

5.4 Mechanical characterization

Five different experimental tests were realized in this work to achieve a closer understanding of the involved materials and their interfaces.

5.4.1 Fiber tensile strength analysis

The aim of the experimental fiber tensile test was to determine mechanical properties of initial and microstructured tungsten fibers. From the surface modifications, however, possible stress peaks due to the notching effect can be introduced into the tungsten fiber surface reducing the ultimate tensile strength (UTS). The UTS is an important criteria to validate the application of the fibers in the Cu compound.

The experimental tests were carried out on the universal test machine from Tira Test 2820 (TIRA GmbH) under ambient conditions. Some fibers allow performing the tensile test measurement using a Laser-Speckle Extensometer LSE-4000 DE to determine the

length change and consequently the Young's modulus. The others exhibit a irregular surface so that the laser signal cannot be evaluated. Therefore, the ultimate tensile strength (UTS) for the initial and six different microstructured fibers were determined and compared. For each fiber type, the UTS of ≈15 fibers were determined and an average value and its standard error were calculated. The measuring error of the tensile machine was neglected.

The fiber specimens were glued to a steel strip, at both ends, using two-component epoxy resin glue. Subsequently, the steel strips were fixed in the clamps. The influence of the steel strip on the results is assumed to be negligible, because the deformation is small compared to that of the tungsten. The specimen was attached to the tensile tester with the use of locking pins. To ensure that the sample was loaded uniaxially, the x-y displacement table was utilized to determine the straight position.

The raw data was captured and analyzed. The constitutive equations, after DIN EN 10 002 [133], were applied to evaluated the UTS for the specimen. The comparison of the obtained UTS values is given in the results chapter 6.

5.4.2   Pull-out test on matrix-coated single fibers

Pull-out tests on coated and/or microstructured tungsten single fibers were performed to characterize the interface between fiber and electroplated Cu matrix. The fiber pull-out test can be analyzed like the fiber push-out test but with some modification including the change of sign of the interfacial friction stress.

The universal test machine was used to pull the matrix-coated single fibers (chapter 5.1.3.2) out of the matrix. During the pull-out, the displacement and the resulting load were acquired continuously. From this raw data the P_d value, the first local maximum peak of the load-displacement curve indicating the onset of debonding, was determined. And the P_{fr} value, the load required to overcome the pull-out friction, manifesting in oscillation of the curve, was determined. The values P_d and P_{fr} as function of the embedded length L serve as data which will be fitted with formulas (see equations 5.10 and 5.11) modified from [134] to obtain the two characteristic interface properties: the interfacial shear strength τ_d and interfacial friction stress τ_{fr}. The interfacial shear strength τ_d is defined as the maximum shear stress encountered at the interface of fiber and matrix just prior to the onset of debonding [135]. The interfacial friction stress τ_{fr} causes the reactive force during fiber slip in the opposite direction of the movement [135].

$$P_d = \frac{\tau_d \cdot 2 \cdot \pi \cdot R}{\alpha} \cdot tanh(\alpha \cdot L) \tag{5.10}$$

$$P_{fr} = \frac{\pi \cdot R^2 \cdot \sigma_0}{k} \cdot \left[exp(-\frac{2 \cdot \mu \cdot k \cdot L}{R}) - 1 \right] \tag{5.11}$$

$$\tau_{fr} = \mu \cdot \sigma_0 \tag{5.12}$$

with

$$k = \frac{\nu_f \cdot E_m}{E_f \cdot (1 + \nu_m)} \tag{5.13}$$

with fiber radius R, embedded matrix length L, radial residual stress σ_0, friction coefficient μ, Young's moduli of fiber and matrix E_f, E_m and Poisson's ratio of fiber and matrix ν_f, ν_m.

For each interface and microstructuring concept $\approx$18 fibers were pulled out. The characteristic interface properties τ_d and τ_{fr} of the interface and microstructuring concepts with their fitting errors are compared in chapter 6.1.3 and 6.2.5.

5.4.3 Thermal cycling of multi-fiber MMC

The thermal expansion mismatch between the reinforcements and the matrix metal causes high residual stresses already present after cooling during the synthesis. Thus, debonding at the interfaces and plastic deformation of the matrix were expected. To investigate the influence of the CTE mismatch of W fiber and Cu matrix on the microstructure, thermal cycling tests were performed on MMCs with the interface concept B and C. The synthesis of the multi-fiber MMCs and MMC disc preparation for thermal stability testing are described in chapter 5.1. For thermal stability testing the discs were, perpendicular to the base plate, fixed in the vacuum furnace (oven MOMO, base pressure $\approx$5$\cdot$10^{-4} Pa, during heating $\approx$1$\cdot$10^{-3} Pa). The discs, characterized by SEM before and after thermal cycling, were cycled 120 times between 350°C - 550°C with a rate of $\pm$10 K/min.

5.4.4 In-situ residual stresses of MMCs by neutron diffraction

Quantitative validation of the multi-fiber MMCs were performed by investigation of the residual stress via neutron diffraction. Neutron diffraction provides the opportunity of stress measurements in penetration depth of mm scale simultaneously during thermal cycling.

Residual stresses for two optimized MMCs were measured to validate the effects of the different implemented interface concepts:

1. MMC 1: Initial W fibers (microstructuring concept 0) combined with interface concept B

2. MMC 2: Microstructuring concept 0 combined with interface concept E but without 800°C heat treatment

Thereby, MMC 1 serves as the reference sample and MMC 2 should demonstrate the CTE mismatch buffering by the graded transition quantitatively.

The strain measurements were carried out on the E3 instrument at HMI Berlin [136]. A Cu (220) monochromator was used to produce monochromatic neutrons and a wave length of 1.486 Å [137]. A 2D ^{3}He system with a dimension of 300 mm x 300 mm with 256 pixels in each direction was used as the detector. The distance between the sample and the detector was fixed to ≈130 cm. The detector was positioned at 86.50°. The angle range of the detector in the vertical and horizontal directions was 13.14°. For the primary side, an aperture of 5 x 5 mm^2 was chosen while on the secondary side a vertical slot aperture of 2 mm width was installed.

The sample was positioned 45° to the incoming beam to measure the longitudinal stress and rotated 90° to measure the transverse stress. The gauge volume was chosen as large as possible to reduce exposure times down to 5 min and reduce the influence of macro stress. The samples were mounted on a sample holder with weak thermal contact and were heated with a ceramic encased wire. The temperature was measured by a thermocouple fixed directly on the surface of the sample.

One pure Cu matrix sample with same dimensions like the MMCs was measured under the same conditions to distinguish between macro and micro stresses, thus, allowing differences in the micro stress during thermal cycling to be analyzed.

Similar to their operation temperature, the samples were cycled two times between RT - 550°C. Strain measurements were made at temperature steps of RT, 200°C, 400°C and 550°C, respectively, with a dwell time of 5 min. The measurements were performed in the frame of the Extremat project [92] by Michael Schöbel from TU Vienna Material Science and Technology department.

Stress calculation

The symmetry of the cylindrical samples reduces the problem to a 2-axial stress system. The longitudinal strain was measured independent of the transverse contribution. The transverse stress contribution in the matrix is a combination of radial and tangential stresses at the fiber-matrix interfaces. The neutron strain measurements indicate an average lattice strain over the gauge volume. Thus, it is not possible to distinguish

between radial and tangential stresses at the fiber/matrix interfaces. The following equations [138], based on Hooke's law, were used to determine the stresses of the matrix in longitudinal and transverse directions and of the fiber in longitudinal direction:

$$\sigma_l = (\varepsilon_l - \varepsilon_l \nu_{matrix} + 2\varepsilon_t \nu_{matrix}) \frac{E_{matrix}}{(1 + \nu_{matrix})(1 - 2\nu_{matrix})} \tag{5.14}$$

$$\sigma_t = (\varepsilon_t + \nu_{matrix}\varepsilon_l) \frac{E_{matrix}}{(1 + \nu_{matrix})(1 - 2\nu_{matrix})} \tag{5.15}$$

$$\sigma_{fiber} = \varepsilon(1 - \nu_{fiber}) \frac{E_{fiber}}{(1 + \nu_{fiber})(1 - 2\nu_{fiber})} \tag{5.16}$$

with stress σ, strain ε, Young's modulus E and Poisson ratio ν. For the fiber stress, an uniaxial strain state was assumed as the radial contribution could not be evaluated because of strong fiber texture.

5.4.5 High heat flux experiments of optimized monoblock mock-ups

High heat flux tests were carried out on two optimized active water-cooled monoblock mock-ups in the neutral beam facility GLADIS at IPP Garching. The goal was to investigate the thermal performance of the whole monoblock mock-up focusing on the implemented W_f/Cu MMC at the interface between W PFM and CuCr1Zr cooling tube.

Screening tests with increasing power density were applied to determine the ultimate loading conditions and pre-testing the performance of the monoblock mock-ups under heat load. The surface was exposed to an heat flux of 0.2, 0.5, 1, 1.5, 2, 3, 4.4 , 5.2, 6 MW/m^2 for 30 seconds, respectively, and 7, 8 and 10.5 MW/m^2 for 20 seconds, respectively, to achieve a steady state temperature. Additionally, the second monoblock mock-up was cyclically loaded with a heat flux of 10.5 MW/m^2. 25 cycles were performed to investigate the fatigue behavior of the optimized monoblock mock-up. Every minute the mock-up was loaded for 20 seconds.

Two Cu water pipes were clamped onto the water channel of the monoblock mock-ups to provide pressurized cooling water. Water, with a temperature of 10°C, was pumped circularly through the cooling channel with a static pressure of 10 bar. The water flow was 12 m/sec.

The heat loaded area was fixed to the beam exposed surface of the four W tiles by two scrapers. The beam offers a homogeneous beam intensity distribution. The

surface temperature of the exposed mock-ups was determined by an infrared camera ($\lambda \approx$ 10 µm) taking frames during each pulse and, quantitatively, by a one- and a two-color pyrometer (temperature ranges: one-color 650°C - 2200°C and two-color 700°C - 1700°C). For the one-color pyrometer (λ = 0.85 - 1.1 µm) an emissivity of 0.4 was assumed for the W surface. A CCD video camera imaged the component during each pulse. The bulk temperatures of each W tile were measured by thermocouples (temperature range limit 1800°C), which were placed 2.5 mm under the beam faced surface.

The Finite Element Model

A 2D Finite Element Analysis (FEA) was performed to pre-estimate the expected transient temperature at the surface and within the monoblock mock-up during high heat flux test. In the pre-processing step a mathematical model was generated, i.e., the material properties depending on the temperature, boundary conditions and applied heat flux loads were expressed mathematically. The surface was exposed to a heat flux of 1, 2.5 , 5, 10, 15 and 20 MW/m^2 for 10 seconds, respectively. The cross-section geometry of the W_f/Cu monoblock (see Figure 5.3) was then discretized using a collection of finite elements joined by shared nodes (mesh). The axial symmetry of the cross section of the monoblock was utilized to reduce the computational effort. In the simulation step the temperature in each finite element was determined depending on the applied heat flux on the W tile surface and was stored as output files ready for post processing. The output files were graphically displayed for understanding and interpretation the results.

The commercially available software FEM System ANSYS 5.3 was used for the FEA. A self-developed algorithm by Greuner [139] was implemented as input for the transient and steady-state FEA to consider complex heat transfer phenomenon occurring in the cooling tubes. The thermodynamics and constitutive equation, which are well accepted in the fusion community [139–141], are briefly summarized in the following.

The monoblock mock-ups cooling channel is supplied by pressurized cooling water (T_{water} = 20°C; p_{static} = 10 bar) with a water velocity of v_{water} = 12 m/s resulting in a high turbulent flow (Reynolds number (Re) = 144000 > 2300). Depending on the wall temperature, different heat transfer regimes occur in a uniformly heated tube (see Figure 5.4).
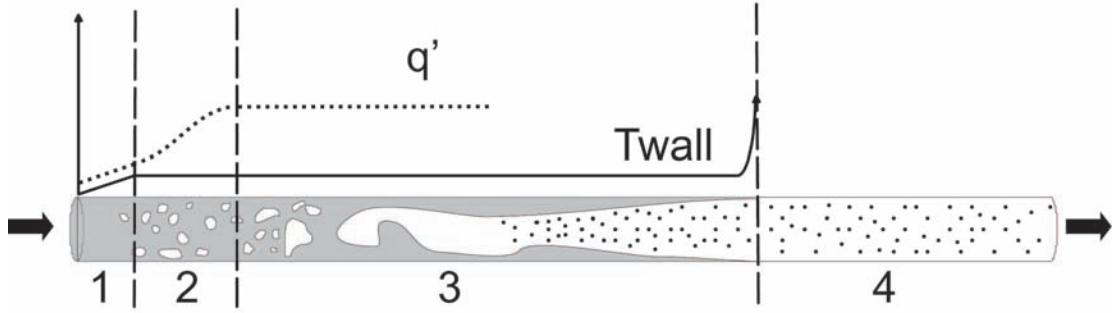
Figure 5.4: *Heat transfer regimes in a uniform heated tube:*
1) Single phase regime with forced convection
2) Transition region from forced convection to nucleate boiling
3) Sub-cooled boiling
4) Critical heat flux

- In the *single phase regime* (T < 180°C) the heat transfer is characterized by forced convection. For the turbulent flow in tubes, the heat exchange $\dot{q}$ is described by

$$\dot{q}_{con} = \alpha(T_{wall} - T_{water}) \tag{5.17}$$

with heat exchange coefficient α

$$\alpha = \frac{\lambda}{d} \cdot Nu \tag{5.18}$$

and thermal conductivity λ, internal tube diameter d and the Nusselt number Nu. The Gnielinski equation [142] is an explicit function for calculating Nu used for the heat transfer equation 5.18. It is described by

$$Nu_0 = \frac{\frac{\xi}{8}(Re - 1000)Pr}{1 + 12.7\sqrt{\xi/8}(Pr^{\frac{2}{3}} - 1)} \left[1 + \left(\frac{d_i}{l} \right)^{\frac{2}{3}} \right] \tag{5.19}$$

with the friction factor ξ

$$\xi = (1.82 \cdot log_{10}Re - 1.64)^{-2} \tag{5.20}$$

and Prandtl number

$$Pr\,(20°C) = \frac{\nu_{water}}{\alpha} = 6.94 \tag{5.21}$$

- At higher temperature (T > 180°C) the forced convection transitions to the beginning of *partial sub-cooled boiling,* which can be mathematically described

by Bergles and Rohsenow and by Thom [143]. During sub-cooled boiling, steam
bubbles are formed within the liquid at the wall if the wall temperature rises
above the saturation temperature, while the bulk of the liquid is subcooled. The
bubbles grow until they reach a critical size, at which point they separate from the
wall and are carried into the main fluid stream. There the bubbles collapse due to
the lower temperature of bulk fluid compared to the wall temperature. The heat
transfer process away from the walls is very efficient and can be calculated by
the quadratic sum of convection and sub cooled boiling by Bergles and Roshenow
(see Figure 5.5):

$$\dot{q} = (\dot{q}_{con}^2 + \dot{q}_{boil}^2)^{0.5} \tag{5.22}$$

with

$$\dot{q}_{boil} = \frac{(T_{wall} - T_{saturation})^2}{22.65 \cdot e^{\frac{-p}{87}}} \tag{5.23}$$

with water pressure p and saturation temperature of water $T_{saturation}$. The end of
the partial sub-cooled boiling (point A in Figure 5.5) is described by Engelberg-
Forster and Grief [143].

$$\dot{q}_A = 1.4 \cdot \dot{q}_B \tag{5.24}$$
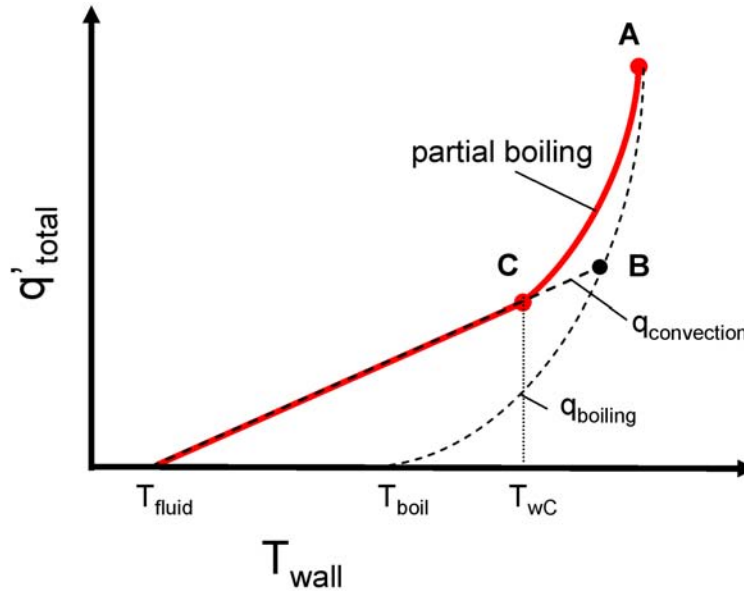
Figure 5.5: *Heat transfer of convection and partial subcooled boiling*

- The last heat transfer regime is the *critical heat flux regime*, where the wall
temperature increases dramatically due to the isolation effect of the bubbles.
This regime can be described by Tong [144, 145].

The main advantage of FEA is that the heat performance of the monoblock mock-up can be predicted without the considerable costs associated with laboratory experiments. However, to performe the simulation certain simplifying assumptions were made. Thus, the simulation is an approximation to describe temperature evolution within the cross section of the W_f/Cu monoblock and should be considered complementary to the experimental high heat flux tests.

Chapter 6

Results of interface optimization

6.1 Interface concepts

6.1.1 Interface reaction between W and Cu

The interface specification of the W/Cu system is an important basis for the optimization of their interface. Interdiffusion experiments with W/Cu diffusion couples were performed to verify that no chemical alloying of Cu and W occurs independent of temperature.

The RBS profiles of W and Cu after tempering the W/Cu diffusion couples at 500°C, 650°C, 800°C and 900°C are shown in Figure 6.1. The curves show the W and Cu peak. By investigating the left edge of the W peak a slight shift of the curves at different temperatures is observed. This results from the thickness variation of the measured samples caused by the inhomogeneous magnetron sputter deposition process of the Cu substrates. As there is no change in the slopes of the different curves, an interdiffusion between W and Cu can be ruled out.

6.1.2 Nanostructure of different interface concepts

Nanoscopic interfaces were tailored by depositing different interlayers on W fiber to achieve a form closure plus adhesive bond to enhance the adhesion between W fiber and Cu matrix and to buffer their thermal mismatch.

Figure 6.2 a) shows exemplarily the top view of the nanostructure of one interface concept (interface concept C, the stepwise graded W/Cu$_{PVD}$ interlayer) after the magnetron deposition process on top of the initial W fiber. Cross-sections were prepared by FIB and imaged by high resolution SEM. The nanostructure of the different concepts on initial rough W fibers (see also morphology characterization of the initial W
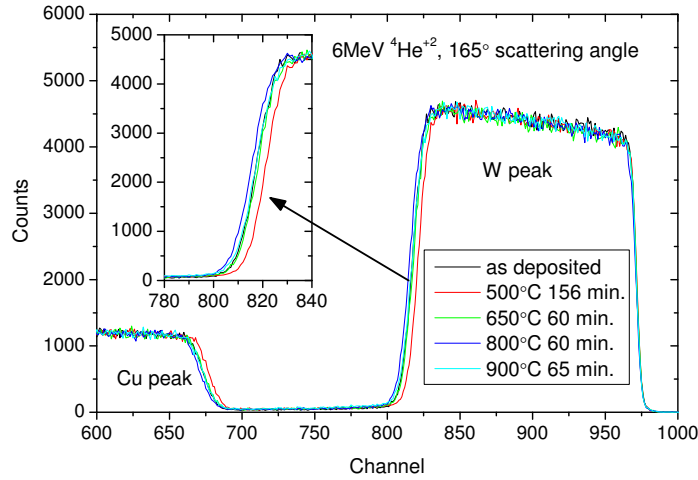
Figure 6.1: *RBS spectra of W/Cu diffusion couple measured at room temperature, 500°C, 650°C, 800°C and 900°C*

fiber in chapter 6.2.1) was characterized by the fine nanostructure of the thin PVD coating filling the gaps of the grooves of the W fiber. In turn, the nanostructure was characterized by the shadowing effects of the fine grooves of the W fiber. The resulting pore formation within the coating can be seen in the cross-section in Figure 6.2 b). After the subsequent electroplating process the surface exhibited a smoother surface structure (Figure 6.2 c)). The synthesized MMC showed a homogeneous fiber distribution (Figure 6.2 d)) with no pores in the different interlayers. Due to the influence of the fiber roughness leading to uneven interlayer deposition it was decided that the nanostructure of the different interface concepts in particular of the stepwise graded transition on planar samples should be analyzed.

Figure 6.3 presents the cross-section of interface concept C on a planar substrate and clearly shows the stepwise change of the nanostructure, in particular the grain size, by varying the W and Cu composition within the graded transition. A detailed nanostructure investigation can be found in chapter 6.1.4. The EDX maps indicate the changing concentration of W and Cu. As expected, the W concentration increases with decreasing Cu concentration.

Figure 6.4 presents the cross-section of interface concept E (continuously graded W/Cu$_{PVD}$ interlayer) without 800°C heat treatment. The changing of the nanostructure by continuously varying the W and Cu composition within the graded transition cannot be seen as clearly as at the interface concept C. The EDX maps indicate the continuously changing concentration of W and Cu. As the continuously graded transi-
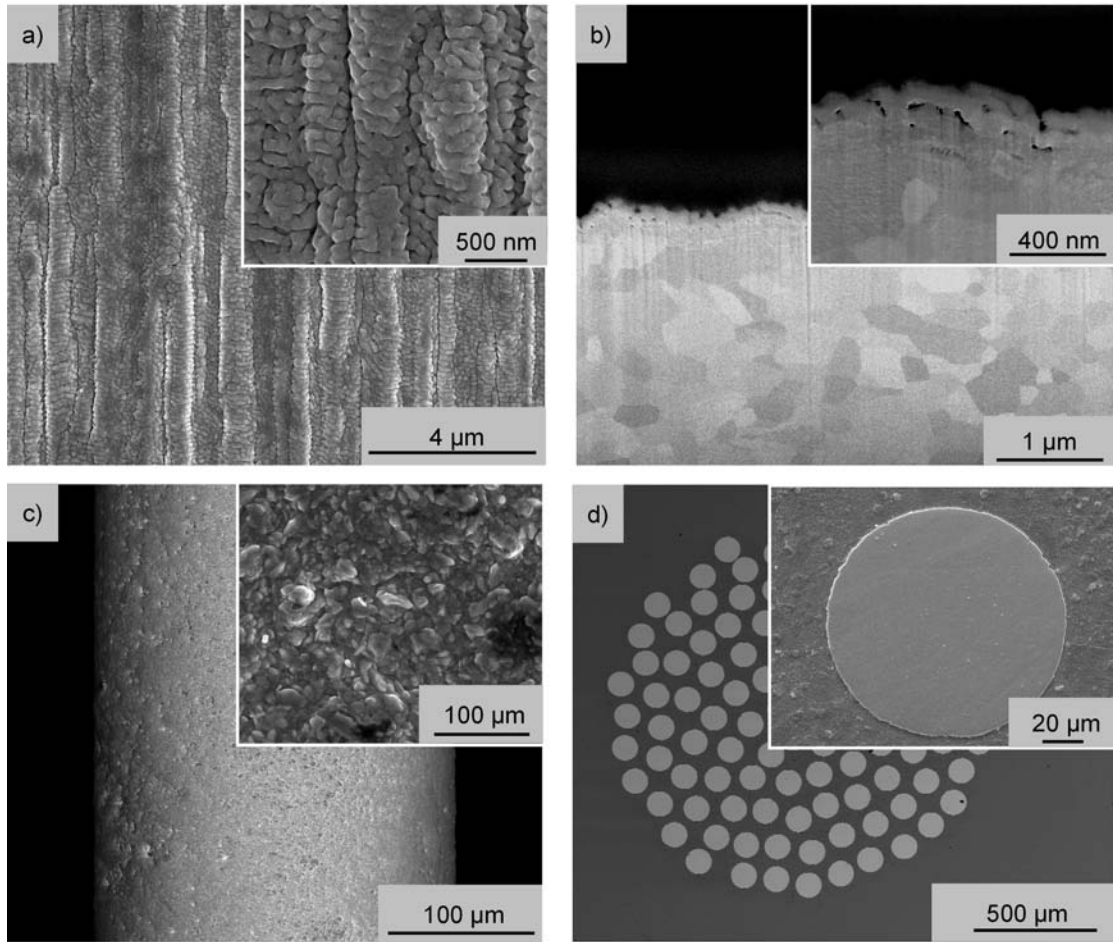
Figure 6.2: *a) Top view and b) cross-section of W fiber with the deposited stepwise graded W/Cu$_{PVD}$ interlayer (interface concept C)*
c) W fiber with interface concept C encased in ≈60 µm electroplating Cu coating
d) Consolidated W fiber-reinforced Cu MMC

tion shows a smooth transition from W to Cu with no significant characteristics in the nanostructure, it was decided to use the stepwise graded transition for further investigations like thermal stability tests. The thermal stability of the interface coating D and E is assumed to be similar due to the analogy of interface concepts.

6.1.3 Interfacial adhesion

In preliminary studies, push-out measurements were tested to investigate the interfacial adhesion. Due to the brittleness of W, the fibers split by trying to push them out of the matrix by an identor. This fact makes this measurement useless for W$_f$/Cu systems.

Therefore, for the mechanical characterization of the interface between the fiber and matrix, pull-out tests on matrix-coated single tungsten fibers were performed.
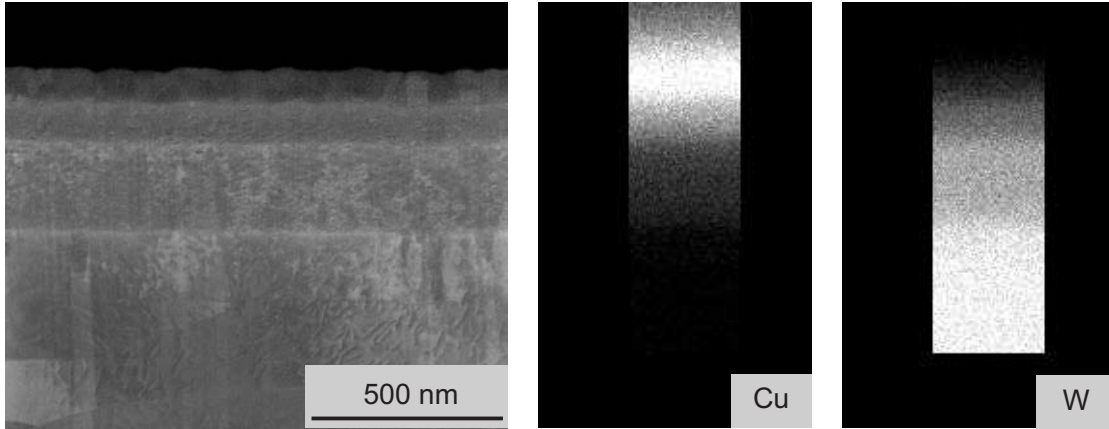
Figure 6.3: *Resolved Cu and W signal of stepwise graded W/Cu coating (interface concept concept C) measured by EDX*
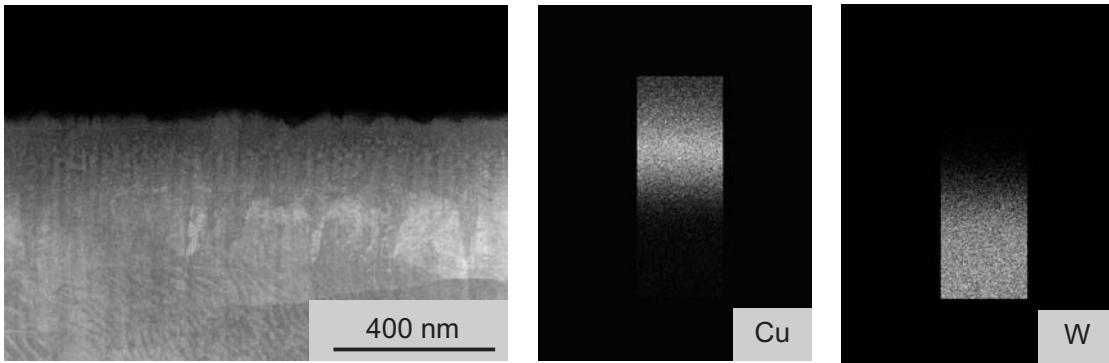
Figure 6.4: *Resolved Cu and W signal of continuously graded W/Cu coating (interface concept concept E without annealing at 800˚C) measured by EDX*

The mechanical interface properties were described by the interfacial shear strength τ_d and the interface friction stress τ_{fr} calculated from matrix-coated single fiber pull-out tests (chapter 5.4.2). The results of the five interface concepts are shown in Figure 6.5. The fitting error of τ_{fr} is very high due to extreme variations in the pullout friction P_{fr}. A possible reason for this variation can be the very small embedded length; however this was necessary to avoid premature breaking of the fiber, i.e., to analyze the interface properties, the adhesion must be smaller than the tensile strength of the fiber. The resulting data makes it difficult to interpret and compare the τ_{fr} results of the different interface concepts. Therefore, only τ_d were compared and the τ_{fr} results are presented for the sake of completeness.

The determined interfacial shear strength value of the interface concept A (no interlayer) indicates a poor mechanical interlocking in the Cu matrix. Interface concept B (Cu_{PVD} interlayer) does not indicate significant increase of interfacial shear strength.

In contrast, interface concept C (stepwise graded W/Cu$_{PVD}$ interlayer) shows a 3 fold increase in interfacial shear strength in comparison to concepts A and B. For interface concept D (stepwise graded W/Cu$_{PVD}$ interlayer + 800°C heat treatment), the additional heat treatment has a dramatic influence on the interfacial shear strength: At least a 6 fold increase in shear strength compared to concept A can be achieved which indicates a strong bonding between fiber and copper. From performed surface diffusion simulations, it is known that at 800°C surface self-diffusion is expected between W and W. It can be assumed that diffusion processes between the grains of the W fiber and the grains of the W layer of the graded transition at 800°C are responsible for the strong bonding. This assumption was verified by thermal stability tests presented in the subsequent chapter 6.1.4. A similar dramatic influence on the interfacial shear strength was achieved by depositing the continuously graded interlayer plus 800°C heat treatment, interface concept E: the shear strength increased at least by a factor 5 compared to concept A. Again, the W/W diffusion bonding is assumed to be responsible for this high bonding effect.
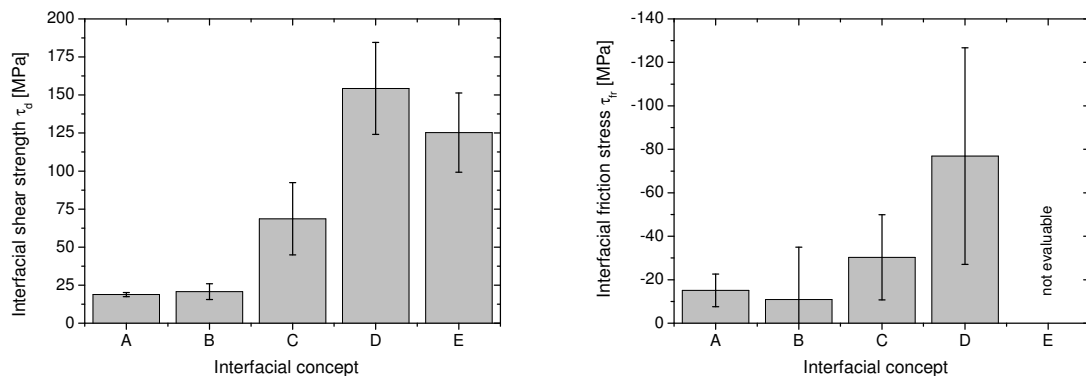
Figure 6.5: *Comparison of the interfacial shear stress and friction stress values of the different interface concepts*

As it can be seen from the failure analysis by SEM images (see Figure 6.6), the surfaces of the pulled fibers vary. Figure 6.6 A and 6.6 B, showing the pulled fibers of interface concept A and B, indicate no Cu matrix residues on the W fiber surface. The determined interfacial shear strength value indicates poor mechanical interlocking. Figure 6.6 C, showing the pulled fiber surface with the stepwise graded transition interlayer, interface concept C, shows many areas of small amounts of Cu residues on the W fiber surface. This indicates good bonding between fiber and transition layer and correlates to the higher interfacial shear strength. The SEM image of the slipped

fiber of interface concept D (Figure 6.6 D) shows large areas of W/Cu graded layer residue on W fiber surface. This system has one of the highest interface properties, which indicates strong bonding between fiber and matrix. The pulled fiber of interface concept E (Figure 6.6 E), achieving the second highest interface properties, shows an overall distribution of small Cu or more precisely continuously graded W/Cu residues on the W fiber surface indicating good adhesion between the W fiber and interlayer.
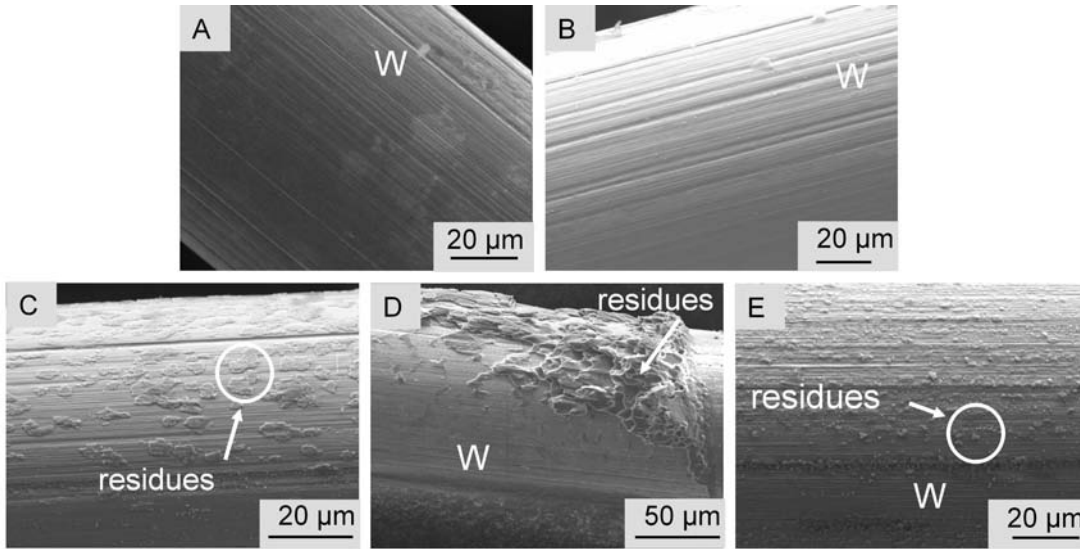
Figure 6.6: *Failure analysis by SEM images of pulled fibers of single matrix-coated samples with interface concept A, interface concept B, interface concept C, interface concept D and interface concept E*

6.1.4   Thermal stability of thin stepwise graded W/Cu coatings

Thin graded W/Cu coatings, stepwise and continuously, improved the interfacial adhesion between W and Cu. Previously shown pull-out measurements of matrix-coated single fibers showed that an up to 6 or 5 fold increase in shear strength, i.e., a stronger bonding between W fiber and Cu matrix, was achieved by depositing thin stepwise or continuously graded transition interlayers by magnetron sputter deposition and subsequent additional heat treatment at 800°C. At 800°C, W grain boundary diffusion processes were expected resulting in good bonding between coated W and the W fiber. To understand the thermal and morphological processes of the stepwise or continuously graded transition layers due to heat treatment during the synthesis of the components and during its use in the divertor, dedicated heating experiments at 550°C, 650°C and 800°C were performed. After each heating step, planar samples deposited with the stepwise graded coating were investigated regarding its nanostructure by SEM and its

phase, stress state and texture by XRD analysis. Moreover, cross-sections of the graded coating deposited on planar W substrates and on W fibers - prepared by FIB - were investigated with SEM and TEM to detect a change in the nanostructure like grain growth and diffusion processes of each layer due to the heating of the samples.

6.1.4.1 Segregation investigation of W/Cu by RBS

In preliminary investigations, the segregation effect of a nano-merged graded W/Cu coating applied in interface concept C, D and E was analyzed by RBS. Therefore, the stability of the stepwise graded transition layers, interface concept C, was investigated at 650°C. The result of the segregation experiment is depicted in Figure 6.7 which shows the RBS spectra of the stepwise graded transition before and after heating. The curves show the W and Cu peak with the different concentration steps at the specific energies. As the steps of the heated and the unheated depth profiles remain constant and no peak width variations are observed, a segregation of W and Cu can be ruled out within the scope of the RBS accuracy. However, microstructure investigation (described in detail in chapter 6.1.4.2) showed that significant changes of the nanostructure of the thin stepwise graded W/Cu coating occurred with temperature increase. It can be concluded that the RBS technique was not suitable for investigation of the thermal stability of the thin stepwise graded W/Cu coatings.
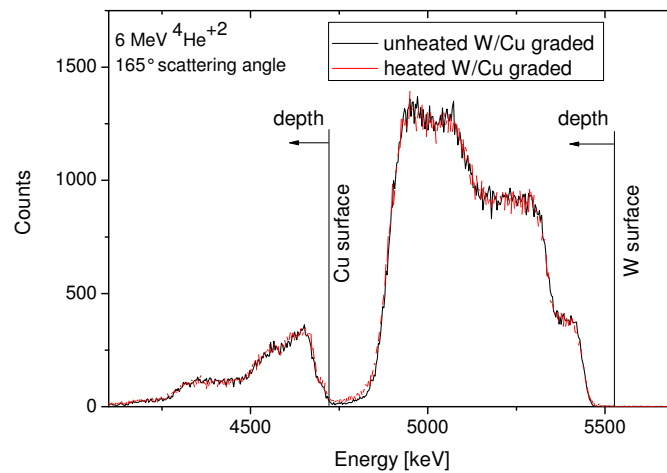
Figure 6.7: *RBS spectra of unheated and heated (650°C) stepwise graded transition from 100% W to 100% Cu*

6.1.4.2   Nanostructure and phase analysis of thin stepwise graded W/Cu coating

The microscopic investigation of the initial planar sample by SEM is presented in Figure 6.8 a). The SEM image of the cross-section obtained by FIB of the stepwise graded W/Cu coating clearly shows the five layers from 100% W to 100% Cu. The grain size differs depending on composition which was measured by RBS and extracted by means of SIMNRA program. After annealing at 650°C the nanostructure of the graded W/Cu coating begins to change slightly compared to after annealing at 550°C (Figure 6.8 b) and c)). Significant differences in the nanostructure can be seen after annealing at 800°C (see Figure 6.8 d)). The 100% Cu layer has agglomerated to islands on the surface. This process starts at 650°C. Interconnections between the W of the coating and substrate have been developed after annealing at 800°C. These two effects are caused by surface diffusion of Cu grains and Ostwald ripening of W grains. During ripening, large grains grow larger at the expense of smaller ones, thus reducing the total surface energy [146]. Energy minimization (Gibbs–Thomson effect) is the driving force for the interconnection growth. The diffusive mass transfer between grains is governed by grain boundary diffusion [147]. For a detailed description of the Ostwald ripening effect the reader is referenced to a review by Voorhees from 1985 [148].
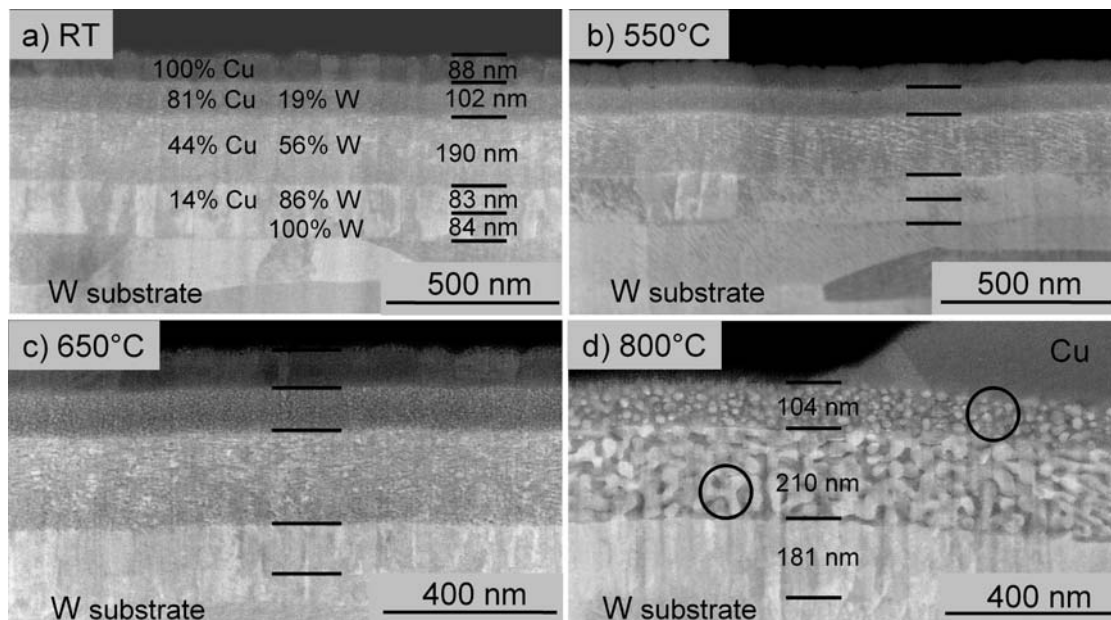
Figure 6.8: *SEM images of the cross-sections of the stepwise graded W/Cu coating on planar W substrates a) as-deposited with its five layers with thickness and composition designation and b) annealed at 800°C with merged layers and Cu islands on the top.*

Similar effects of the coating are observed on W fibers as on planar samples. The two TEM images (see Figure 6.9) show the stepwise graded W/Cu coating on W fiber. After annealing at 800°C the same formation of W structure, verified by EDX mapping, has been built by Ostwald ripening as on the planar sample. Additionally, interconnections have been formed between layers and fiber.
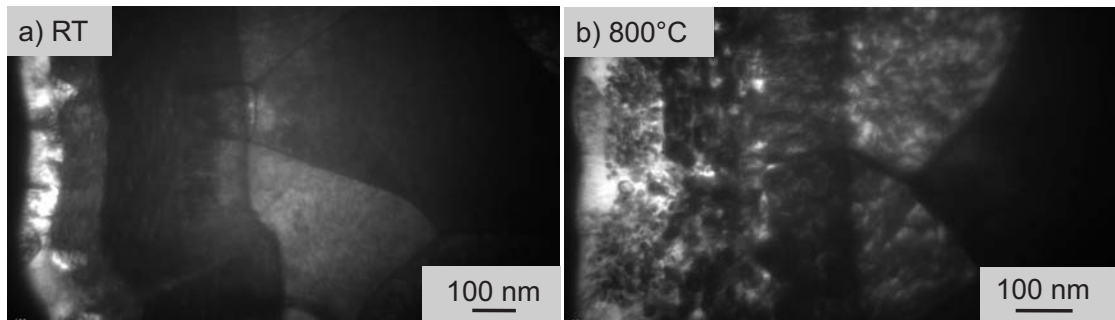
Figure 6.9: *TEM images of the cross-sections of the stepwise graded W/Cu coating on W fiber a) as-deposited and b) annealed at 800°C.*

The diffraction pattern measured by XRD demonstrated that the formed nano-structures by annealing at 800°C are pure W and Cu structures and are not affected by impurities like oxygen (see Figure 6.10). In contrast, the WO_3 (111) peak found in the diffraction pattern of the as-deposited sample has already been removed through thermal heating at 550°C. Oxygen was incorporated during the deposition process as the increase of the substrate temperature and the argon atom flux make the intra- and the intergranular oxygen diffusion easier [149].
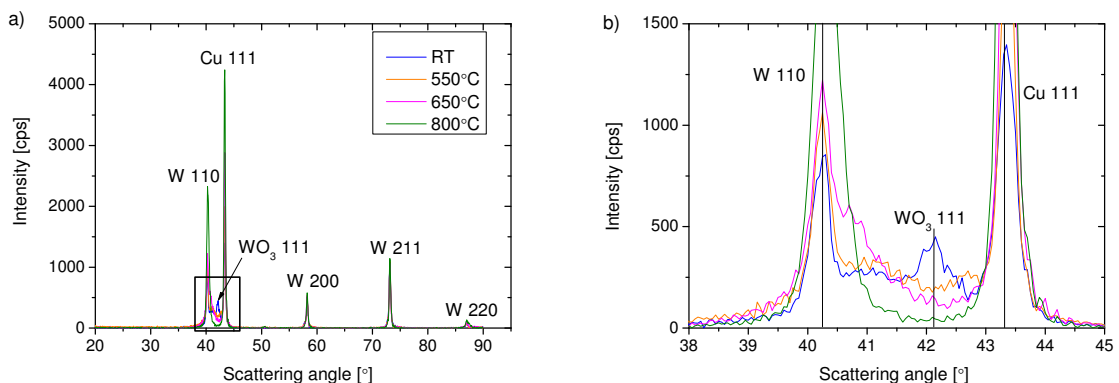
Figure 6.10: *a) X-ray diffraction pattern of graded W/Cu initial and after heat treatments at 550 °C, 650°C and 800°C with its magnification b) showing the disappearance of the WO_3 (111) peak after heating at 550°C.*

The W (110) diffraction peak (scattering angle 40.26°) was evaluated in respect to the peak width depending on the temperature. The peak width, i.e. the full width at half-maximal (FWHM) value, increases slightly from 1.3° in the as-deposited coating to 1.7° after annealing at 550°C. Then it decreases to 0.8° after annealing at 650°C and to 0.5° after annealing at 800°C. This decrease is attributed to grain growth by Ostwald ripening. Quantitative analysis of the Cu (111) peak width (scattering angle 43.32°) was not possible due to the peak shape asymmetry, which cannot be resolved in the spectra.

6.1.4.3   Texture analysis of stepwise graded W/Cu coating

After the deposition of the stepwise graded W/Cu coating, W and Cu exhibit a strong fiber texture. A commonly observed texture for fcc metallic films produced by magnetron sputtering - such as Cu - is the {111} fiber texture [150]. This is also the case for the Cu in the coating, as the pole figure of the Cu (111) peak demonstrates (scattering angle 43.32°) in Figure 6.11 a). The intensities of the diffraction peaks caused by the distribution of crystallite orientations have been recorded depending on the tilting angles from 0° to 80° and on the rotation angles from 0° to 360°. After annealing to 800°C the {111} fiber texture remains. With increasing annealing temperature the (111) peak intensity first decreases and then increases (see Table 6.1). Presently, interpretations for the decrease have not been found; however, the increase can be explained by crystallization of amorphous Cu components and crystallite growth. W pole figures of the (110) peak (scattering angle 40.26°) are presented as-deposited in Figure 6.11 c) and annealed at 800°C in Figure 6.11 d). The as-deposited and annealed W of the stepwise graded W/Cu coating is polycrystalline and shows a fiber texture in {110} direction. As already observed for Cu (111), the W (110) peak intensity first decreases and then increases with increasing annealing temperature (see Table (6.1)). Grain growth by Ostwald ripening should be primarily responsible for the increase, however contribution of thermally-induced ordering is possible. The mosaic spreads, defined as the FWHM value of the tilting scan averaged over 180° rotation, are analyzed for the Cu (111) and for the W (110) texture at RT and after annealing at 550°C, 650°C and 800°C (Table 6.1). The mosaic spread for both phases increases first and then decreases with increasing annealing temperature. The increase of the mosaic spread correlates to the decrease of the intensity of the peaks. The decrease of the peaks is caused by Ostwald ripening resulting in an increase in intensity.
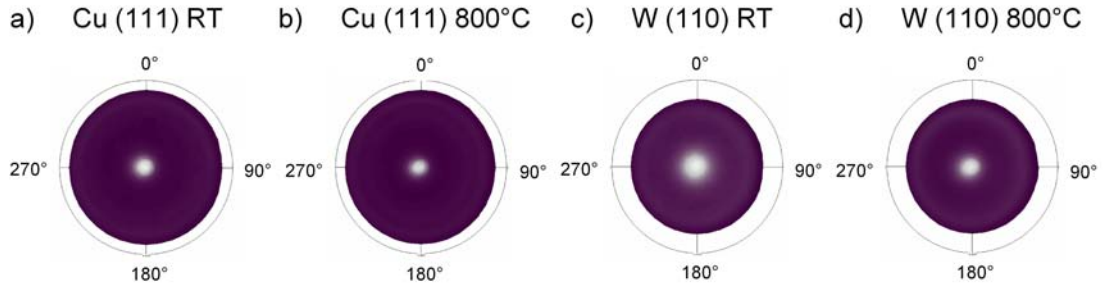
Figure 6.11: *Pole figures of the Cu (111) peak of the stepwise graded W/Cu coating on planar W substrates a) as-deposited and b) annealed at 800˚C. Pole figures of the W (110) peak of the stepwise graded W/Cu coating on planar W substrates c) as-deposited and d) annealed at 800˚C.*

Table 6.1: *Overview of the intensity, peak width and mosaic spread of Cu (111) and of W (110) depending on the temperature.*

	Temperature	Intensity [cps]	Mosaic spread [°]	Peak width [°]
Cu (111)	RT	5931	13.9±0.1	-
	550˚C	4470	18.9±0.4	-
	650˚C	8506	13.2±0.2	-
	800˚C	11393	12.4±0.3	-
W (110)	RT	4916	21.8±0.1	1.3
	550˚C	4733	27.4±0.1	1.7
	650˚C	11144	18.4±0.2	0.8
	800˚C	25804	16.2±0.2	0.5

6.1.4.4 Stress analysis of stepwise graded W/Cu coating

The biaxial residual stress state is determined for the thin graded W/Cu coating. Quantitative analysis of the Cu stress state is not possible due to the high Cu {111} fiber texture. Solely from the analysis of the W (321) peak (scattering angle 131.16°) a trend regarding the stress state of the W components in the thin graded W/Cu coatings can be concluded (see Figure 6.12 and Table 6.2). From all measured stress values by XRD, the calculated thermally induced stress of ≈ 0.1 GPa caused by the deposition process is subtracted. (Kuru showed in 2008 that the CTE of thin metal films is grain size dependent [151]. With increasing crystallite size the CTE values decrease. Thus, the calculated CTE mismatch would be slightly higher if experimental CTE values were used for the thermal stress calculation.)

Assuming the biaxial residual stress state of rotational symmetry (chapter 5.3.3) the following stresses were calculated: An intrinsic tensile stress of ≈0.7 ± 0.2 GPa of W is determined in the as-deposited coatings. After annealing at 550°C the intrinsic

tensile stress state remains stable ($\approx 0.7 \pm 0.1$ GPa) which correlates to the microscopic investigation showing that the nanostructure of the coatings have not been changed. A clear increase of the intrinsic tensile stress to $\approx 1.5 \pm 0.1$ GPa after thermal treatment at 650°C and an increase to $\approx 1.8 \pm 0.1$ GPa at 800°C are determined. At annealing temperatures of ≈ 700°C thermal stresses relief occurs in W which again correlates with the significant changes in the nanostructure. Regarding this stress relief, the measured intrinsic tensile stresses after annealing at 650°C and at 800°C are solely caused by thermal induced stresses due to the CTE mismatch of the SiO_2/graded layer interface after cooling. It can be assumed that the W-dominated layers of the coating solely contribute to the stress state. Calculation of the stresses due to the CTE mismatch by using the thermal stress equation (see equation 3.2) verified the interpretation. As the yield tensile strength (σ_{Cu}= 33.3 MPa [82]) of Cu is far below the stress state of W it can be assumed that the influence of Cu to the stress state of the coating is negligibly low, already for the as-deposited layer.

Regarding the biaxial residual stress state (Table 6.2) the anisotropy of the stress values at RT and 550°C leads to the assumption that the growth mechanism of the stepwise graded W/Cu layer was not homogeneous in plane. With the change in the nanostructure at higher temperature the influence of the intrinsic stress in W is released and the resulting thermal stress due to the CTE mismatch is homogeneous in the x- and y-direction.
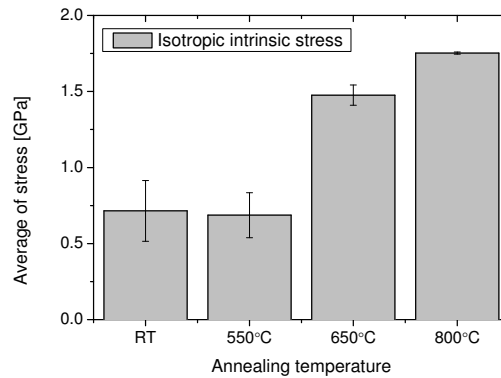
Figure 6.12: *Biaxial residual stress state of rotational symmetry of W within the stepwise graded W/Cu coating on SiO$_2$ after thermal treatments. The stress state was determined based on the W (321) peak*

Table 6.2: *Comparison of stress state under the assumption of biaxial residual stress state of rotational symmetry and biaxial stress state of W within the stepwise graded transition on SiO$_2$ after thermal treatments at 550˚C, 650˚C and 800˚C.*

W (321)	Isotropic biaxial stress state	Anisotropic biaxial stress state σ_x	Anisotropic biaxial stress state σ_y	Calculated thermal stress σ_{therm} at W/SiO$_2$ interface
RT	≈0.7 ± 0.2 GPa	1.2 GPa	0.5 GPa	-
550˚C	≈0.7 ± 0.1 GPa	1.1 GPa	0.5 GPa	-
650˚C	≈1.5 ± 0.1 GPa	1.5 GPa	1.4 GPa	1.48 GPa
800˚C	≈1.8 ± 0.1 GPa	1.8 GPa	1.7 GPa	1.83 GPa

6.1.5 Summary interface concepts

The interfacial adhesion of W and Cu is determined solely through mechanical interlocking. Interdiffusion experiments show that there are no interface reactions between W and Cu at the synthesis and operation temperatures. Segregation processes of nano-merged graded W/Cu coating was not detectable by RBS analysis.

The interfaces between W and Cu occurring within the MMC at the fiber/matrix interface were optimized to improve the interfacial adhesion by five different interface concepts. The best result was achieved by applying thin 500 nm graded W/Cu coatings, stepwise and continuously, and an additional subsequent heat treatment at 800˚C. The interfacial shear strength, i.e., the interfacial adhesion between W and Cu could be improved at least by a factor 6.

Significant changes in the nanostructure of thin graded W/Cu coatings have been observed after annealing at 800˚C. As expected, the better adhesion between W fiber and Cu matrix by implementing thin graded transitions plus additional heat treatment at 800˚C is caused by W/W grain boundary diffusion processes and Ostwald ripening of the nanometer-sized grains leading to their interconnection between each other and the W substrate. In good agreement to the microscopic investigations, the phase and texture analysis of graded W/Cu indicates grain growth and diffusion processes of pure W and Cu. The stress analysis shows that the changes in the nanostructure of the W/Cu coatings correlates to the stress relief of W at temperatures starting from 650˚C. After cooling of the coating to RT, the residual intrinsic tensile stress is caused by thermal mismatches of the substrate and the 100% W layer of the coating.

6.2   Microstructuring concepts

Six different microstructuring concepts were chosen to modify the tungsten fiber surface to achieve enhanced interfacial adhesion between the W fiber and the Cu matrix : Ion sputtering, chemical etching, fiber twisting to 20° and 30° and subsequent combinations of fiber twisting and chemical etching. This chapter focuses on the surface characterization of the modified fibers on nanometer and micrometer scale. The interface properties are discussed.

6.2.1   Surface morphology visualization

6.2.1.1   Micrometer scale - SEM

The SEM images of modified fibers (see Figure 6.13) show that different microstructuring leads to important changes on the surface of the W fibers. As the W fiber is manufactured by thermo-mechanical treatments, the surface morphology of the initial W fiber showed fine grooves oriented longitudinally along the fiber length.

SEM images of concept I (ion sputtering) (see Figure 6.13 I), indicates a smoothing effect of the surface (i.e. the peak to valley difference was smaller). As seen in Figure 6.13 II, concept II (chemical etching) causes more fine and deep grooves by etching along the longitudinal and transverse orientated grain boundaries.

Figure 6.13 III demonstrates the surface of concept III (twisting 20 $\pm$4). The surface of the fine grooves still remains continuously closed. Therefore, significant damage of the surface through twisting can not be detected on micrometer scale in contrast to concept IV (twisting 30 $\pm$4): Further twisting leads to clear damage of the fiber surface. Through the fiber elongation (the fiber was clamped and rotated by the turning lathe leading to an elongation of the fiber) cracks has formed on the grooves' surfaces (see Figure 6.13 IV). The damage of the surface results in a strong reduction of the strength of the fiber (see chapter 6.2.4). Concept V (twisting 20 $\pm$ 4 plus chemical etching), see Figure 6.13 V, causes a superposition of the resulting effects just like the surface modifications by concept VI (twisting 30 $\pm$ 4 plus chemical etching) (Figure 6.13 VI).

By comparing all six microstructuring concepts obtained by SEM analysis it can be concluded that the surface has significant variations on the microscale length.
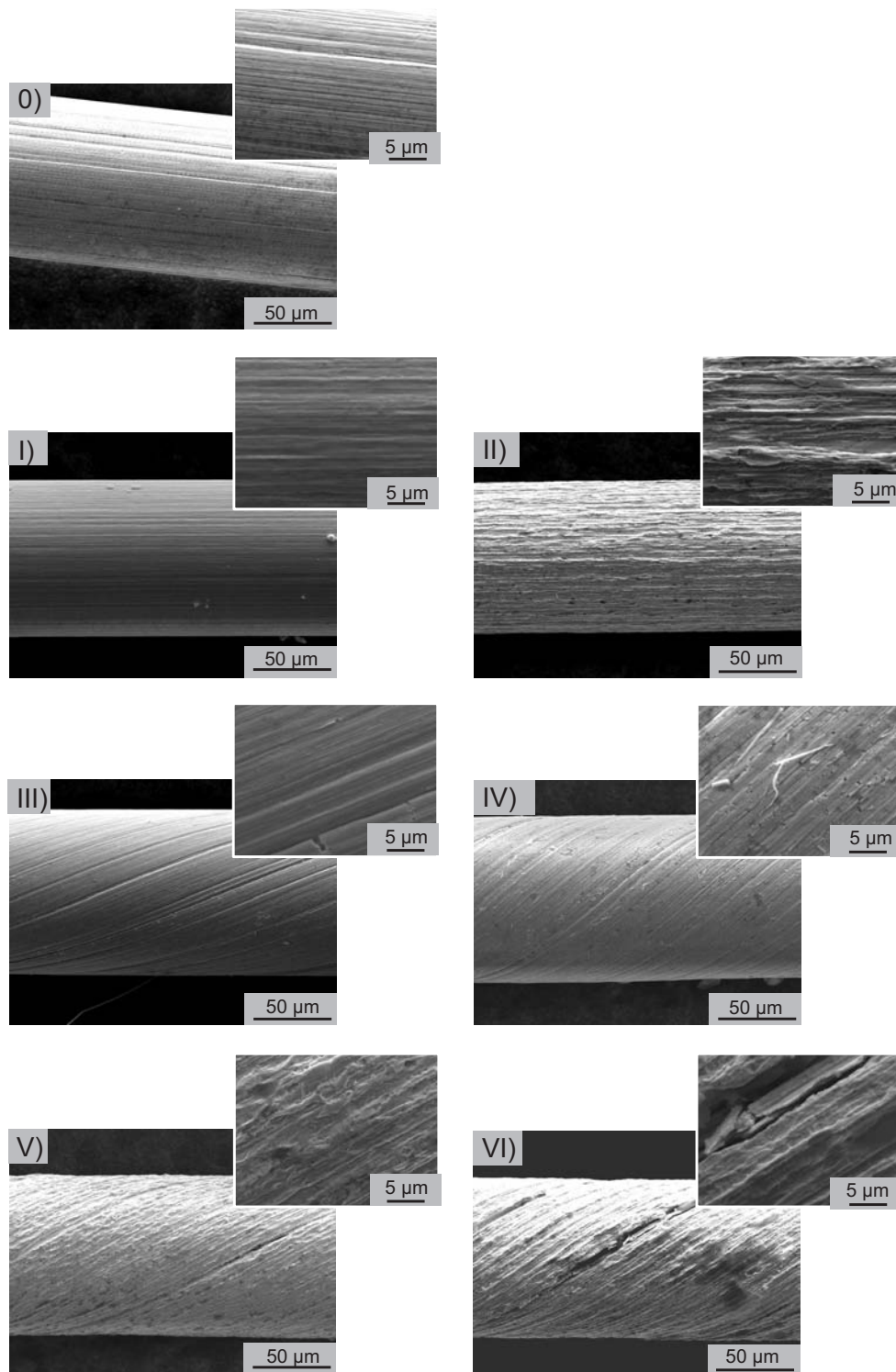
Figure 6.13: *SEM images of an initial fiber and of six microstructuring concepts: I) ion sputtering, II) chemical etching, III) fiber twisting to 20°±4°, IV) fiber twisting to 30°±4°, V) fiber twisting to 20°±4° plus chemical etching and VI) fiber twisting to 30°±4° plus chemical etching.*

6.2.1.2   Nanoscale Analysis - AFM

AFM measurements were performed on the surfaces of the initial and microstructured fibers. The resulting AFM scans, showing the surface morphologies of each concept, are compared in Figure 6.14. Observing the cross-sectional profiles, as shown in Figure 6.15 I - VI, the variation in grooves' heights and widths of the tungsten fiber are seen and compared with a cross-sectional profile of the initial fiber. The profile line was set perpendicular to the grooves orientation (see Figure 6.14, lines).

Comparing the profile of concept I with the initial one, a two fold reduction of height differences between the peaks and valleys is observed. Additionally, fine ion sputtered grooves can be detected on a nanometer scale in the AFM images at higher magnification as well as in the profile scan.

The profile of concept II (see Figure 6.14 II) demonstrates larger height differences between the peaks and valleys than the initial one. This is in good agreement with the observations from SEM images.

The AFM image of concept III, Figure 6.14 III, demonstrates, in contrast to the SEM images, damage to the surface along the longitudinal direction. Therefore, the elongation of the fiber, bursting the fine grooves surface, can be detected in the nanometer scale. The cross-sectional profiles indicate a decrease of peak height caused by the elongation effect of the fiber surface.

Concept IV also causes damage to the surface in the longitudinal direction (see Figure 6.14 IV). The damage is detected in both nanometer and micrometer scale. Comparing the cross-sectional profiles of concept IV with the initial one, an obvious decrease in the peak height is seen. No clear difference is distinguishable comparing the cross-sectional profiles and the AFM images of concept III with concept IV in the nanometerscale.

Figure 6.14.V shows the concept combination of twisting to $20°\pm4°$ and chemical etching, concept V. It indicates that in addition to the surface damage, there is a roughening effect by chemical etching. Similarly to the micrometer scale, a superposition of the two concept effects appears.

This can be considered accordingly for the AFM image of concept VI, see Figure 6.14 VI, showing a superposition of stronger twisting and chemical etching. The cross-sectional profiles of the combined concepts indicate that the height differences between the peaks and valleys is not distinguishable to the initial ones.
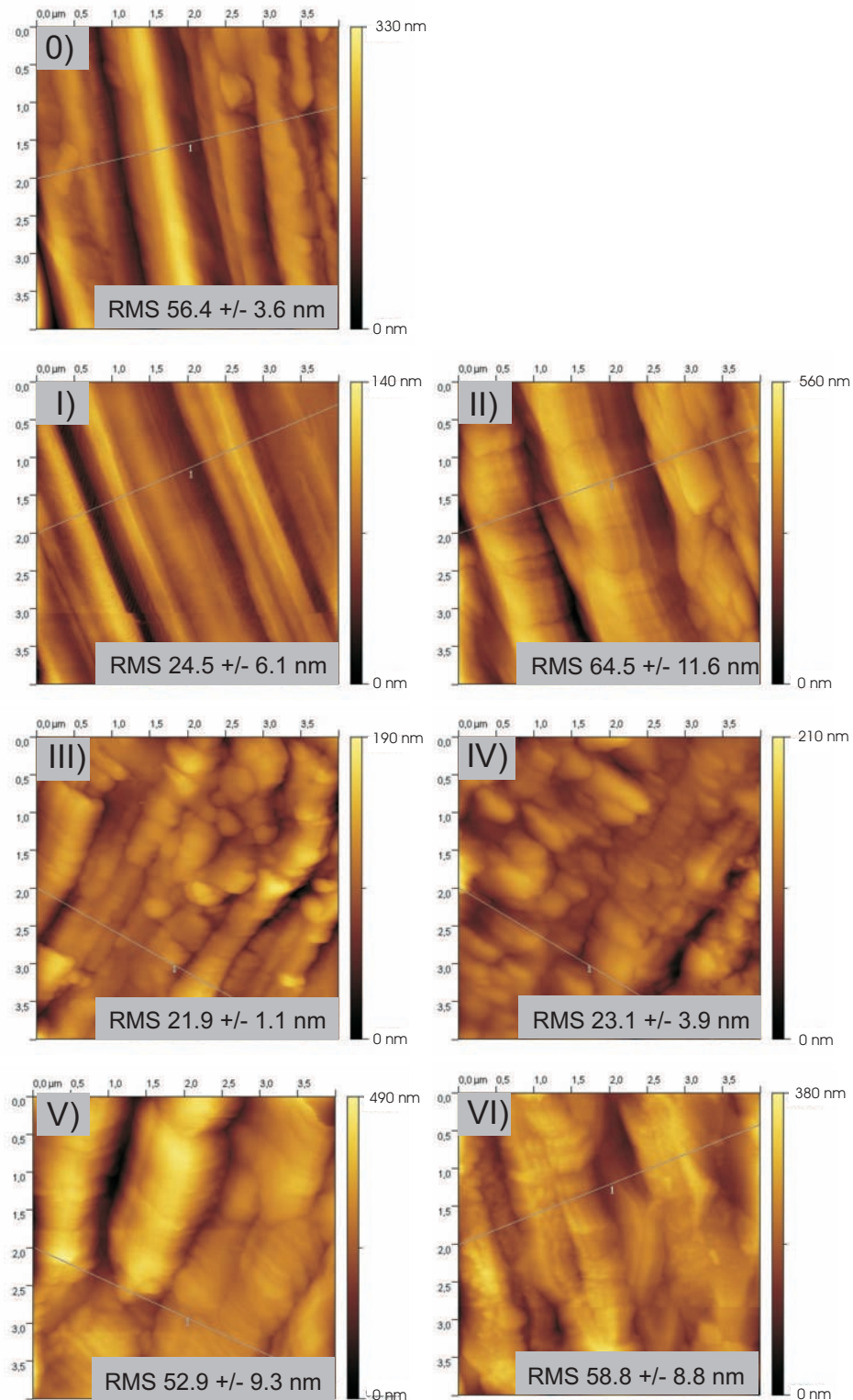
Figure 6.14: *4 μm x 4 μm AFM images of the initial tungsten fiber and of the six microstructuring concepts: I) ion sputtering, II) chemical etching, III) fiber twisting to 20° ± 4°, IV) fiber twisting to 30° ± 4° V) fiber twisting to 20° ± 4° plus chemical etching and VI) fiber twisting to 30° ± 4° plus chemical etching. The lines indicate the position of the extracted cross-sectional profiles of Figure 6.15.*
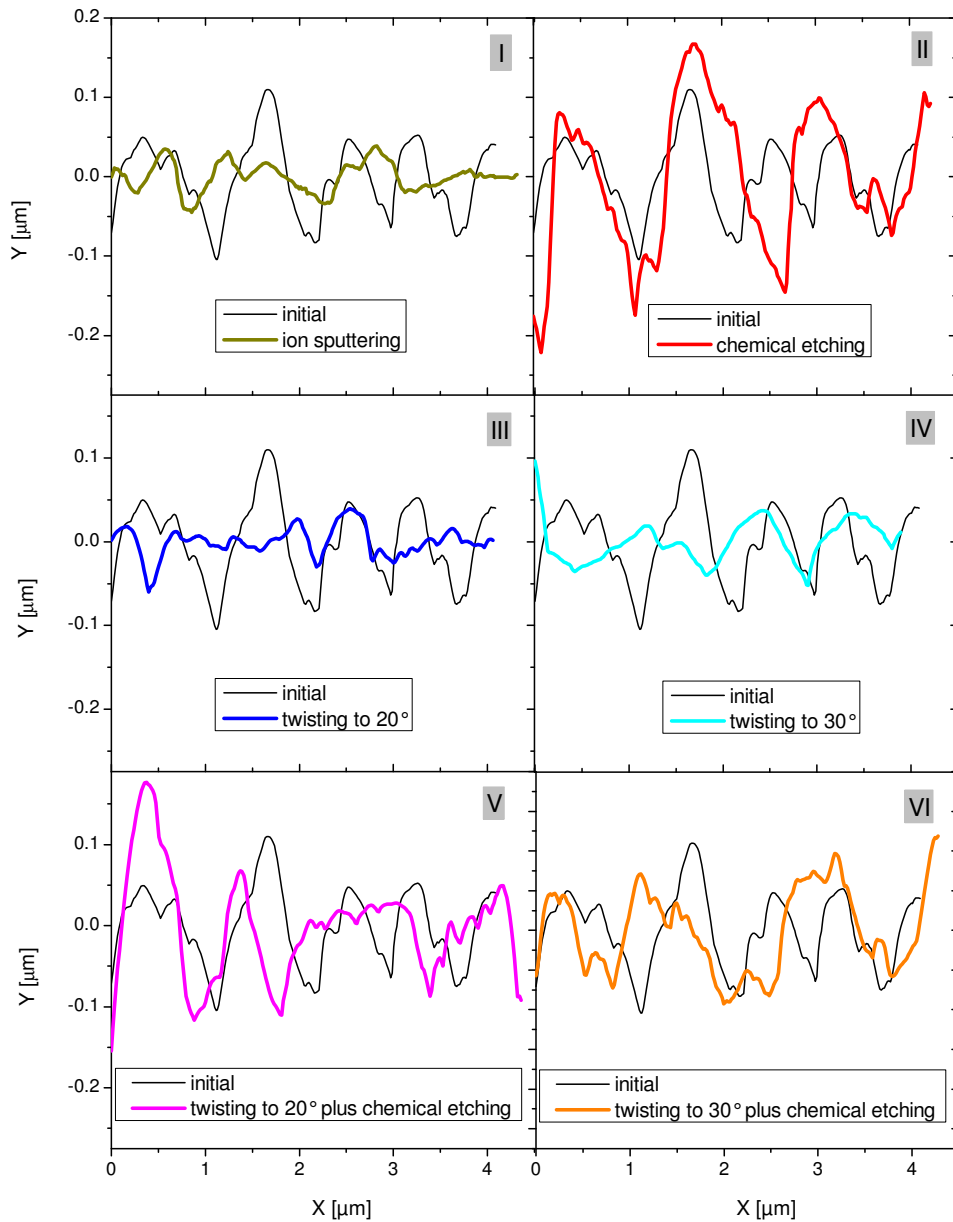
Figure 6.15: *Extracted cross-sectional profile of the six different microstructuring concepts compared to the cross-sectional profile of the initial fiber*

6.2.2 Roughness analysis

The RMS surface roughness, skewness and kurtosis were determined by averaging the values from three AFM data of 4 µm x 4 µm area for each microstructuring concept.

The RMS surface roughness values are presented within Figure 6.14 and additionally summarized in Table 6.3, while skewness and kurtosis values are presented in Figure 6.16.

The RMS roughness of concept I is seen to be smoother than the initial surface, corroborating the optical interpretation from SEM and AFM data. The RMS value of concept II surface does not indicate a significant roughening effect on a nanometer scale compared to the initial surface. The RMS values of concept III and concept IV indicate lower roughness due to surface elongation which results in peak reductions. This is in good agreement with the earlier interpretation from the micrometer scale analysis presented in chapter 6.2.1. The roughness values of the microstructuring concept V and VI, are dominated by the effect of chemical etching and resembles the RMS values of the initial fibers.

In summary, the RMS roughness is reduced by ion sputtering and twisting while chemical etching results in roughness values similar to that of the initial fibers.

Table 6.3: *Comparison of the measured average RMS roughness for the 4 µm x 4 µm scanned areas of different microstructuring concepts*

No.	Microstructuring concept	RMS [nm]
0	Initial	56.4±3.6
I	Ion sputtering	24.5±6.1
II	Chemical etching	64.5±11.6
III	Twisting 20 ± 4	21.9±1.1
IV	Twisting 30 ± 4	23.1±3.9
V	Twisting 20 ± 4 + chemical etching	52.9±9.3
VI	Twisting 30 ± 4 + chemical etching	58.8±8.8

Since microstructuring concepts II, V and VI show similar RMS values as the initial fiber, skewness values were determined to distinguish between the profiles and their symmetries (see Figure 6.16 a)). The skewness of the initial fiber and microstructuring concept VI was found to be approximately zero, indicating a symmetrical height distribution with as many peaks as valleys. The skewness of the microstructuring concept I, II, III, IV and V were negative, indicating that peaks were reduced or scratches were deeper. It is noted that concepts II and V have the most negative values, and chemical etching resulted in peaks that were smoothed and/or the initial grooves being etched deeper into the fiber.

The kurtosis of the profile distinguishes between two profiles having the same or similar RMS values but different periodicity (see Figure 6.16 b)). The kurtosis parameter of the microstructuring concepts I, II and VI, are slightly negative. Thus,

the distribution curve is platykurtic, which is equivalent to a few high peaks and low valleys. The distribution curves of concepts III, IV and V are leptokurtic, which is equivalent to many high peaks and low valleys. Therefore, the twisting process increases the periodicity of the peaks corroborating the earlier observation that fiber elongation bursts the finely grooved surface and forms more peaks.
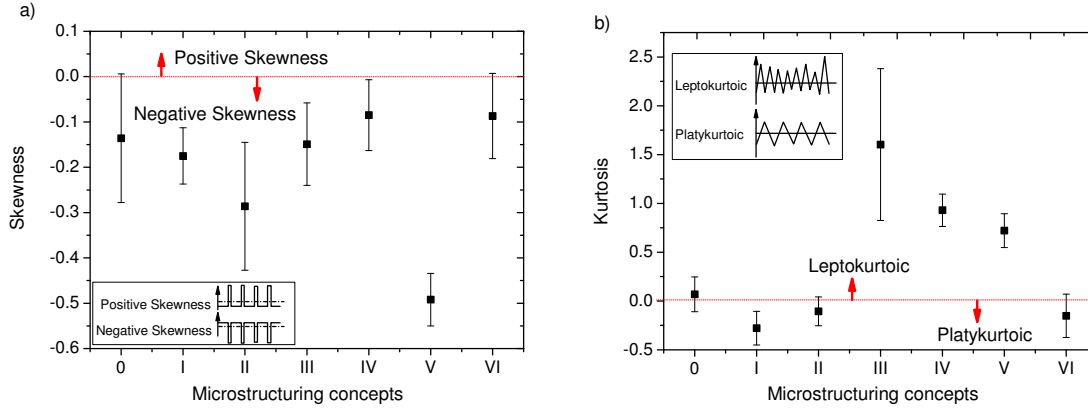
Figure 6.16: *Overview of a) skewness and b) kurtosis values of the initial fiber and of the six different microstructured fibers*

6.2.3   Surface area

Surface enlargement from the various microstructuring concepts was analyzed using the triangulation method based on AFM data. In Figure 6.17, the ratio of the real surface to the projected surface is compared for each microstructuring concept.

The surface ratio values, presented in Figure 6.17, indicate that concept I, III and IV lead to a decrease in surface area. The differences between the initial surface area and the modified surface areas of microstructuring concepts II, V and VI were slightly less. The variation of all ratios is solely $\approx$10 %. Therefore, no surface enlargement and consequently, no increase in contact area can be achieved on a nanometer scale using modification the surface by the six microstructuring concepts.

6.2.4   Fiber strength

Tensile tests were performed on the initial and modified fibers. The results are shown in Figure 6.18. The data verified the expectation that the surface modifications weaken the fiber strength.
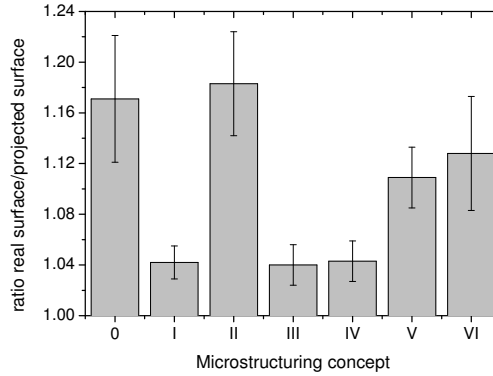
Figure 6.17: *Comparison of the surface enlargement of the six different microstructuring concepts against the initial fibers. Derived from the average of the 4 μm x 4 μm and 2 μm x 2 μm scanned areas.*

Through the production process the initial tungsten fiber is compressed with a phase structure. The strong bonding between the different phase crystalline fiber in the longitudinal direction combined with the high crystal strength explain the initial fiber tensile strength.

Ion sputtering had the lowest impact on fiber strength. Chemical etching also had a relatively low impact on the fiber strength. Therefore, the more nanoscopic modifications of the fiber by ion sputtering and chemical etching (see also chapter 6.2.1.2) do not affect the strength dramatically. This is in contrast to microscopic modification inducing concepts like fiber twisting. It was observed that the tensile strength of the twisted fibers decreased with increasing twisting angle. The combination of the concepts reduces the strength of the fiber even further resulting in highest loss of tensile strength. The twisting to 30° ±4° and chemical etching damages the surface and cause inner plastic deformation, stress and dislocations which are responsible for the low UTS value.

6.2.5   Interfacial adhesion

The mechanical interface properties are described by the interfacial shear strength τ_d and the interfacial friction stress τ_{fr} calculated from single fiber pull-out tests. Like in the pull-out measurements of the different interface concept, the fitting error of τ_{fr} is very high as the pull-out friction P_{fr} varied extremely due to the low embedded matrix lengths. Therefore, only τ_d is discussed, as it can be seen in Figure 6.19. The comparison of the τ_{fr} is presented in Figure 6.19 for completeness.
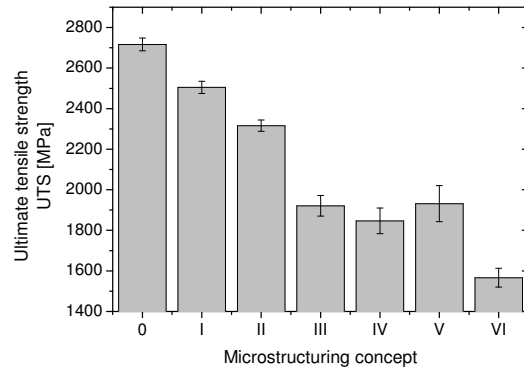
Figure 6.18: *Fiber strength of initial and microstructured fibers*

The τ_d value of ion sputtering indicates a poor mechanical interlocking in the Cu matrix. Chemical etching results in an increase of τ_d indicating a stronger bonding between the fiber and the Cu matrix. The twisting procedure has a dramatic influence on τ_d: higher twisting angles result in stronger adhesion between the fiber and matrix. An increase in τ_d of at least three fold can be achieved by twisting to 30°±4°. This increase in strength is achieved by the twisted fiber being mechanically interlocked in the matrix like a screw. The combined concepts of twisting to 20°±4° or 30°±4° plus chemical etching also results in higher τ_d compared to the initial one.

To summarize, all microstructuring concepts with the exception of ion sputtering result in an increase in interfacial adhesion between the fiber and the surrounding Cu matrix. As no surface enlargement and, consequently, no increase in contact area can be achieved on a nanometer scale (see chapter 6.2.3), the achieved higher interfacial adhesion is caused solely by a roughening effect on micrometer scale.

6.2.6 Summary microstructuring concepts

The interface between W fiber and Cu matrix was optimized by microstructuring the fiber surface to achieve enhanced adhesion. Six different microstructuring concepts were chosen: Ion sputtering, chemical etching, fiber twisting to 20°±4° and 30°±4° and the combination of fiber twisting and chemical etching.

The surface modification of the fibers were characterized on both the nanometer and micrometer scale. The resulting analysis showed that the surface had significant variations on the microscale length like smoothing effects due to ion sputtering, roughness increment due to chemical etching, and surface cracks due to twisting. The comparison of the RMS values showed that the RMS roughness was reduced by ion sputtering
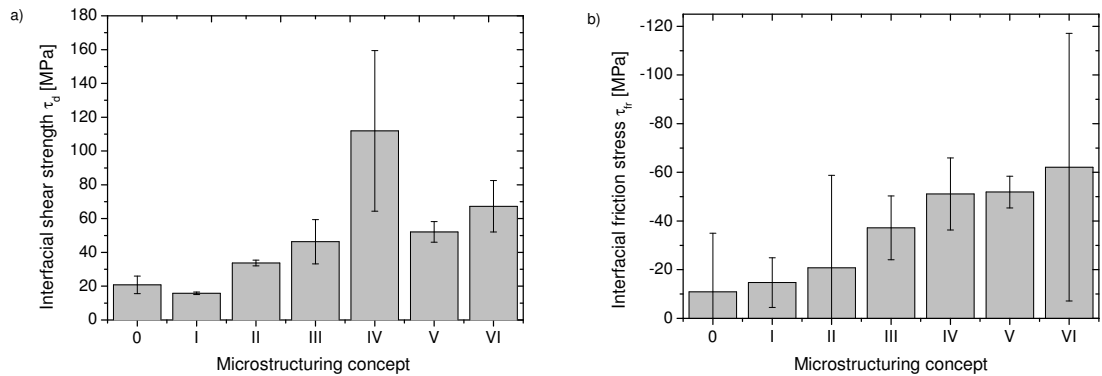
Figure 6.19: *a) Interfacial shear strength τ_d and b) interfacial friction stress τ_{fr} of the six different microstructuring concepts*

and twisting. Chemical etching and the combined microstructuring concepts showed a roughness effect but did not exceed the roughness of the initial fiber. Skewness analysis showed that all concepts, except twisting to 30° ±4° plus chemical etching reduced the peaks and/or formed deeper scratches. The comparison of the kurtosis values pointed out that the twisting process increases the periodicity of the peaks. Surface enlargement analysis showed that there was no enlargement of the contact area on a nanometer scale. Therefore, the mechanical interlocking was caused on a micrometer scale leading to an adhesion increase between fiber and matrix.

In addition, mechanical characterization of fibers were performed. Tensile tests demonstrated that the surface modifications weaken the UTS of the fibers. The interfacial strength was determined from single fiber pull-out tests. A general increase in interfacial shear strength resulted from the microstructuring concepts with the exception of ion sputtering. Fiber twisting to 30° ±4° was found to achieve the highest interfacial shear strength, with a three fold increase in strength. For further application of the microstructured fibers, a balance must be found between interfacial adhesion, fiber strength and technical feasibility. Therefore, chemical etching was chosen to be the optimal concept to be applied on the fibers for further application in the monoblock mock-up (see chapter 7).

6.3   Investigations on improved W_f/Cu MMCs

In this chapter, micromechanical properties of improved W_f/Cu MMCs were investigated. Multi-fiber MMCs with selected concepts were synthesized and validated with respect to different criteria: 1) The O content of MMCs was measured via RBS. This analysis gave information about the quality of the synthesis process of the MMCs. 2) Thermal cycling test of the MMC with graded interlayer should validate the functionality of CTE adaptation qualitatively. 3) Supplementary, in-situ stress measurements during thermal cycling via neutron diffraction were chosen to quantitatively validate the graded interface concepts which should be implemented in the monoblock mock-up.

6.3.1   Oxygen content

Impurities like O strongly influence the mechanical properties (via changes in the microstructure) including strength, toughness and thermal conductivity of Cu and W and consequently of the MMC. Additionally, the O content gives an idea whether the interfaces between W/Cu are affected by the formation of Cu-oxide or W-oxide. Therefore, it is essential to validate the applied synthesis process regarding the purity of the MMC.

For the determination of the O content of the composite, one MMC disc was bombarded with a 1 mm x 1 mm ^{3}He$^+$ beam with 2.5 MeV until a charge of 40 µC was collected. The underlying nuclear reaction was ^{16}O (^{3}He$^+$, p)^{18}N. To obtain depth information the initial kinetic energy of the ions and their stopping power (energy loss per distance traveled) in the sample had to be considered. From the received proton spectra the integral of the O peak of an electroplated plus outgassed Cu sample and of the W_f/Cu MMC (with interface concept C) were analyzed (Figure 6.20 a) and b)). For quantitative determination of the O content the integrals were compared with the integral of the reference bulk SiO_2 sample (Figure 6.20 c)). It was assumed that the oxygen is dispersed homogeneously within the samples. By nature, the peak integral from the SiO_2 spectrum corresponds to an O content of 66 % in the information depth. The information depth of Cu was determined to be half of that of SiO_2. Thus, the O content of the W_f/Cu MMC was calculated to be ≈0.6 % and of the electroplated plus heat treated Cu to be ≈0.4 %.

The electroplating and the consolidation steps are the critical steps during the synthesis process where O can be incorporated. Popescu [84] showed already that slow outgassing at 550°C for 1 h with a slow heating rate of 20°C/h after the electroplating process reduce the O content. Regarding the O content of the W/Cu MMC compared
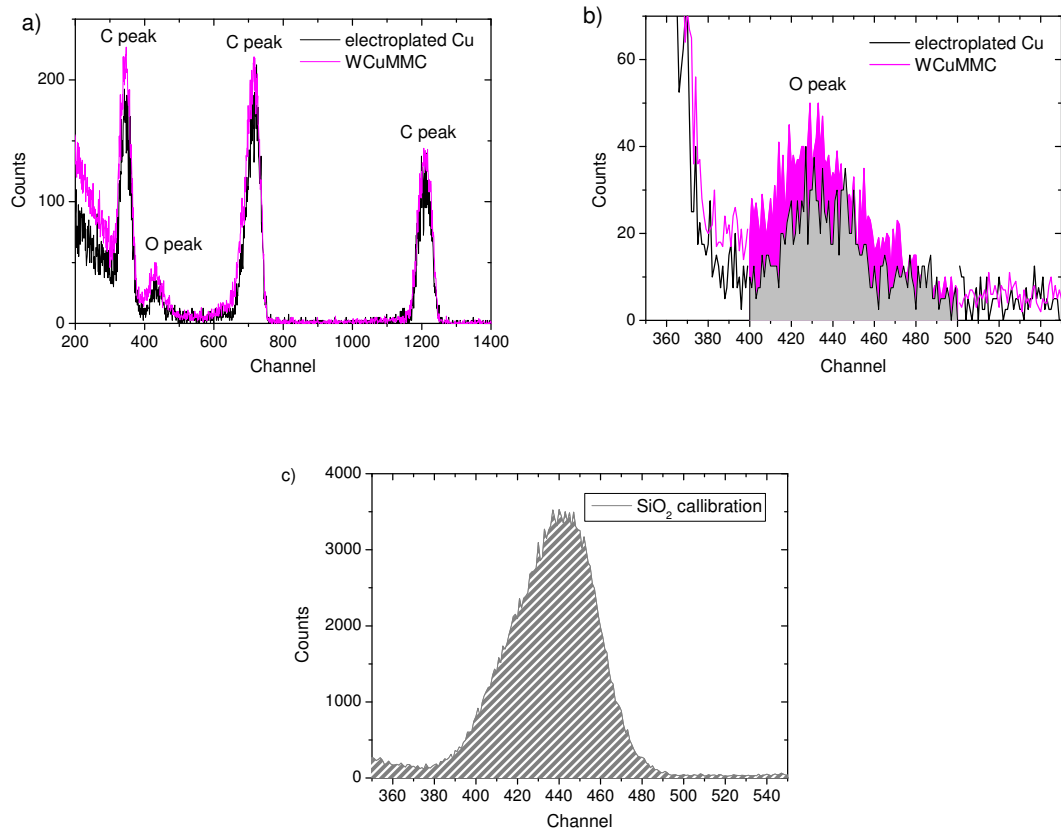
Figure 6.20: *a) NRA protons spectrum of W_f/Cu MMC with interface concept C and of electroplated Cu bombarded with 2.5 MeV $3He^+$; b) Curve integral of the O peak of W_f/Cu MMC and of electroplated plus heat treated Cu to extract the O content of the samples; c) Curve integral of the O peak of the reference SiO_2 sample*

to the one of the electroplated samples there was no significant increase of O in the MMC. Thus, it can be concluded that the MMC synthesis process, in particular the consolidation process, did not incorporate more O and that the interfaces of W and Cu were most likely free of oxide.

6.3.2   Thermal behavior of improved MMCs

Thermal cycling was performed for thermal stability testing of improved W_f/Cu MMCs. The SEM images (Figure 6.21) show the two investigated MMC discs containing initial fibers coated with the interface concept B and C after the thermal cycling test. The W fibers of the MMC with the interface concept B debonded during thermal cycling which indicated a weak interfacial adhesion (see Figure 6.21 a) and b)). In contrast,

the fibers with interface concept C, depicted in Figures 6.21 c) and d), showed that the fibers bonded to the matrix and that the displacements occurred solely at the Cu grain boundaries. This indicated a strong bonding between fiber and matrix. It was assumed that the stepwise graded transition between W fiber and Cu matrix acted as stepwise adaptation of CTE mismatch between W fiber and Cu matrix during cycling.
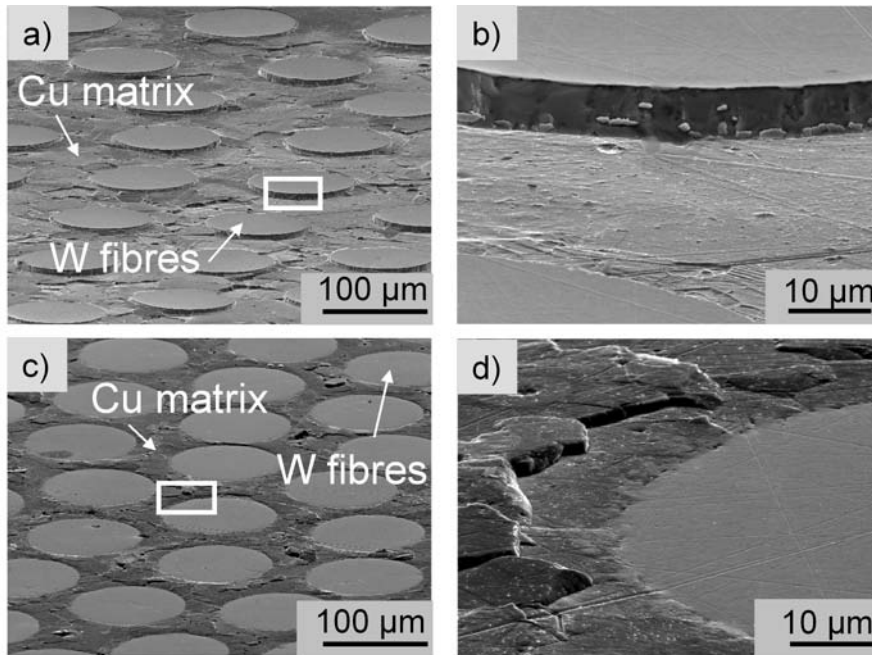
Figure 6.21: *SEM images of the two investigated MMC discs after thermal cycling: a) and its magnification b) show the MMC consisting of unstructured fibers (microstructuring concept 0) coated with Cu_{PVD} interlayer (interface concept B); c) and its magnification d) show the MMC consisting of unstructured fibers coated with the stepwise graded W/Cu_{PVD} interlayer (interface concept C); All MMC samples were hipped at 650°C.*

6.3.3 Residual stresses in improved MMCs during thermal cycling

An qualitative proof of the functionality of graded W/Cu coatings was shown in the previous chapter 6.3.2. A quantitative supplementation are in-situ residual stress measurements of multi-fiber MMCs with neutron diffraction. Two MMCs with interface concept B (Cu_{PVD} interlayer) and E (continuously graded W/Cu_{PVD} interlayer but without 800°C heat treatment) were chosen for residual stress measurements during thermal cycling leading to a quantitative validation of the graded transition concept. The reference MMC 1 and the MMC 2 were thermally cycled and analyzed regarding

the residual stress state and internal microstructure conditions.

The residual matrix stresses of the MMCs during two thermal cycles are shown in Figure 6.22. Compressive stresses were generated during heating through longitudinal and transverse expansion of the Cu matrix. The decrease of matrix stresses at high temperature ($\approx$400°C) indicated plastic deformation, i.e., stress relaxation of the matrix at the interface. Thus, during cooling to RT the matrix shrinks and tensile stress results in the matrix. Possible debonding between fiber and matrix, indicated by decreasing stress amplitudes during thermal cycling, could not be detected.

A clear difference was observed between MMC 1 and the MMC 2. MMC 2 showed a lower residual stress maxima due to stress distribution over the continuously graded interface region leading to a stress reduction at the fiber/matrix interface. In consideration of the qualitative investigation of the functionality of graded W/Cu coatings (chapter 6.3.2), it can be expected that the long term stability of MMC 2 is higher than MMC 1. This will be investigated in the next measurement campaign where the MMC samples will be thermally cycled 50 times between RT and 550°C.

The stress variations in the fibers are more accurate compared to matrix stresses because of their bigger strain affected volume fraction. It can be assumed that the whole fiber volume is almost homogeneously deformed by the expanding matrix. However, fiber stresses are difficult to evaluate due to its texture. The strong textured W fibers allow strain measurements solely in longitudinal direction.

The W (220) peak was identified in MMC 2 and was used for stress calculation of the fiber. Figure 6.23 shows the comparison of the longitudinal stresses of fiber and matrix of the MMC 2 during thermal cycling. The W fibers compensate the compressive stresses of the matrix by tension according to their volume fraction (fiber volume fraction $\approx$ 20%). The relation of 1:5 fiber to matrix correlates to the ratio of maximal Cu matrix stress of -150 MPa to the maximal W fiber stresses of +750 MPa. Equivalent to the evolution of the matrix stress, the fiber stress decreased from $\approx$400°C and at RT the fibers were compressed.
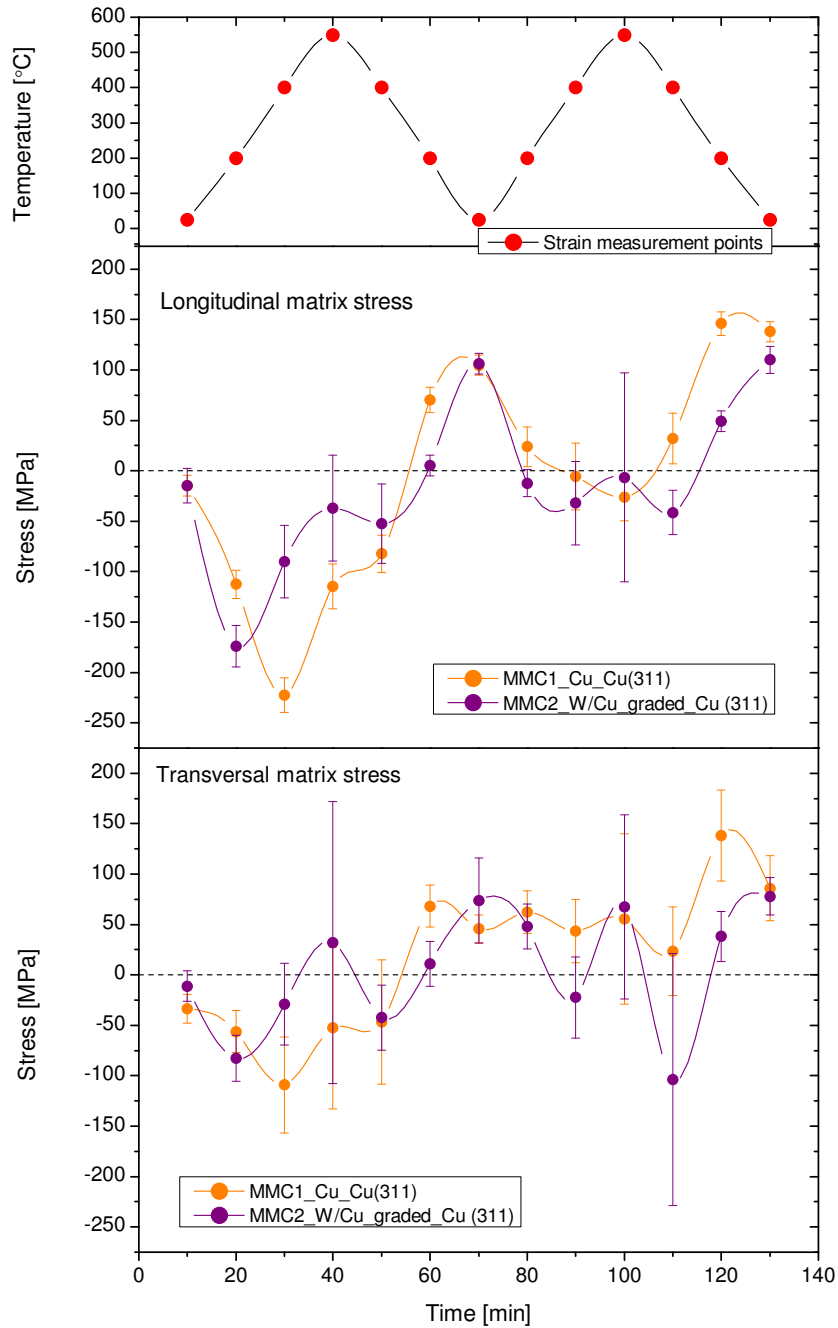
Figure 6.22: *Residual stresses of matrix of MMC 1 (composite with initial W fibers with Cu_{PVD} interlayer) and of MMC 2 (composite with initial W fibers with continuously graded W/Cu_{PVD} without 800°C heat treatment) in longitudinal and transverse direction measured by neutron diffraction*
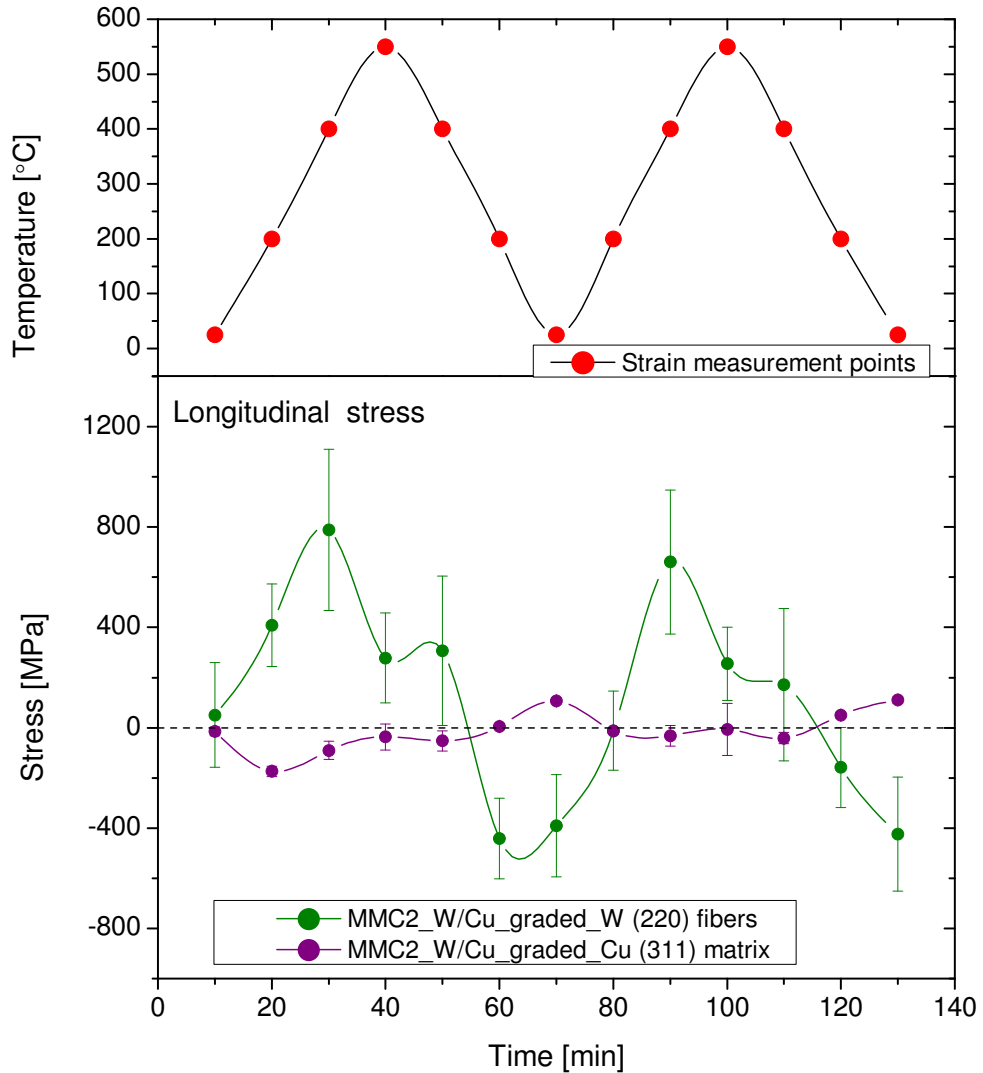
Figure 6.23: *Residual stresses of fibers and matrix of MMC 2 measured by neutron diffraction*

6.3.4 W/Cu graded transition as joining layer between MMC and PFM

As a result of the investigations of the stepwise graded W/Cu at different temperatures (see chapter 6.1.4) and resulting higher adhesion between W and Cu on nanoscale due to heat treatment to 800°C, a transfer to the next higher length scale (mm - scale)

seems logical. The deposition of a continuously graded W/Cu interlayer may act as an effective joining technology due to diffusion bonding of the reinforced cooling tube to the W tile at lower process temperatures. The lower process temperatures would reduce the stresses at the interface occurring in the cool down process after processing. Therefore, some pre-tests were performed to apply the bonding technology.

The reinforced cooling tube surface was coated with a ≈ 1 µm thick continuously graded W/Cu transition from 100 % Cu to 100% W. The deposition was carried out analogously to the deposition described in chapter 5.1.1 but in the inverse way and by changing the concentrations every second minute. The reinforced cooling tube with the coating was press-fitted in the four center aligned W tiles to obtain a cylindrical interference fit. Subsequently, the component was heat treated at 800°C for 1 hour to achieve a bonding between the W tiles and the last W layer of the transition.

The bonding technology failed due to the fact that the stress due to shrinkage of the cooling tube was stronger than the diffusion bond of W and W. The stress at the interface was assumed to be higher than the adhesion of the bonding. Higher temperature or longer heating duration of the diffusion bonding process might have resulted in a stronger bonding because a higher diffusion coefficient results at higher temperature [152]. In turn, the low melting Cu-based components of the MMC do not allow high temperature (<1084°C) and the higher the temperature the higher the stresses at the W fiber/Cu matrix interface. It can be concluded that Ostwald ripening and W self diffusion processes at 800°C were effective on nanometer scale but not on larger scale.

Thus, an alternative bonding technology is required. In the framework of ITER R&D investigations several joining technologies have been developed and applied [9]. Besides the casting technology to join pure Cu onto W, several methods are available as electron beam welding, brazing or HIP. Therefore, it was decided to use a well established joining technology with a low process temperature, the brazing process with GEMCO material.

6.3.5   Summary improved W_f/Cu MMCs

It can be summarized that the MMC synthesis process, in particular the consolidation process, did not incorporate more O and that the interfaces of W and Cu are most likely free of oxide.

From the investigated interface concepts, the graded transition interface with additional heat treatment was found to achieve the highest interfacial shear strength (see summary 6.2.6). Thermal cycling tests showed that the thermal stability of the MMC

can be assured by depositing a stepwise graded transition between W fiber and Cu matrix. It can be assumed that the stepwise graded transition between W fiber and Cu matrix acts as a stepwise adaptation of CTE mismatch between W fiber and Cu matrix.

In-situ stress measurements were performed on two different MMC concepts to quantitatively validate the functionality of the graded transition. Residual stresses in the Cu matrix up to 200 MPa were built up during thermal cycling between RT and 550°C. Plastic deformation of the matrix (creep) is shown by stress inversion after cooling due to matrix shrinkage. The W fibers compensate the compressive stresses of the matrix by tension according to their volume fraction. Debonding between fiber and matrix was not detected. Clear differences in residual stress levels between the MMCs without interface and with continuously graded transition were observed. Thus, the graded transition leads to stress reduction at the fiber/matrix interface.

The deposition of a continuously graded W/Cu interlayer may act as an effective joining technology to diffusion bond the reinforced cooling tube to the W tile. Ostwald ripening and W self diffusion processes at 800°C were effective processes on nanometer scale to bond W and W. To achieve a stronger, stable bonding on millimeter scale, higher temperature or longer heating duration are necessary.

Chapter 7

Assessment of optimization concepts

7.1   Advantages and disadvantages

All results of the interface optimization (see chapter 6) were taken into consideration to identify the optimal interface and microstructuring concepts for their further application. Besides the positive effects of the different concepts like enhanced interface adhesion and/or adaptation of thermal mismatch between W fiber and Cu matrix, it requires that the concepts can be easily realized for further processing to novel W_f/Cu MMCs and implementation in two monoblock mock-ups. Therefore, four eligibility criteria were determined to evaluate the optimal concepts:

1. Effect on interfacial adhesion

2. Effect on thermal mismatch of W fiber and Cu matrix

3. Effect on tensile strength of the fibers

4. Feasibility of concept

In the following, each concept is evaluated and rated. The results are presented in Table 7.1. The grades range from a negative effect, "-", over zero effect, "0", to very high effect, "+++". For no influence the symbol "/" was used.

Interface concepts

The highest interfacial adhesion between W and Cu was achieved by applying thin 500 nm graded W/Cu coatings, stepwise (interface concept D) and continuously (interface concept E), with a subsequent heat treatment at 800°C. The interfacial shear strength

Interface optimization concepts	Eligibility criteria			
	Enhanced interfacial adhesion	Adaptation of thermal mismatch	Tensile strength of the fibers	Feasibility
A	Ref	-	/	+++
B	0	/	/	+++
C	+	+	/	+++
D	++	++	/	+++
E	++	++	/	+++
0	Ref	/	Ref	+++
I	-	/	+++	+
II	+	/	++	+++
III	++	/	+	-
IV	+++	/	+	-
V	++	/	+	-
VI	++	/		-

Table 7.1: *Advantages and disadvantages of each interface and microstructuring concept at a glance*

could be improved at least by a factor 6 and factor 5. In addition, neutron diffraction investigations and thermal cycling on multi-fiber MMCs indicate that the graded transitions between W fiber and Cu matrix act as stepwise adaptation of CTE mismatch leading to stress reduction at the fiber/matrix interface. Significant differences between the stepwise and continuous interlayer could not determined but it can be expected that a continuously graded interlayer with a smoother transition between W and Cu results in a better adaptation of CTE. None of the interface concepts had an influence on the tensile strength of the fiber. All interface concepts are easily realized by magnetron sputter deposition.

Microstructuring concepts

For further application of the microstructured fibers, a balance must be found between interfacial adhesion, fiber strength and technical feasibility. Tensile tests demonstrated that the surface modifications of all six different microstructuring concepts weakened the UTS of the fibers. The reduction ranged from 8% to 42%. However, single fiber pull-out tests showed that a general increase in interfacial shear strength was achieved by the microstructuring concepts with the exception of ion sputtering.

Fiber twisting to 30° ±4° was found to achieve the highest interfacial shear strength, with a three fold increase in strength. On the other hand, the tensile strength was

reduced by 32 %. In addition, the twisting process is relatively complex in laboratory scale and very time consuming. The twisting of the required large amount of fibers for the implementation into the mock-up can only be realized through a large effort. Therefore, all concepts including the twisting were evaluated as not easily feasible.

Chemical etching showed an increase of interfacial shear strength by a factor of 1.5 and reduced the tensile strength only by 15%. Chemical etching can be easily realized. Therefore, the tensile strength and feasibility criterion were the convincing arguments here.

7.2 Choice of optimal concepts

Chemical etching (interface concept II) was chosen to be the optimal microstructuring concept to be applied on the fibers for an enhanced mechanical interlocking. Furthermore, it was decided to choose the continuously graded W/Cu coatings plus subsequent heat treatment at 800℃ (interface concept E) as the optimal interface concept for improved adhesion and adaptation of the thermal mismatch. The microstructured and coated fibers were used for further application in the monoblock mock-up.

Future industrial realization

The realization of the optimization concepts on industrial scale is feasible. The promising microstructuring concepts like chemical etching are practical. Even the realization of helical grooves on top of the W fibers for enhanced mechanical interlocking might be feasible by already incorporating a twisting of the fiber in the manufacturing process.

The technology for continuous fiber coating by magnetron sputter deposition at industrial scale has already been developed by EADS and is an industrially applicable technique for applying the graded W/Cu coating on W fibers as an interface concept. The continuous microstructured and coated fibers can be further wound to achieve circumferential, helical and polar winding as reinforcement according to the desired mechanical properties [153].

Chapter 8

Proof of Principle - Evaluation of optimized monoblock mock-up

8.1 Monoblock mock-up with optimized W_f/Cu MMC

Based on the results from lab experiments a novel advanced W_f/Cu MMC was developed and validated for its used as an efficient high heat sink material for water-cooled divertors in future fusion reactors. Interface concept E (continuously graded W/Cu_{PVD} interlayer + 800°C heat treatment) and microstructuring concept II (chemical etching) were chosen to enhance the adhesion between fibers and matrix. The next step was to demonstrate the feasibility of implementing the novel W_f/Cu MMC in a monoblock mock-up and to analyze and validate the performance of the component under high heat fluxes. The MMC was used to reinforce the interface between the PFM and the cooling channel in the monoblock mock-up. Figure 8.1 a) shows one finalized monoblock mock-up after the synthesis processes. Figure 8.1 b) presents the experimental set-up of the monoblock mock-up within the GLADIS vacuum chamber. The cooling tube of the monoblock was clamped to the water cooling supply. The two scrapers were positioned to limit the beam on the W tiles of the monoblock. The thermocouples were installed in the shadow of the component to prevent them from direct contact with the beam.

8.2 Finite Element Analysis

Thermal 2D FEA was performed to estimate the expected temperature at the W tile surface (T-smax), at the thermocouples (T-tc) (placed 2.5 mm under the plasma-facing surface in each W tile), of the W_f/Cu MMC (T-MMC), of the CuCr1Zr cooling tube
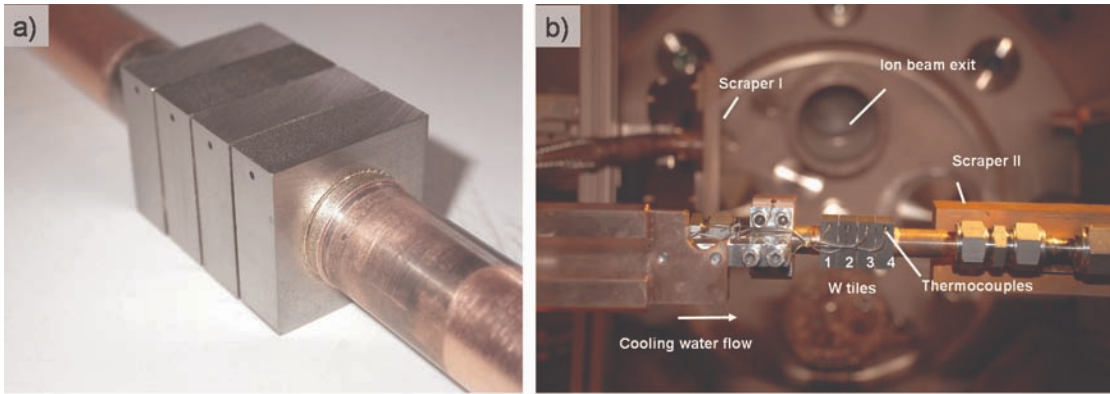
Figure 8.1: *a) Finalized optimized monoblock mock-up after the syntheses processes*
              b) Experimental set-up of the monoblock mock-up within the GLADIS vacuum chamber

(T-CuCrZr) and at the internal tube wall (T-wi).

As an example, the temperature evolution as a function of time within the monoblock at a heat flux of 15 MW/m² is shown in Figure 8.2 a). The temperature decreases with decreasing distance to the cooling channel. After 10 seconds, all temperatures reach a steady state.

Figure 8.2 b) presents the calculated steady state temperature at dedicated heat fluxes between 1 and 20 MW/m² which serves as basis for comparison with the experimental temperature data. In general, the temperature of T-smax and T-tc increased almost linearly with increasing heat fluxes. The temperature evolution of T-MMC, T-CuCrZr and T-wi indicate at 5 MW/m² a decrease of the slope of the temperature resulting in a smaller temperature increase at higher heat fluxes than at the surface and at the thermocouples.

At heat fluxes higher than 15 MW/m² the CuCr1Zr cooling tube has to withstand temperatures higher than 438°C. The calculated temperatures in 2D are similar to those predicted by the simulation in 3D by You [12]. However, these temperatures are in the range of the operation temperature limit of the CuCr1Zr material and would lead to loss of its precipitation hardening. Therefore, a thicker reinforcement or a complete replacement of the CuCr1Zr tube by the W$_f$/Cu MMC should be used for the future monoblock developments to reduce the thermo-mechanical stress.

Figure 8.3 presents the temperature distribution of the half cross-section of the monoblock mock-up. The edges of the W tiles are clearly the highest temperature loaded area since these are farthest away from the cooling channel. Additionally, it can be seen that the temperature of the lower half of the W tile does not significantly change. Thus, this part does not contribute significantly to the cooling of the component.
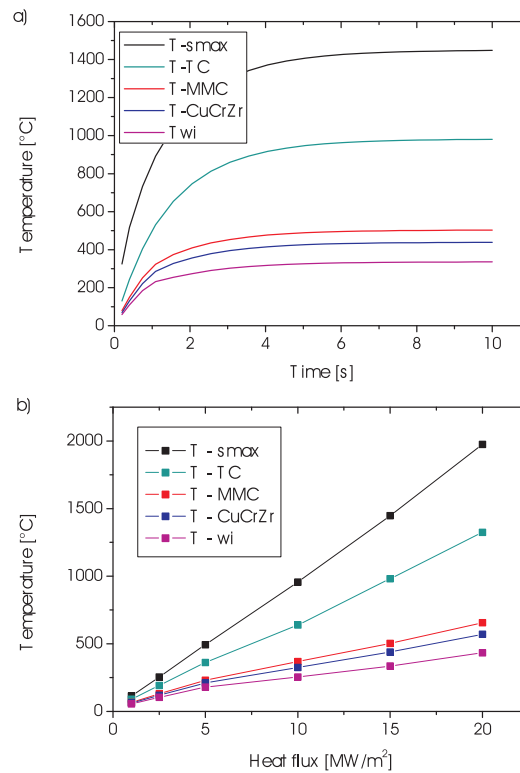
Figure 8.2: *a) Temperature evolution as function of time within the monoblock at a heat flux of 15 MW/m^2*
b) Expected temperatures of the W/Cu monoblock mock-up at the W surface, at the thermocouple, at the MMC, at the CuCr1Zr cooling tube and at the internal colling tube wall in dependence of different heat fluxes calculated by FEA
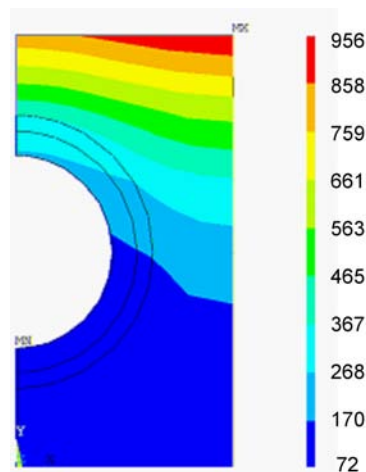
Figure 8.3: *Temperature distribution plot of the half cross-section of the monoblock mock-up at a heat flux of 10 MW/m^2. The figure shows the graphical representation of the temperature values of each element within the structure.*

8.3   Temperature analysis of the heat-loaded monoblock

Screening tests with increasing power density, starting from 0.2 to 10.5 MW/m^2, were applied to determine the performance of the monoblock mock-ups under heat load. The results of the first monoblock are presented in detail in the following two chapters.

The temperature evolution with increasing heat flux load at the W tile surface and at the thermocouples of each tile is shown in Figure 8.4. In general, the surface temperature and the bulk temperature of the mock-up increase with the applied heat flux. The temperature data and the optical investigation by CCD camera of the first (W tile #1) and the last (W tile #4) W tile show an overheating of the W tile starting already at low heat fluxes. It appears that the tiles were not correctly bonded to the MMC resulting in insufficient cooling of the tiles.

In contrast, the two middle W tiles (W tile #2 and #3) were nicely bonded and their temperature at different heat fluxes followed the expected temperature predicted by FEA. At higher heat fluxes, 7 MW/m^2, the temperature of W tile #2 slightly differs from the temperature of W tile #3 indicating some cooling problems. Possible explanation is the debonding at one or more of the interfaces or the influence of the overheated neighbor W tile. Therefore, solely W tile #3 was perfectly actively cooled until 10.5 MW/m^2. Microscopic investigation of the cross sections gave more information about the failure mechanism leading to a better understanding (see next chapter 8.4).

The thermocouples reached their limit (1080°C) at the heat flux of 10.5 MW/m^2, thus, no measurements were possible for higher heat fluxes. The temperatures determined by the one-color pyrometer (spot size of d = 6mm) and two-color pyrometer (spot size of d = 18 mm) were measured on W tile #2 but follow and continue the linear temperature evolution of the thermo couple measurements of W tile #1 and #4. Therefore, it can be assumed that the measured temperature values correlated to the temperatures of the overheated and not cooled W tiles.

Figure 8.5 presents the infrared camera images at heat flux pulses of 0.2, 0.5, 1, 2, 8 and 10.5 MW/m^2, respectively, identifying the hot spots on the monoblock. W tile #1 and W tile #4 show an overheating starting at low heat fluxes of 1 MW/m^2. The images indicates temperature peaks at the upper edge of the W tiles which correlates to the FEA predicted maximum thermally loaded spots. The lower edge should also indicate a temperature peak. The position of the infrared camera or a slight tilt angle of the monoblock regarding the beam plane are possible reasons for this asymmetrical behavior.

Regarding the temperature measurement methods, some concluding remarks should
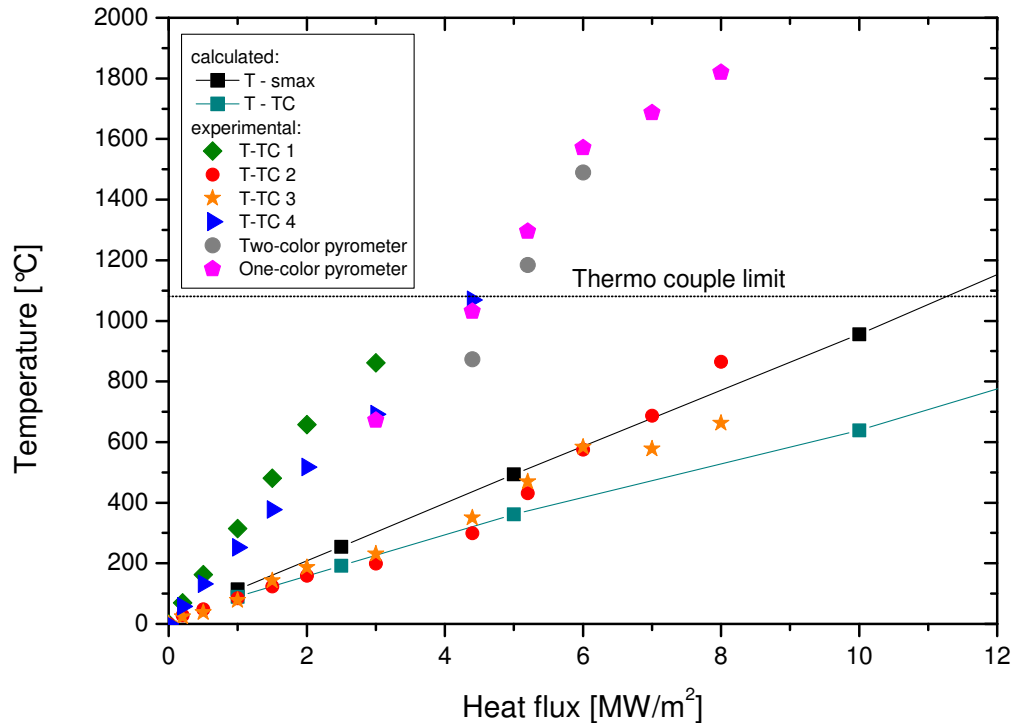
Figure 8.4: *Experimental measured temperatures of infrared camera, pyrometer and installed thermo couples within the W tiles #1 - #4 of the W_f/Cu monoblock mock-up in dependence of different heat fluxes compared with the calculated surface and thermo couple temperature data by FEA*

be taken into consideration: A sensitive parameter for one-color pyrometer and infrared measurement is the emissivity factor ϵ which depends on the surface of the W tiles, on the temperature and detection wave length λ. Variations of the emissivity of ± 0.02 correspond to temperature variations of $\pm 400°C$. Therefore, it is difficult to compare the exact values of the optically measured temperatures, i.e., the values of the one-color pyrometer and infrared camera, with the calculated surface temperatures via FEA. The most reliable temperature measurements during the high heat flux tests were achieved by the thermo couples.
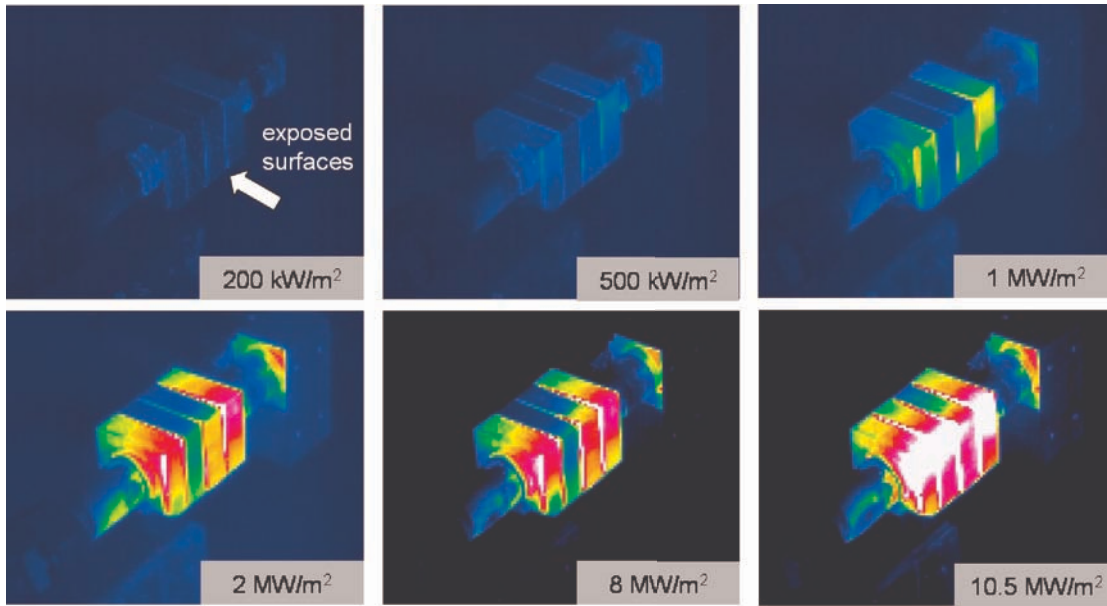
Figure 8.5: *Infrared camera images during heat flux pulses at different power densities, identifying the hot spots on the monoblock and indicating the highest temperature load at the edges of the W tiles.*

8.4 Microscopic investigations

The first and the last W tile (W tiles #1 and #4) already showed gaps at the interface between PFM and MMC structure before heat flux testing which indicates imperfections in the joining process. As the bonding technology between W and CuCr1Zr is considered as well established technology, no failure was expected. The novelty in the brazing process was to incorporate the MMC within the W tiles instead of the pure CuCr1Zr tube. From a chemical point of view, all the materials are well known and no problems should arise unless materials are contaminated with impurities which can create problems. Therefore, a possible explanation for the difference between the bonded W tiles #2 and #3 and the insufficiently bonded tiles #1 and #4 could be impurities at the brazing interface due to handling mistakes.

Light microscopy and SEM investigations were performed on the mock-up after the high heat flux tests. No micro-cracks were observed on the exposed surfaces of the W tiles. The microstructure of the beam facing W half is dominated by coarse grains. The grain growth occurs due to the higher temperature. In contrast, the microstructure of the other W half is characterized by fine grains.

The cross-section analysis of each W tile of the mock-up was performed to check for diffusion, delamination and debonding of the monoblock components. Figure 8.6 shows EDX maps of the cross section of W tile #3 indicating that Ni diffused from the

GEMCO brazing foil into Cu while Ge diffused mainly into W.
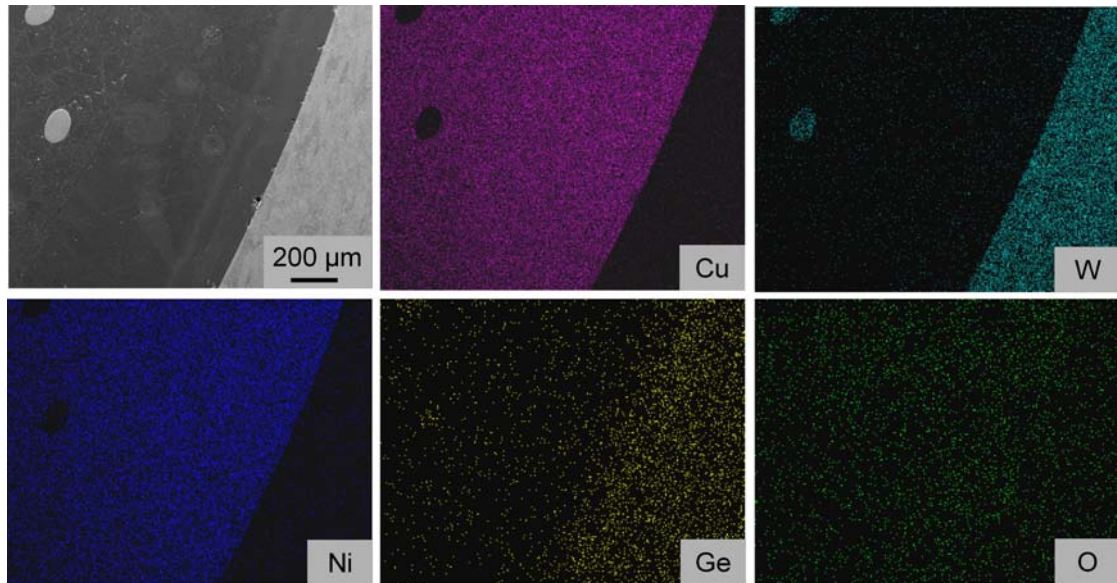
Figure 8.6: *EDX maps of the cross section of W tile #3 indicating diffusion of Ni and Ge from GEMCO brazing foil into Cu and W, respectively*

W tile #3 survived 10.5 MW/m^2 without any visible damage of the compound. Figures 8.7 a) and b) present the cross sections of W tile #4 and #2. The cross sections of #4 indicate large gap formation between PFM, GEMCO brazing foil and MMC as it was already expected from the result of the temperature analysis. The cross sections of W tile #2 and #3 look similar. Both show mainly bonded zones between PFM and brazing foil.

The focus of the high heat flux test was to investigate the performance of the novel optimized W$_f$/Cu MMC implemented in the monoblock mock-up. The cross section of the interface between W fiber and Cu matrix of the MMC in W tile #3 (SEM Figure 8.7 c)) clearly shows that the fiber was well embedded like most of the fibers in the Cu matrix without any debonding. Possible cracks between fiber and matrix may result from the polishing process of the cross section. The magnification of Figures 8.7 a) and b) show that no gap between MMC and CuCr1Zr tube was visible, thus, it can be concluded that the arrangement of the W fibers and the HIP process at the reinforced region lead to a complete consolidation. The synthesis method can be applied to implement W$_f$/Cu MMC as reinforcement or eventually as replacement of CuCr1Zr material for the cooling tube. In this work four uni directional layers were implemented due to the time consuming manual work. In principle, the number of fiber layers allows to tailor the fiber volume fraction and can be freely adjusted to obtain the required mechanical properties.
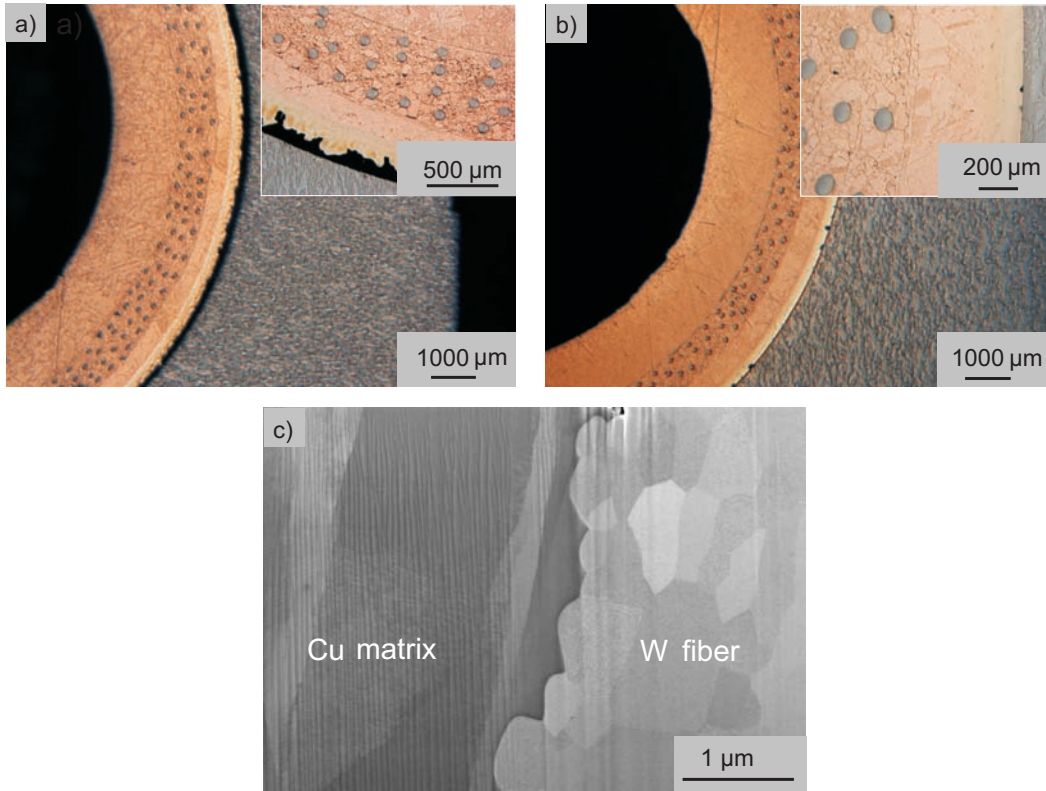
Figure 8.7: *Cross section of W tiles of the monoblock mock-up after heat flux test a) Cross section of W tile #4 demonstrate the gap between tube and PFM while b) W tile #2 indicates a good bonding between tube and PFM c) Cross section of the interface between W fiber and Cu matrix of the MMC in W tile #3 indicating that the fiber is well embedded*

Incomplete consolidation of the joints leads to an interruption of the thermal heat transport resulting in an overheating of the not bonded structure. This effect occurred at the end of the cooling tube where the HIP Cu capsule was not completely bonded to the CuCr1Zr tube (see Figure 8.8 a)). The cross section of the cooling tube shows that the outer Cu capsule was overheated and began to deform plastically due to melting. The microstructure of the Cu capsular is dominated by coarse grains due to recrystallization (see Figure 8.8 b)). In contrast, the microstructure of the CuCr1Zr tube is characterized by fine grains which may originate from the precipitation. The surface melting was already detected in-situ by the CCD camera and led to the termination of the heat flux test at 10.5 MW/m^2 to avoid possible water loss of the cooling channel.
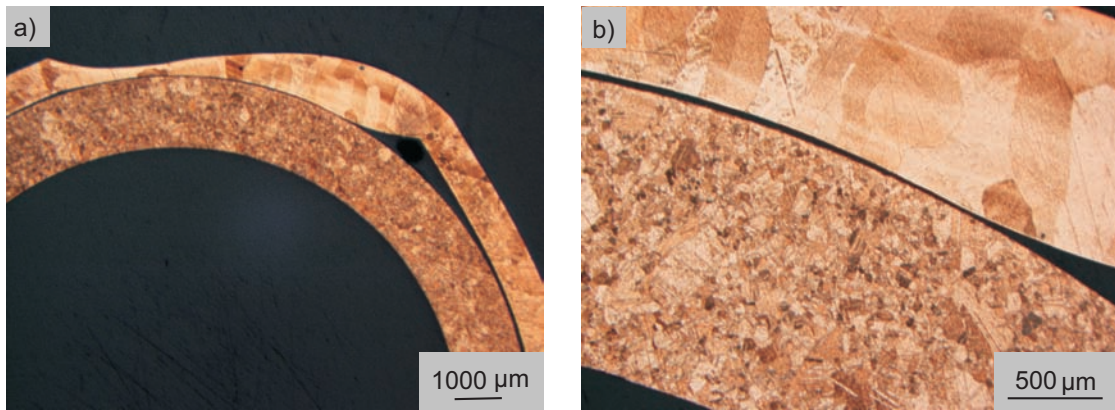
Figure 8.8: *Local surface melting of the cooling tube as a result of incomplete consolidation process of the CuCr1Zr tube and the Cu capsular*

8.5 Cyclic test of optimized monoblock mock-up

The second monoblock mock-up was tested under high heat fluxes analog to the first monoblock mock-up. The same screening tests (chapter 4.5) were performed. The results of the first monoblock mock-up could be confirmed. One W tile showed an optimal stable thermal behavior at heat fluxes of up to 10.5 MW/m². Subsequently, the beam exposed surface was limited by one movable scraper to the surface of the stable W tile. The pyrometers and infrared camera were positioned on this W tile. The W tile was cyclically loaded with a heat flux of 10.5 MW/m². With each cycle the surface temperature increased slightly indicating a degradation of the W tile cooling. After 25 cycles the variation of temperature was ≈400°C. It can be assumed that during each cycle the bond between PFM and MMC degenerates as this joint is the weak point of the component.

8.6 Summary evaluation of optimized monoblock mock-up

FEM simulation predict the expected temperature within the monoblock mock-up allowing to design and understand the thermal behavior of the component under high heat flux test. The predicted temperature peak at the upper W tile edges was verified during the heat flux experiments.

The temperature data and optical investigation of the first monoblock mock-up indicated two overheated W tiles due to their incomplete bonding due to faulty brazing to the MMC. The other two W tiles showed a temperature behavior as predicted by

FEA. At the highest heat flux of 10.5 MW/m^2 W tile #3 remained bonded and showed an optimal stable thermal behavior. The second monoblock mock-up could confirm the achieved results and showed unstable thermal behavior after 25 cycles at 10.5 MW/m^2.

Microscopic investigation of the cross sections of each W tile gave more information about the failure mechanism like insufficient bonding due to improper handling of W tile #1 and #4 prior to brazing. Furthermore, the light microscopy images show that the implementation of the novel W$_f$/Cu MMC was successful and no consolidation problems occurred. The fibers remained stably embedded in the matrix.

It can be concluded that the weak point of the monoblock mock-ups was the bonding technology between W and W$_f$/Cu MMC.

Chapter 9

Conclusion

A novel W_f/Cu metal matrix composite was developed and validated for its application as an efficient high temperature heat sink material in water-cooled monoblock divertors for future fusion reactors like DEMO. The main focus of this work was the optimization of the interface between the W fibers and the Cu matrix to obtain better adhesion. Interdiffusion experiments showed that the interfacial adhesion of W and Cu is determined solely through mechanical interlocking at synthesis and operation temperatures of the W_f/Cu MMC. Therefore, effective interface optimization concepts were chosen to achieve a stable interface between the W fiber and the Cu matrix, thus allowing good mechanical properties of the MMC.

The interface between W fiber and Cu matrix was optimized by: 1) tailoring the nanoscopic interface by depositing different interlayers to achieve a form closure plus adhesive bond, and 2) by nano- and microstructuring of the fiber to improve the mechanical interlocking. Five different interface concepts and six different microstructuring concepts were tested to improve the interface between fiber and matrix. The PVD deposited interlayers were analyzed with respect to their thermal stability, i.e., changes of their nanostructure, composition, stress state and texture were analyzed after dedicated heat treatments according to synthesis and operation temperatures of the MMC. The morphology, strength and roughness of the microstructured fibers were characterized on several length scales. The interface and microstructuring concepts were mechanically tested by pull-out measurements to investigate their optimization effect on the interfacial adhesion between fiber and matrix. Chosen MMCs were investigated with respect to their oxygen content, thermal stability and the residual stress state of their fibers and matrix during thermal cycling. The optimal interface and microstructuring concept was determined and was unified in MMCs, processed in two monoblock mock-ups and tested under high heat fluxes.

In the following, the main results of this work are discussed.

Interface concepts

Five different interlayers were tested for the interface between the W fibers and the Cu matrix. The best result was achieved by applying thin 500 nm graded W/Cu coatings, stepwise and continuously, with subsequent heat treatment at 800°C. The interfacial shear strength, i.e, the interfacial adhesion between W and Cu could be improved by at least a factor of 6.

This results from significant changes in the nanostructure of the thin graded W/Cu coatings after annealing at 800°C: W/W grain boundary diffusion processes and Ostwald ripening of the nanometer-sized grains led to their interconnection between each other and the W substrate. In good agreement to the microscopic investigations, the phase, texture and stress analysis of graded W/Cu indicated grain growth, diffusion processes and changes in the nanostructure of pure W and Cu.

Microstructuring concepts

The second possibility to optimize the interface between W fiber and Cu matrix was by microstructuring the fiber surface to achieve enhanced adhesion. Six different nano- and microstructuring concepts were investigated. The resulting analysis showed that the surface has significant variations on the microscale length like smoothing effect due to ion sputtering, roughness increase due to chemical etching, and surface cracks due to twisting. Tensile tests demonstrated that the surface modifications weaken the UTS of the fibers. However, single fiber pull-out tests showed that a general increase in interfacial shear strength was achieved by the microstructuring concepts with the exception of ion sputtering. The microstructuring led to enlargement of the contact area on a micrometer scale resulting in good mechanical interlocking and interfacial adhesion between fiber and matrix. For further application of the microstructured fibers in the monoblock mock-up, a balance was found between interfacial adhesion, fiber strength and technical feasibility. Chemical etching was chosen to be the optimal concept to be applied on the fibers.

Improved W$_f$/Cu MMCs

Analysis of MMCs produced from the W fibers showed that the consolidation process does not incorporate more O and that the interfaces of W and Cu are mostly free of oxides.

Selected MMCs were thermally cycled between 350°C and 550°C according to its expected operation temperature. The tests showed that the thermal stability of the MMC can be ensured by depositing a stepwise graded transition between W fiber and Cu matrix. It can be concluded that supplementary to its positive effect on the interface adhesion the stepwise graded transition between W fiber and Cu matrix acts as a stepwise adaptation of CTE mismatch between W fiber and Cu matrix.

This functionality was quantitatively validated by in-situ stress measurements of ungraded and graded fiber reinforced MMCs. Residual stresses in the Cu matrix up to 200 MPa are built up during thermal cycling between RT and 550°C. Plastic deformation of the matrix (creep) is indicated by stress inversion after cooling due to matrix shrinkage. The W fibers compensate the compressive stresses of the matrix by tension according to their volume fraction. After two cycles, debonding between fiber and matrix was not detected. Clear differences in residual stress levels between the MMCs without interface and with continuously graded transition was observed. Thus, it can be concluded that the graded transition leads to stress reduction at the fiber/matrix interface.

Optimized monoblock mock-up

Based on the optimization results from lab experiments the continuously graded W/Cu$_{PVD}$ interlayer plus 800°C heat treatment and chemical etching of the fiber were chosen to enhance the adhesion between fiber and matrix. The novel advanced W$_f$/Cu MMC was implemented in monoblock mock-ups reinforcing the interface between the plasma facing material and the cooling channel. Its suitability as an efficient high heat sink material for water-cooled divertors in future fusion reactors was tested in the high heat flux facility GLADIS.

FEM simulations were performed to predict the temperature within the monoblock mock-up to understand the thermal behavior of the component under high heat fluxes. The experimental temperature data and optical investigation of the first mock-up indicated that two of four W tiles were optimally bonded. Their thermal behaviors showed good agreement with the predicted temperatures during the heat flux experiments. At the highest heat flux of 10.5 MW/m^2 one of these W tiles remained bonded and showed an optimal stable thermal behavior.

Furthermore, microscopic investigation showed that the implementation of the novel W$_f$/Cu MMC was successful and the synthesis method can be applied to implement W$_f$/Cu MMC as reinforcement or eventually as replacement of CuCr1Zr material for the cooling tube. The fibers remained stably embedded in the matrix under high heat

fluxes guaranteeing good performance of the whole component.

The second monoblock mock-up was able to confirm the achieved results of the first monoblock mock-up, but showed unstable thermal behavior after 25 cycles at 10.5 MW/m^2. It can be concluded that the weak point of the monoblock mock-up under heat flux tests was the bonding technology between W and W_f/Cu MMC.

Concluding remarks

Many technical application fields have to deal with similar problems of thermal management. High temperature becomes a limiting factor in construction not only of fusion reactors but also of heat exchangers, thruster chambers, brake systems, aircraft engine parts, etc. The need for new materials possessing high thermal conductivity, ability to withstand large temperature changes without loss or deterioration of properties, and capable of reducing complex thermo-mechanical stresses after bonding is always present.

In this work, novel advanced W_f/Cu composites were developed by tailoring of interfaces between W and Cu at micro- and nanoscopic levels in order to enhance its performance under extremely demanding environments. The next step would be to transfer the generated knowledge to industrialization. The commercial realization of promising microstructuring concepts like chemical etching is practical. Even the realization of helical grooves on top of the W fibers for enhanced mechanical interlocking might be feasible by incorporating a twisting of the fiber already in the manufacturing process.

The technology for continuous fiber coating by magnetron sputter deposition at industrial scale was already developed by EADS and is an industrially applicable technique for applying the graded W/Cu coating on W fibers as an interface concept. The continuous microstructured and coated fibers can be further wound to achieve circumferential, helical and polar winding as reinforcement according to the desired mechanical properties.

The satisfying development, characterization, implementation and mechanical testing of the W_f/Cu MMC in monoblock mock-up demonstrates that the manufacturing of an MMC optimized divertor for fusion application is definitely challenging but feasible.

Chapter 10

List of publications, talks and posters

10.1 Publications

1. A. Herrmann, C. Boswell, M. Balden, K. Schmid and H. Bolt. *Microstructuring of tungsten fiber for enhanced interfacial adhesion in copper.* Materials Science and Engineering A, (2008) prepared to submit.

2. A. Herrmann, M. Rasinski, M. Balden and H. Bolt. *Adhesion, stress state, phase and morphology analysis of thin graded W/Cu coatings on tungsten and their thermal behaviour in fusion application.* Advanced Materials Research, (2008) in revision.

3. A. Herrmann, K. Schmid, M. Balden and H. Bolt. *Interfacial optimization of tungsten fiber reinforced copper for high-temperature heat sink material for fusion application.* Journal of Nuclear Materials, (2008), accepted.

4. A. Herrmann, A. Brendel, M. Balden and H. Bolt. *Metal Matrix Composite used as high-temperature heat sink material for future fusion reactors.* JEC Composite Magazine, 33, 67-70 (2007).

5. F. Kost, C. Linsmeier, M. Oberkofler, M. Reinelt, M. Balden, A. Herrmann and S. Lindig. *Investigation of chemical phase formation in the ternary system beryllium, carbon and tungsten with depth-resolved photoemission spectroscopy.* Journal of Nuclear Materials, (2008), in revision.

6. T. Köck, A. Herrmann, A. Brendel, and H. Bolt. *Influence of different deposition parameters on the performance of a Ti-Ta-C interface layer in silicon carbide-copper metal-matrix composites.* Advanced Materials Research, (2008) in revision.

7. C. Adelhelm, M. Balden, F. Kost, A. Herrmann, S. Lindig. *Thermal induced structural changes of a-C and a-C:Ti films analyzed by NEXAFS and XPS*. Journal of Physics: Conference Series, 100, (2008)

8. M. Balden, C. Adelhelm, T. Köck, A. Herrmann, J. Jaimerena-Muga. *Thermal nanostructuring of metal-containing carbon films and their nanoindentation testing*, Reviews on Advanced Materials Science, 15(2):95-104, (2007)

10.2 Oral conference presentations

1. A. Herrmann, C. Linsmeier and H. Bolt. *ExtreMat – Challenges in Materials Research and Integrated Solutions at European Level.* European Training Network for Plasma Fusion Materials (ETN-PFM) meeting, 2008-06-09 to 2008-06-11, Cadarache.

2. A. Herrmann, M. Rasinski, M. Balden and H. Bolt. *Adhesion, stress state and phase analysis of thin graded W/Cu coatings on tungsten and their thermal behaviour in fusion application.* 1st International Conference on New Materials for Extreme Environments, 2008-06-02 to 2008-06-04, San Sebastian.

3. A. Herrmann. *Interfacial Optimization of Tungsten Fibre-Reinforced Copper for High Temperature Heat Sink Material for Fusion Application.* DGM - Fachausschuss „Metallische Verbundwerkstoffe und zellulare Metalle", 2007-11-06, Garching

4. A. Herrmann, M. Balden and H. Bolt. *Tungsten fiber reinforced copper for high-temperature heat sink material for fusion application.* 16. Symposium: Verbundwerkstoffe und Werkstoffverbunde, DGM, 2007-03-14 to 2007-03-16, Bremen.

5. M. Schöbel, H.P. Degischer, T. Buslaps, M. di Michiel, T. Poeste, R. Schneider, S. Kleiner, J. Hemptenmacher, A. Herrmann. *Residual stresses in metal matrix composites for heat sink applications during thermal cycling.* 8th International Conference on Residual Stresses, 2008-08-04 to 2008-08-08, Denver.

6. A. Brendel, V. Paffenholz, T. Köck and A. Herrmann. *Faserverstärktes Kupfer für Bauteile in Fusionsreaktoren.* 14. Nationales Symposium SAMPE Deutschland e.V. "Fasern und Matrix", 2008-02-27 to 2008-02-28, Technische Universität München, Garching.

10.3 Poster presentations

1. A. Herrmann, C. Boswell, M. Balden, K. Schmid and H. Bolt. *Coating and microstructuring of tungsten fibers for its enhanced interfacial adhesion in copper for high-temperature heat sink material.* E-MRS 2008 Spring Meeting, 2008-05-26 to 2008-05-30, Strasbourg.

2. A. Herrmann, K. Schmid, M. Balden and H. Bolt. *Interfacial optimization of tungsten fiber reinforced copper for high-temperature heat sink material for fusion application.* 13thInternational Conference on Fusion Reactor Materials (ICFRM-13), 2007-12-10 to 2007-12-14, Nice.

3. A. Herrmann, M. Balden, A. Brendel and H. Bolt. *Interfacial characterisation of tungsten fiber reinforced copper for high-temperature heat sink material for fusion application.* European Congress and Exhibition on Advanced Materials and Processes (EUROMAT 2007), 2007-09-10 to 2007-09-13, Nürnberg.

List of Figures

List of Tables

Bibliography

[1] ITER Technical Basis. Technical report, International Atomic Energy Agency, 2002.

[2] U. Schumacher. Status and problems of fusion reactor development. *Naturwissenschaften*, 88(3):102–112, 2001.

[3] M. Merola, W. Dänner, J. Palmer, G. Vielder, and C. H. Wu. European contribution to the development of the ITER divertor. *Fusion Engineering and Design*, 66-68:211–217, 2003.

[4] K. Ehrlich. Materials research towards a fusion reactor. *Fusion Engineering and Design*, 56-7:71–82, 2001.

[5] S. J. Zinkle and N. M. Ghoniem. Operating temperature windows for fusion reactor structural materials. *Fusion Engineering and Design*, 51-52:55–71, 2000.

[6] A. S. Kukushkin, H. D. Pacher, G. Federici, G. Janeschitz, A. Loarte, and G. W. Pacher. Divertor issues on iter and extrapolation to reactors. *Fusion Engineering and Design*, 65(3):355–366, 2003.

[7] D. Maisonnier. Plant models for DEMO. In *Burning Plasma Diagnostics*, volume 988 of *Aip Conference Proceedings*, pages 52–59. 2008.

[8] et al. D.Maisonnier. EFDA Final Report of the European Fusion Power Plant Conceptual Study (PPCS). Technical report, EFDA, 2004.

[9] ITER Materials Assessment Report. Technical report, ITER Doc. G74 MA 1001-07011 W 0.2, 2001.

[10] J. Schlosser, F. Escourbiac, M. Merola, S. Fouquet, P. Bayetti, J. J. Cordier, A. Grosman, M. Missirlian, R. Tivey, and M. Rodig. Technologies for ITER divertor vertical target plasma facing components. *Nuclear Fusion*, 45(6):512–518, 2005.

[11] J. Linke. High heat flux performance of plasma facing materials and components under service conditions in future fusion reactors. *Fusion Science and Technology*, 53(2T):278–287, 2008.

[12] J.H. You. Design feasibility study of a divertor component reinforced with fibrous metal matrix composite laminate. *Journal of Nuclear Materials*, 336(1):97–109, 2005.

[13] J.H. You and H. Bolt. Structural analysis of a plasma facing component reinforced with fibrous metal matrix composite laminate. *Journal of Nuclear Materials*, 329-333(Part 1):702–705, 2004.

[14] H. Bolt, V. Barabash, W. Krauss, J. Linke, R. Neu, S. Suzuki, N. Yoshida, and ASDEX Upgrade Team. Materials for the plasma-facing components of fusion reactors. *Journal of Nuclear Materials*, 329-333(Part 1):66–73, 2004.

[15] H. Bolt, V. Barabash, G. Federici, J. Linke, A. Loarte, J. Roth, and K. Sato. Plasma facing and high heat flux materials - needs for ITER and beyond. *Journal of Nuclear Materials*, 307:43–52, 2002.

[16] F.L. Chong, J.L. Chen, and J.G. Li. Evaluation of tungsten coatings on Cu-CrZr and W/Cu FGM under high heat flux and HT-7 limiter plasma irradiation. *Journal of Nuclear Materials*, 363-365:1201–1205, 2007.

[17] W.P. Shen, Q. Li, K. Chang, Z.J. Zhou, and C.C Ge. Manufacturing and testing W/Cu functionally graded material mock-ups for plasma facing components. *Journal of Nuclear Materials*, 367-370(Part 2):1449–1452, 2007.

[18] G. Pintsuk, S. E. Brünings, J. E. Döring, J. Linke, I. Smid, and L. Xue. Development of W/Cu-functionally graded materials. *Fusion Engineering and Design*, 66-68:237–240, 2003.

[19] C.C. Ge, J.-T. Li, Z.-J. Zhou, W.-B. Cao, W.-P. Shen, M.-X. Wang, N.-M. Zhang, X. Liu, and Z.-Y. Xu. Development of functionally graded plasma-facing materials. *Journal of Nuclear Materials*, 283-287(Part 2):1116–1120, 2000.

[20] R. Jedamzik, A. Neubrand, and J. Rodel. Functionally graded materials by electrochemical processing and infiltration: Application to tungsten/copper composites. *Journal of Materials Science*, 35(2):477–486, 2000.

[21] Y. Itoh, M. Takahashi, and H. Takano. Design of tungsten/copper graded composite for high heat flux components. *Fusion Engineering and Design*, 31(4):279–289, 1996.

[22] J. W. Davis, K. T. Slattery, D. E. Driemeyer, and M. A. Ulrickson. Use of tungsten coating on iter plasma facing components. *Journal of Nuclear Materials*, 233-237(Part 1):604–608, 1996.

[23] D. M. Mattox. Surface effects on the growth, adhesion and properties of reactively deposited hard coatings. *Surface and Coatings Technology*, 81(1):8–16, 1996.

[24] Fr.-W. Bach, A. Laarmann, and T. Wenz, editors. *Fundamentals of thin-film Technology*. Modern Surface technology. Wiley-VCH, Winheim, 2006.

[25] M. Ohring. *The materials science of thin films*. Academic press, 1992.

[26] R. Behrisch and W. Eckstein, editors. *Sputtering by Particle Bombardment - Experiments and Computer Calculations from Threshold to MeV Energies*, volume 110 of *Topics in Applied Physics*. Springer, Berlin, 2007.

[27] D. M. Mattox. Particle Bombardment Effects on Thin-Film Deposition - a Review. *Journal of Vacuum Science and Technology A - Vacuum Surfaces and Films*, 7(3):1105–1114, 1989.

[28] J. Mahan. *Physical vapor deposition of thin films*. John Wiley and Sons, 2000.

[29] J. Cho, S.G. Terry, R. LeSar, and C.G. Levi. A kinetic monte carlo simulation of film growth by physical vapor deposition on rotating substrates. *Materials Science and Engineering A*, 391(1-2):390–401, 2005.

[30] H. J. Gao and W. D. Nix. Surface roughening of heteroepitaxial thin films. *Annual Review of Materials Science*, 29:173–209, 1999.

[31] P. B. Barna and M. Adamik. Fundamental structure forming phenomena of polycrystalline films and the structure zone models. *Thin Solid Films*, 317(1-2):27–33, 1998.

[32] I. Petrov, P. B. Barna, L. Hultman, and J. E. Greene. Microstructural evolution during film growth. *Journal of Vacuum Science and Technology A*, 21(5):117–128, 2003.

[33] B. A. Movchan and Demchish.Av. Study of Structure and Properties of Thick Vacuum Condensates of Nickel, Titanium, Tungsten, Aluminium Oxide and Zirconium Dioxide. *Physics of Metals and Metallography-Ussr*, 28(4):83, 1969.

[34] J. A. Thornton and D. W. Hoffman. Stress-Related Effects in Thin-Films. *Thin Solid Films*, 171(1):5–31, 1989.

[35] R. Messier, A. P. Giri, and R. A. Roy. Revised Structure Zone Model for Thin - Film Physical Structure. *Journal of Vacuum Science and Technology A - Vacuum Surfaces and Films*, 2(2):500–503, 1984.

[36] H. Windischmann. Intrinsic Stress in Sputter-Deposited Thin-Films. *Critical Reviews in Solid State and Materials Sciences*, 17(6):547–596, 1992.

[37] H. Windischmann. Intrinsic Stress in Sputtered Thin-Films. *Journal of Vacuum Science and Technology A - Vacuum Surfaces and Films*, 9(4):2431–2436, 1991.

[38] R. Abermann. Measurements of the intrinsic stress in thin metal films. *Vacuum*, 41(4-6):1279–1282, 1990.

[39] H. Zhang and D. Y. Li. Effects of sputtering condition on tribological properties of tungsten coatings. *Wear*, 255(7-12):924–932, 2003.

[40] K. Robbie and M. J. Brett. Sculptured thin films and glancing angle deposition: Growth mechanics and applications. *Journal of Vacuum Science and Technology A - Vacuum Surfaces and Films*, 15(3):1460–1465, 1997.

[41] R. Messier, P. Sunal, and V. Venugopal. Evolution of sculptured thin films. *Engineered Nanostructural Films and Materials*, 3790:133–141, 1999.

[42] R. Messier and A. Lakhtakia. Sculptured thin films - Experiments and applications. *Materials Research Innovations*, 2(4):217–222, 1999.

[43] G.G Stoney. The Tension of Metallic Films Deposited by Electrolysis. *Proceedings of the Royal Society of London. Series A*, 82:172–175, 1909.

[44] R. W. Hoffman. Stresses in thin films: The relevance of grain boundaries and impurities. *Thin Solid Films*, 34(2):185–190, 1976.

[45] J. C. Bravman, W.D. Nix, D.M. Barnett, and D.A. Smith, editors. *Thin films: Stresses and Mechanical Properties*, volume 130 of *Thin films: Stresses and Mechanical Properties Symposium*. Material Research Society, 1989.

[46] R. Koch. The Intrinsic Stress of Polycrystalline and Epitaxial Thin Metal-Films. *Journal of Physics-Condensed Matter*, 6(45):9519–9550, 1994.

[47] F. Spaepen. Interfaces and stresses in thin films. *Acta Materialia*, 48(1):31–42, 2000.

[48] G. Janssen. Stress and strain in polycrystalline thin films. *Thin Solid Films*, 515(17):6654–6664, 2007.

[49] L. Spiess, R. Schwarzer, H. Behnken, and G. Teichert. *Moderne Röntgenbeugung - Röntgendiffraktometrie für Materialwissenschaftler, Physiker und Chemiker*. Teubner, Wiesbaden, 2005.

[50] M. Murakami. Deformation in Thin-Films by Thermal Strain. *Journal of Vacuum Science and Technology A - Vacuum Surfaces and Films*, 9(4):2469–2476, 1991.

[51] A. Brenner and S. Senderoff. Calculation of Stress in Electrodeposits from the Curvature of a Plated Strip. *Journal of Research of the National Bureau of Standards*, 42(2):105–123, 1949.

[52] M. Pletea, W. Brückner, H. Wendrock, and R. Kaltofen. Stress evolution during and after sputter deposition of Cu thin films onto Si(100)substrates under various sputtering pressures. *Journal of Applied Physics*, 97, 2005.

[53] C. Fitz, W. Fukarek, A. Kolitsch, and W. Moller. An instrument for in-situ stress measurement in thin films during growth. *Surface and Coatings Technology*, 128-129:474–478, 2000.

[54] M. Cremona, L. M. Gazola, L. C. Scavarda do Carmo, J. T. P. Castro, and C. A. Achete. In situ hard coatings strain measurement using a commercial strain-gage device. *Thin Solid Films*, 377-378:436–440, 2000.

[55] M. Mildner. *Komplexe Röntgendiffraktometrie an Dünnschichtsystemen*. PhD thesis, Technische Universität Chemnitz, 2005.

[56] U. Welzel, J. Ligot, P. Lamparter, A. C. Vermeulen, and E. J. Mittemeijer. Stress analysis of polycrystalline thin films and surface regions by X-ray diffraction. *Journal of Applied Crystallography*, 38:1–29, 2005.

[57] ASM International. Binary Alloy Phase Diagrams.

[58] T. B. Massalski. *Binary Alloy Phase Diagrams*. ASM International, Materials Park, OH, 1996.

[59] M. Hansen and K. Anderko. *Constitution of binary alloys*. second edition, 1958.

[60] A. P. Prevarskiy and Y. B. Kuzma. Phase-Equilibria and Crystal-Structures of Compounds in the W-Cu-Al System. *Russian Metallurgy*, (5):187–189, 1983.

[61] Y. V. Efimov, T. M. Frolova, O. I. Bodak, and O. I. Kharchenko. The W-WSi2-Cu System. *Inorganic Materials*, 20(9):1374–1376, 1984.

[62] M. Nastasi, F. W. Saris, L. S. Hung, and J. W. Mayer. Stability of Amorphous Cu/Ta and Cu/W Alloys. *Journal of Applied Physics*, 58(8):3052–3058, 1985.

[63] R. J. Kerans and T. A. Parthasarathy. Theoretical-Analysis of the Fiber Pullout and Pushout Tests. *Journal of the American Ceramic Society*, 74(7):1585–1596, 1991.

[64] D. Jihong, L. Zhengxiang, L. Gaojian, Z. Hui, and H. Chunliang. Surface characterization of CVD tungsten coating on molybdenum substrate. *Surface and Coatings Technology*, 198(1-3):169–172, 2005.

[65] S.J. Bull and E.G. Berasetegui. An overview of the potential of quantitative coating adhesion measurement by scratch testing - 180 Years of Scratch Testing. *Tribology International*, 39(2):99–114, 2006.

[66] S. Zhang, D. Sun, Y. Fu, and H. Du. Toughness measurement of thin films: a critical review. *Surface and Coatings Technology*, 198(1-3):74–84, 2005.

[67] M. D. Kriese, W. W. Gerberich, and N. R. Moody. Quantitative adhesion measures of multilayer films: Part I. Indentation mechanics. *Materials Research*, 14(7):3007–3018, 1999.

[68] D. B. Marshall and A. G. Evans. Measurement of Adherence of Residually Stressed Thin-Films by Indentation - Mechanics of Interface Delamination. *Journal of Applied Physics*, 56(10):2632–2638, 1984.

[69] E. Neubauer, G. Korb, C. Eisenmenger-Sittner, H. Bangert, S. Chotikaprakhan, D. Dietzel, A. M. Mansanares, and B. K. Bein. The influence of mechanical adhesion of copper coatings on carbon surfaces on the interfacial thermal contact resistance. *Thin Solid Films*, 433(1-2):160–165, 2003.

[70] J. Valli. A Review of Adhesion Test Methods for Thin Hard Coatings. *Journal of Vacuum Science and Technology A - Vacuum Surfaces and Films*, 4(6):3007–3014, 1986.

[71] J.-K. Kim and Y.-W. Mai. Interfaces in Composites. In R. Cahn, P. Haasen, and E. Kramer, editors, *Materials Science and Technology - Structure and Properties of Composited*, volume 13. VCH, Weinheim, 1993.

[72] C.-H. Hsueh. Interfaceial debonding and fiber pull-out stresses of fiber-reinforced composites. *Material Science and Engineering A*, pages 125–132, 1992.

[73] J. K. Kim and Y. W. Mai. High-Strength, High Fracture-Toughness Fiber Composites with Interface Control - Review. *Composites Science and Technology*, 41(4):333–378, 1991.

[74] K. Chawla. *Composite Materials - Science and Engineering.* Springer, New York,NY, 2nd edition, 1998.

[75] D. McDanels. Tungsten Fiber Reinforced Copper Matrix Composites - A review. *NASA Technical paper*, 2924, 1989.

[76] D. W. Petrasek and J. W. Weeton. Effects of Alloying on Room-Temperature Tensile Properties of Tungsten-Fiber-Reinforced-Copper-Alloy Composites. *Transactions of the Metallurgical Society of Aime*, 230(5):977, 1964.

[77] M.H. Meetham, G.W.; Van de Voorde. *Materials for High Temperature Engineering Applications.* Springer, Berlin Heidelberg, 2000.

[78] K. Izdinsky, P. Stefanik, and S. Kavecky. High Temperature Heat Sinks - Alternative concepts report phases 2. Technical report, IMSAS, 2005.

[79] PLANSEE. Wolfram - Werkstoffeigenschaften und Anwendungen. Technical report, 2000.

[80] Specialty Materials. Silicon Carbide Fiber Properties. http://www.specmaterials.com.

[81] P. W. M. Peters, J. Hemptenmacher, and H. Schurmann. Fibre and wire reinforced copper alloys as heat sinks for fusion reactors. *Materialwissenschaft und Werkstofftechnik*, 38:755–765, 2007.

[82] MatWeb. Online Material Data Sheet, 2008. http://www.matweb.com/.

[83] Deutsches Kupfer Institut. Datenblatt CuCr1Zr - Legierung, 2005. http://www.kupferinstitut.de.

[84] C. Popescu. *Processing and Characterisation of SiC Fibre reinforced Cu-Matrix Composites*. PhD thesis, TUM, 2004.

[85] A. Brendel. Specification of User Requirements on Heat Sink Materials for the Divertors of Fusion Devices. Technical report, IPP, March 2005 2005.

[86] A. Brendel, C. Popescu, T. Köck, and H. Bolt. Promising composite heat sink material for the divertor of future fusion reactors. *Journal of Nuclear Materials*, 367:1476–1480, 2007.

[87] A. Brendel, C. Popescu, C. Leyens, J. Woltersdorf, E. Pippel, and H. Bolt. SiC-fibre reinforced copper as heat sink material for fusion applications. *Journal of Nuclear Materials*, 329-33:804–808, 2004.

[88] S. Levchuk. *Interface development for a EUROFER steel matrix composite with SiC-fibre reinforcement*. PhD thesis, TUM, 2005.

[89] S. Levchuk, S. Lindig, A. Brendel, and H. Bolt. Interface reactions and control of diffusion at the interface between SiC fibres and layer of deposited Fe-9Cr base alloy. *Journal of Nuclear Materials*, 367:1233–1237, 2007.

[90] T. Köck. *Herstellung und Characterisierung eines SiC/Cu- Metall-Matrix-Verbundwerkstoffes mit angepasster Faser/Matrix-Grenzfläche*. PhD thesis, TUM, 2007.

[91] T. Köck, A. Brendel, and H. Bolt. Interface reactions between silicon carbide and interlayers in silicon carbide-copper metal-matrix composites. *Journal of Nuclear Materials*, 362(2-3):197–201, 2007.

[92] Extremat. European FP6 integrated project - Extremat - new materials for extreme environments, 2007. http://www.extremat.org/.

[93] Slovak academy of science. Institute for material and machine mechanics, 2008. http://www.umms.sav.sk.

[94] P. Majerus, R. Duwe, T. Hirai, W. Kuhnlein, J. Linke, and M. Rodig. The new electron beam test facility JUDITH II for high heat flux experiments on plasma facing components. *Fusion Engineering and Design*, 75-9:365–369, 2005.

[95] W. Espe. *Werkstoffkunde der Hochvakuumtechnik*, volume 1. VEB Deutscher Verlag der Wissenschaften, Berlin, 1959.

[96] A. D. Ivanov, A. K. Nikolaev, G. M. Kalinin, and M. E. Rodin. Effect of heat treatments on the properties of CuCrZr alloys. *Journal of Nuclear Materials*, 307:673–676, 2002.

[97] M. Merola, A. Orsini, E. Visca, S. Libera, L. F. Moreschi, S. Storai, B. Panella, E. Campagnoli, G. Ruscica, and C. Bosco. Influence of the manufacturing heat cycles on the CuCrZr properties. *Journal of Nuclear Materials*, 307:677–680, 2002.

[98] L.-P. Zhou, M.-P. Wang, R. Wang, Z. Li, J.-J. Zhu, K. Peng, D.-Y. Li, and S.-L. Li. Enhanced adhesion of Cu-W thin films by ion beam assisting bombardment implanting. *Transactions of Nonferrous Metals Society of China*, 18(2):372–377, 2008.

[99] G. Sundberg, P. Paul, C. M. Sung, and T. Vasilos. Fabrication of CuSiC metal matrix composites. *Journal of Materials Science*, 41(2):485–504, 2006.

[100] P. B. Abel, A. L. Korenyiboth, F. S. Honecy, and S. V. Pepper. Study of Copper on Graphite with Titanium or Chromium Bond Layer. *Journal of Materials Research*, 9(3):617–624, 1994.

[101] H. Ye, X. Y. Liu, and H. Hong. Fabrication of metal matrix composites by metal injection molding - A review. *Journal of Materials Processing Technology*, 200(1-3):12–24, 2008.

[102] C. Leyens, J. Hausmann, and J. Kumpfert. Continuous fiber reinforced titanium matrix composites: Fabrication, properties and applications. *Advanced Engineering Materials*, 5(6):399–410, 2003.

[103] J. M. Hausmann, C. Leyens, J. Hemptenmacher, and W. A. Kaysser. Optimisation of the fatigue resistance of metal matrix composites. *Advanced Engineering Materials*, 4(7):497–500, 2002.

[104] M. Verrilli, Y. Kim, and T. Gabb. High Temperature Fatigue Behavior of Tungsten Copper Composites. *NASA Technical Memorandum 192404*, 1989.

[105] R. E. Lee and S. J. Harris. Matrix strengthening in continuous fibre reinforced composites under monotonic and cyclic loading conditions. *Journal of Materials Science*, 9(3):359–368, 1974.

[106] J. Zhang and C. Laird. Fracture behavior of monofilament-reinforced multicrys-talline copper composites. *Acta Materialia*, 49(1):109–122, 2001.

[107] J. Zhang and C. Laird. Fatigue fracture of tungsten monofilament-reinforced monocrystalline copper matrix composites. *Materials Science and Engineering A*, 283(1-2):126–135, 2000.

[108] J. Zhang and C. Laird. Cyclic hardening of tungsten monofilament-reinforced monocrystalline copper matrix composites. *Acta Materialia*, 47(14):3811–3824, 1999.

[109] Z. L. Wang and J. L. Lee. Electron Microscopy Techniques for Imaging and Analysis of Nanoparticles. In R. Kohli and H. Texas, editors, *Developments in Surface Contamination and Cleaning*. William Andrew, Norwich, NY, 2008.

[110] S. Amelinckx, D. van Dyck, J. van Landuyt, and G. van Tendeloo, editors. *Hand-book of Microscopy*, volume 1+2 of *Applications in Materials Science, Solid-State Physics and Chemistry*. VCH, Weinheim, 1997.

[111] G. Binnig, C. F. Quate, and C. Gerber. Atomic Force Microscope. *Physical Review Letters*, 56(9):930–933, 1986.

[112] B. Bhushan. *Handbook of Micro/Nanotribology*. CRC Press, 1995.

[113] J. C. Vickerman, editor. *Surface Analysis -The Principal Techniques*. Jon Wiley and Sons, Manchester, 1997.

[114] T.W. Clyne and P.I. Withers. *An Introduction to Metal Matrix Composites*. Cambridge Solid State Science Series. Cambridge Univ.Press, Cambridge, 1995.

[115] M. Birkholz. *Thin Film Analysis by X-Ray Scattering*. WILEY-VCH Verlag GmbH and Co., Weinheim, 2006.

[116] B. Okolo, P. Lamparter, U. Welzel, T. Wagner, and E.J. Mittemeijer. The effect of deposition parameters and substrate surface condition on texture, morphology and stress in magnetron-sputter-deposited Cu thin films. *Thin Solid Films*, 474(1-2):50–63, 2005.

[117] J.R. Tesmer, C.J. Maggiore, M. Nastasi, and J.C. Barbour. A review of high en-ergy backscattering spectrometry. *Materials Chemistry and Physics*, 46(2-3):189–197, 1996.

[118] W.-K. Chu, J. Mayer, and M. Nicolet. *Backscattering Spectrometry*. Academic Press, 1978.

[119] H. Greuner, H. Bolt, B. Boswirth, T. Franke, P. McNeely, S. Obermayer, N. Rust, and R. Suss. Design, performance and construction of a 2 MW ion beam test facility for plasma facing components. *Fusion Engineering and Design*, 75-9:345–350, 2005.

[120] H. Greuner, B. Boeswirth, J. Boscary, A. Plankensteiner, and B. Schedler. High heat flux tests of the WENDELSTEIN 7-X pre-series target elements: Experimental evaluation of the thermo-mechanical behaviour. *Fusion Engineering and Design*, 82(15-24):1713–1719, 2007.

[121] W.K. Kim, H.G. Shin, B.H. Kim, and H.Y. Kim. Straightening of micro wires using the direct wire heating and pulling method. *International Journal of Machine Tools and Manufacture*, 47(7-8):1046–1052, 2007.

[122] P. D. Desai, T. K. Chu, H. M. James, and C. Y. Ho. Electrical - Resistivity of Selected Elements. *Journal of Physical and Chemical Reference Data*, 13(4):1069–1096, 1984.

[123] L.A. Hall. Survey of Electrical Resistivity Measurements on 16 Pure Metals in the Temperature Range 0 to 273 K. *NBS Technical Note*, 365, 1968.

[124] K.H. Hellwege. *Landolt-Börnstein Numerical Data and Functional Relationships in Science and Technology*, volume 15. Springer-Verlag, Heidelberg, 1982.

[125] C. Wang, J. Lei, C. Bjelkevig, S. Rudenja, N. Magtoto, and J. Kelber. Electrodeposition of adherent copper film on unmodified tungsten. *Thin Solid Films*, 445(1):72–79, 2003.

[126] J.-H. You and I. Komarova. Probabilistic failure analysis of a water-cooled tungsten divertor: Impact of embrittlement. *Journal of Nuclear Materials*, 375(3):283–289, 2008.

[127] Ansaldo-Ricerche, 2008. http://www.ansaldoricerche.it/.

[128] D. Necas, P. Klapetek, and et al. Gwyddion - A SPM data visualization and analysis tool, 2008. http://gwyddion.net/.

[129] E. S. Gadelmawla, M. M. Koura, T. M. A. Maksoud, I. M. Elewa, and H. H. Soliman. Roughness parameters. *Journal of Materials Processing Technology*, 123(1):133–145, 2002.

[130] T. Thomas. *Rough Surfaces*. Imperial College Press, London, 2nd edition, 1999.

[131] C. Douketis, Z. H. Wang, T. L. Haslett, and M. Moskovits. Fractal Character of Cold-Deposited Silver Films Determined by Low-Temperature Scanning-Tunneling-Microscopy. *Physical Review B*, 51(16):11022–11031, 1995.

[132] M. Mayer. SIMNRA user's guide. *Tech. Rep. IPP 9/113 Max-Planck-Institut für Plasmaphysik*, 1997.

[133] W. Beitz and K.-H. Grote. *Dubbel -Taschenbuch für den Maschinenbau*. Springer Verlag, 19th edition, 1997.

[134] D. K. Shetty. Shear-Lag Analysis of Fiber Push-out (Indentation) Tests for Estimating Interfacial Friction Stress in Ceramic-Matrix Composites. *Journal of the American Ceramic Society*, 71(2):C107–C109, 1988.

[135] G. Rausch, B. Meier, and G. Grathwohl. A Push-out Technique for the Evaluation of Interfacial Properties of Fiber-Reinforced Materials. *Journal of the European Ceramic Society*, 10(3):229–235, 1992.

[136] Helmholtz-Zentrum Berlin für Materialien und Energie, 2008. http://www.hmi.de/.

[137] T. Poeste, R. C. Wimpory, and R. Schneider. The new and upgraded neutron instruments for material science at HMI - current activities in cooperation with industry. *Residual Stresses VII*, 524-525:223–228, 2006.

[138] M.E. Fitzpatrick and A. Lodini, editors. *Analysis of Residual Stresses by Diffraction using Neutron and Synchrotron Radiation*. Taylor and Francis Inc, London, 2003.

[139] H. Greuner, A. Herrmann, H. Renner, P. Chappuis, and R. Mitteau. Development of Divertor Targets for WENDELSTEIN 7-X, 1998.

[140] M. Scheerer, H. Bolt, A. Gervash, J. Linke, and I. Smid. The design of actively cooled plasma-facing components. *Physica Scripta*, T91:98–103, 2001.

[141] J. Schlosser. Update of Thermal Hydraulic Data Base. Pco/95-12, CEA Cadarache.

[142] VDI. *VDI-Wärmeatlas*, volume 3. VDI, Düsseldorf, 1977.

[143] K. Stephan. *Wärmeübergang beim Kondensieren und beim Sieden.* Springer Verlag, Berlin, 1988.

[144] L. S. Tong and G. F. Hewitt. Overall Viewpoint of Flow Boiling CHF Mechanisms. *Mechanical Engineering*, 94(9):56, 1972.

[145] L. S. Tong. Phenomenological Study of Critical Heat-Flux. *Mechanical Engineering*, 97(12):105–105, 1975.

[146] K. Oura, V.G. Liftshits, A.A. Saranin, A.V. Zotov, and M. Katayama. *Surface Science - An Introduction.* Springer, Berlin Heidelberg, 2003.

[147] D.A. King and D.P. Woodruff, editors. *The chemical physics of solid surfaces*, volume 8 of *Growth and properties of ultrathin epitaxial layers.* Elsevier, 1997.

[148] P. W. Voorhees. The Theory of Ostwald Ripening. *Journal of Statistical Physics*, 38(1-2):231–252, 1985.

[149] P. Villain, P. Goudeau, J. Ligot, S. Benayoun, K. F. Badawi, and J. J. Hantzpergue. X-ray diffraction study of residual stresses and microstructure in tungsten thin films sputter deposited on polyimide. *Journal of Vacuum Science and Technology A*, 21(4):967–972, 2003.

[150] E. Le Bourhis, D. Faurie, B. Girault, P. Goudeau, P. O. Renault, P. Villain, and F. Badawi. Mechanical properties of thin films and nanometric multilayers using tensile testing and synchrotron X-ray diffraction. *Plasma Processes and Polymers*, 4(3):311–317, 2007.

[151] Y. Kuru, M. Wohlschlögel, U. Welzel, and E.J. Mittemeijer. Coefficients of thermal expansion of thin metal films investigated by non-ambient X-ray diffraction stress analysis. *Surface and Coatings Technology*, 202(11):2306–2309, 2008.

[152] J.N. Mundy, S.J. Rothman, N.Q. Lam, H.A. Hoff, and L.J. Nowicki. Self-diffusion in tungsten. *Physical Review B*, 18(12), 1978.

[153] J.-M. Berthelot. *Composite Materials - Mechanical Behavior and Structural Analysis.* Springer, New York, 1999.

Acknowledgements

Keine Schuld ist dringender, als die, Dank zu sagen.
Marcus Tullius Cicero

An dieser Stelle möchte ich mich bei allen Personen bedanken, die zum Gelingen dieser Arbeit beigetragen haben.

Mein besonderer Dank gilt meinem Doktorvater **Prof. Dr. Dr. Harald Bolt**, der mir die Möglichkeit gegeben hat diese Arbeit am IPP durchzuführen. Für sein offenes Ohr, seine Unterstützungen und seine geschätzte Meinung, möchte ich Ihm herzlichst danken.

Bei **Prof. Dr. E. Werner** möchte ich mich für die Bereitstellung als Zweitgutachter bedanken.

Prof. Dr. H. Baier danke ich für die freundliche Unterstützung meine Promotion an der Fakultät für Maschinenwesen durchführen zu können.

Der größte Dank gilt meinem Betreuer **Dr. Martin Balden** der 3 Jahre lang mir mit Rat und Tat zur Seite stand. Lieber Martin, ich danke dir für die zahlreichen Gespräche und kritischen Diskussionen, deine unermüdliche Unterstützung, für das Vertrauen in mich sowie für dein beeindruckendes Wissen. Ich hätte mir keinen besseren Betreuer wünschen können.

Aus tiefstem Herzen möchte ich besonders **Dr. Thomas Köck** danken für die wundervolle Unterstützung, für sein fachliches Wissen und für die wertvollen Tipps in den letzten 3 Jahren.

Besonderen Dank schulde ich **Dr. Klaus Schmid** der jederzeit ein offenes Ohr für mich hatte und der mich mit seinen innovativen und kompetenten Ratschlägen immer wieder inspirierte.

Meinem Zimmernachbarn **Peter Worbs** danke ich für seine hilfsbereite und aufmerksame Art, für unsere zahlreichen Gespräche und sportlichen Aktivitäten.

Ebenso danke ich **Josef Schäftner,** der Mann meines Vertrauens für dringende und wichtige technische Arbeiten, **Henri Greuner** und **Bernd Böswirth** für die profes-